MOST-CRITICAL TRANSIENT DISTURBANCES IN AN INCOMPRESSIBLE FLAT-PLATE BOUNDARY LAYER

A Dissertation

by

JASON ANDREW MONSCHKE

Submitted to the Office of Graduate and Professional Studies of
Texas A&M University
in partial fulfillment of the requirements for the degree of

DOCTOR OF PHILOSOPHY

Chair of Committee,	Edward White
Committee Members,	William Saric
	Helen Reed
	Prabir Daripa
Head of Department,	Rodney Bowersox

December 2015

Major Subject: Aerospace Engineering

ABSTRACT

Transient growth is a linear disturbance growth mechanism that plays a key role in roughness-induced boundary-layer transition. It occurs when superposed stable, non-orthogonal continuous spectrum modes experience algebraic disturbance growth followed by exponential decay. Algebraic disturbance growth can modify the basic state making it susceptible to secondary instabilities rapidly leading to transition. Optimal disturbance theory was developed to model the most-dangerous disturbances. However, evidence suggests roughness-induced transient growth is sub-optimal yet leads to transition earlier than optimal theory suggests. This research computes initial disturbances most unstable to secondary instabilities to further develop the applicability of transient growth theory to surface roughness.

The main approach is using nonlinear adjoint optimization with solutions of the parabolized Navier–Stokes and BiGlobal stability equations. Three objective functions were considered: disturbance kinetic energy growth, sinuous instability growth rate, and Tollmien–Schlichting (TS) wave growth rate. The first objective function was used as validation of the optimization method. Counter-rotating streamwise vortices located low in the boundary layer maximize the sinuous instability growth rate. Sinuous instabilities were observed at disturbance amplitudes as low as 2.5% spanwise root-mean-square. The near wake of the initial disturbance is potentially much less stable than the far field. TS wave stabilization was achieved for all parameters considered and becomes more effective at higher frequencies.

DEDICATION

To those hardworking electrons, without whose sacrifice of energy this work would have been impossible.

ACKNOWLEDGEMENTS

First and foremost, I would like to acknowledge NASA and the Air Force Office of Scientific Research (AFOSR) for funding this work through AFOSR Grant FA9550-09-1-0341.

This research would not have been possible without the help of many other people. First, thanks is given to Drs. Nicholas Denissen & Pedro Paredes for numerous helpful conversations. I would like to thank Drs. Matthew Kuester & Nicole Sharp for access to their experimental data. Thanks is given to all past and present students at the Klebanoff–Saric Wind Tunnel (KSWT). Specifically I would like to acknowledge Alex Berger, Dr. Nicholas Denissen, Dr. Robert Downs III, Dr. Robert Ehrmann, Justin Freels, Dr. Matthew Kuester, Doug Kutz, Jeffrey Leistico, Robert Long, Dr. Jason Schmucker, Dr. Nicole Sharp, Jamie Weber, and Ben Wilcox.

The members of the National Aerothermochemistry Laboratory (NAL), Flight Research Laboratory (FRL), and Low-Speed Wind Tunnel (LSWT) have been very helpful. Specifically I am grateful to Robbie Allen, Lisa Brown, Dr. Alex Craig, Dr. Brian Crawford, Dr. Tom Duncan, John Kochan, Heather Kostak, Rebecca Marianno, Ian Neel, and David West.

I would like to acknowledge my committee members (Drs. Prabir Daripa, Helen Reed, William Saric, and especially my advisor Edward White) for their guidance and support throughout this process. Finally I would like to thank my family and friends for their love and encouragement along the way. There are too many to name them all but I appreciate the help of my parents Harold & Debbie Monschke, my grandparents Dorothy & Jan Farris, brother and sister-in-law Jeff & Kayla Monschke, and niece Lily Monschke.

NOMENCLATURE

		Page
β_0	Spanwise wavenumber nondimensionalized by δ_0	84
$\max_{x,y}(u'_{\mathrm{rms}})$	Maximum spanwise u' root-mean-square value	8
AFOSR	Air Force Office of Scientific Research	iv
ALSE	Adjoint linear stability equation	14
BiGlobal	Stability of basic states with two inhomogeneous directions	7
CFD	Computational fluid dynamics	7
DNS	Direct numerical simulation	1
F	Nondimensional frequency	79
FRL	Flight Research Laboratory	iv
g	Optimization objective function	18
k	Roughness height	3
KSWT	Klebanoff–Saric Wind Tunnel	iv
LSE	Linear stability equation	10
LSWT	Low-Speed Wind Tunnel	iv
NAL	National Aerothermochemistry Laboratory	iv
PNS	Parabolized Navier–Stokes	26
Re_δ	Reynolds number based on reference boundary layer thickness	12
Re_{kk}	Roughness Reynolds number	3
$\mathrm{Re}_{kk,\mathrm{crit}}$	Critical roughness Reynolds number	3
Re_{x_0}	Reynolds number based on initial disturbance location	72
Re_{x_f}	Reynolds number based on final optimization location	72
TS	Tollmien–Schlichting	4

TABLE OF CONTENTS

Page

LIST OF FIGURES

FIGURE Page

1. INTRODUCTION AND LITERATURE REVIEW

The manner in which a fluid flows around solid surfaces has many important implications. For instance, the design of aircraft relies on understanding the relation between the shape of a wing and the lift and drag that it produces. Accurate lift and drag estimation allows less conservative sizing of engines and structures. This in turn leads to a reduction in aircraft weight and fuel consumption.

In 1775, Leonhard Euler first derived the equations that describe inviscid fluid flow. These inviscid equations admit potential-function solutions. Flow around arbitrarily shaped objects can be approximated by superposing several basic potential flow solutions, such as sources, sinks, doublets, and vortices, that enforce the *no-penetration* boundary condition at surfaces. After Euler, nearly a century passed until viscous terms were added to the governing equations by Sir George Stokes in 1845, resulting in the renowned *Navier–Stokes* equations:

$$\nabla \cdot \boldsymbol{v} = 0, \tag{1.1}$$

$$\frac{\partial \boldsymbol{v}}{\partial t} + (\boldsymbol{v} \cdot \nabla)\, \boldsymbol{v} = -\nabla p + \frac{1}{\mathrm{Re}} \nabla^2 \boldsymbol{v}, \tag{1.2}$$

which govern viscous incompressible fluid flow. $\boldsymbol{v}$ is the vector of fluid velocities, p is the pressure, t is time, and Re is the Reynolds number.

Although the governing equations are known, a complete understanding of fluid flow has remained elusive. Only a few exact solutions for simple geometries of the Navier–Stokes equations have been found. With the explosion in computing power over the last half-century, much progress in the numerical solution of Eqs. (1.1) & (1.2) has been made. However, direct numerical simulation (DNS) of flow over a

full-size aircraft at cruising conditions remains infeasible to this day.

d'Alembert noticed that Euler's inviscid theory predicts zero drag on a body submerged in fluid. For years these inviscid potential flow solutions were criticized by experimentalists who found the theory clearly at odds with numerous observations. This created a deep divide between theorists who studied *hydrodynamics* and experimentalists who worked in the field of *hydraulics*.

It was not until Prandtl's revolutionary 1904 discovery of the boundary layer that finally resolved this paradox. A boundary layer is a thin layer of decelerated fluid near a surface. The boundary layer is a result of the viscous interaction of the molecules of a fluid with the microscopically rough surface of all solids. On a macroscopic length scale this interaction is represented as the *no-slip* boundary condition. Boundary layers were the missing piece that finally resolved d'Alembert's paradox. Superposing inviscid outer flow solutions with the near-wall boundary layer yields more accurate results.

Boundary layers can be either laminar or turbulent. Laminar boundary layers have very small unsteady fluctuations and the skin friction is low. In contrast, turbulent boundary layers are highly unsteady with a much higher skin friction. Osborne Reynolds was the first to observe this distinction between laminar and turbulent flow and discovered that it is related to what we now call the *Reynolds number* in his famous pipe flow experiment [1]. Dye that is injected at the inlet begins to oscillate instead of flowing smoothly as the velocity increases. As the fluid velocity, and thus Reynolds number, increased further the oscillations grew until the dye exhibited fully turbulent flow.

The formulation of the Navier–Stokes equation, the discovery of boundary layers, and the observation that oscillations in the flow can grow leading to turbulence have formed the backbone of fluid dynamics understanding for the last 100 years. Now

that some of the fundamentals of fluid flow have been described, a more detailed summary of the literature pertaining to roughness-induced boundary layer transition will be described in the next section.

1.1 Background

Transition from laminar to turbulent flow over practical aerodynamic surfaces is associated with significant increases in skin friction and surface heating. Delaying transition would reduce drag and fuel consumption and increase range on commercial airliners. It would also reduce aerodynamic heating and increase usable payload on reentry vehicles. Despite its importance, a fundamental understanding of the physical mechanisms responsible is incomplete.

The instabilities in laminar boundary layers over smooth surfaces have been researched extensively [2, 3, 4], leading to improved understanding and transition prediction using methods such as e^N [5, 6]. However, bug strikes and manufacturing defects inevitably roughen these aerodynamic surfaces leading to transition in otherwise stable regions. In the case of scramjets, roughness is intentionally applied to promote turbulent mixing and combustion and to prevent unstarting [7].

At low speeds, the effects of roughness are accounted for using roughness Reynolds number correlations [8]. The roughness Reynolds number is defined as $\mathrm{Re}_{kk} = \frac{U(k)k}{\nu}$ where k is the roughness height, $U(k)$ is the undisturbed streamwise velocity at the roughness height, and ν is the kinematic viscosity. Transition is predicted when $\mathrm{Re}_{kk} > \mathrm{Re}_{kk,\mathrm{crit}}$. These correlations give an estimate for the roughness height that could cause transition but do not give insight into the mechanisms responsible. Similar correlation methods have been used in hypersonic flow, for which Reda [9] and Schneider [10] provide extensive reviews. The quality of these empirical correlations is dependent on the quality of the experiments that they are calibrated against and

the degree to which the correlations capture the underlying physics. There have been several low-speed experiments on the effects of roughness but relatively little has been done in hypersonic flow to understand the mechanism of transition. Additionally, a critical roughness amplitude in a noisy wind tunnel may not be critical in the quiet flow found in flight [7]. Quiet-flow wind tunnel experiments are crucial to obtain meaningful transition predictions using these correlations.

The emergence of transient-growth theory provides a means of understanding how 3D surface roughness can be accommodated by linear stability theory [11]. Transient growth can occur in linearly stable regions due to the superposition of non-orthogonal continuous and discrete modes. At small amplitudes, transient growth is characterized by algebraic disturbance growth followed by exponential decay. If these disturbances reach a large enough amplitude, they can distort the basic state leading to "secondary" instabilities, breakdown, and transition. (Secondary is used in quotes since there is no primary instability.)

Transient-growth theory began with Ellingsen & Palm [12] who first showed that a vertical velocity disturbance within a shear layer leads to linear disturbance growth in time. Landahl [13, 14] later labeled the process of streamwise vorticity redistributing mean flow momentum the "lift-up" effect. Unlike primary instabilities such as the Tollmien–Schlichting (TS) wave, transient growth has no instability to amplify components of the broadband forcing and is highly coupled to the receptivity process.

To eliminate the ambiguity of receptivity, optimal disturbances were computed with the hope that they would represent the "most-dangerous" transient growth in regards to transition. Optimal disturbances are the initial conditions that lead to the largest disturbance growth over a specified domain [15, 16, 17]. While optimal theory provides a straightforward means of computing disturbances, experiments by White

& co-workers [18, 19, 8] show that physically realized roughness-induced transient growth is not well represented by optimal models.

Optimal disturbances are characterized by steady counter-rotating streamwise vorticies located high in the boundary layer. These vorticies generate high- and low-speed streaks by redistributing base flow momentum. In contrast, roughness-induced transient growth generates steady counter-rotating streamwise vorticies at multiple spanwise wavelengths low in the boundary layer. This difference in height causes the experimentally measured disturbance energy to peak far upstream and at much smaller values than optimal predictions.

Denissen & White [20] used biorthogonal decomposition to show that roughness receptivity is a nonlinear process confined to the immediate vicinity of the roughness. Although the receptivity is nonlinear, the subsequent transient growth is linear. They also clearly showed the significant differences in receptivity between optimal theory, roughness-induced transient growth, and linearized receptivity by comparing the continuous spectra receptivity curves. Optimal disturbances excite very slowly decaying continuous modes whereas roughness excites modes that decay much faster.

Past theoretical and computational studies on transient growth have focused on optimal theory [21, 22, 23]. Recently however, Denissen & White [24] showed that roughness-induced disturbances can lead to "secondary" instabilities at significantly lower amplitudes than optimal disturbances. The implication is that optimal disturbances are not the class of disturbance most likely to cause transition. Thus, there is a critical need to better understand roughness-induced transient growth and under what conditions it can lead to turbulence.

Compared to optimal theory, roughness-induced transient growth is less stable to secondary instabilities because of strengthened spanwise and wall-normal velocity gradients. However as the gradients increase, viscous decay causes disturbances to

quickly vanish before secondary instabilities can set in. This implies that there is a "most-critical" disturbance that may have features similar to roughness-induced transient growth. Developing a theory for these most-critical disturbances and connecting this theory to surface roughness is a key objective of this thesis. In particular, "most-critical" disturbances will be computed that maximize secondary instabilities for a fixed primary disturbance amplitude.

1.2 Roughness-Induced Transition

Currently the best methods for predicting the roughness height causing transition is based on $\mathrm{Re}_{kk,\mathrm{crit}}$ correlations. Past experimental research on roughness-induced transition focused on two-dimensional and three-dimensional roughness. Two-dimensional roughness has a height that is invariant in the spanwise direction. As the height of two-dimensional roughness increases, the transition location gradually advances forward [8]. This behavior is likely related to the role of two-dimensional roughness in TS wave receptivity to freestream acoustic disturbances [25]. Three-dimensional roughness exhibits a very different transition behavior. As the three-dimensional roughness height increases transition remains unaffected until Re_{kk} is greater than some critical value [2, 26, 27, 28, 29, 30]. At this point, transition occurs in the near vicinity of the roughness element.

Early flow visualization work by Gregory & Walker [31] established that three-dimensional roughness produces a horse-shoe vortex wrapped around the element. The orientation of the vortex is such that it induces a downward velocity downstream in the centerline of the roughness.

Klebanoff et al. [32] observed that $\mathrm{Re}_{kk,\mathrm{crit}} = 450$ for isolated cylindrical roughness elements with a unity height-to-diameter ratio. They also found that $\mathrm{Re}_{kk,\mathrm{crit}} = 325$ for hemispherical elements whose height-to-diameter ratio is 0.5. Von Doenhoff &

Braslow [29] noticed that $\mathrm{Re}_{kk,\mathrm{crit}}$ scales with $(k/d)^{2/5}$, where k is the roughness height and d is the diameter. Therefore as the roughness diameter is increased, the critical roughness height causing transition decreases. Combining the results of Klebanoff et al. [32] and Von Doenhoff & Braslow [29] the current best prediction of critical roughness Reynolds number for incompressible flat-plate flows is:

$$R_{kk,crit} = 450 \left(\frac{k}{d} \right)^{\frac{2}{5}}. \tag{1.3}$$

Klebanoff et al. [32] also noticed that transition always occurs a finite distance downstream of the roughness element. This implies that transition occurs as the result of an instability that must grow to a large amplitude first.

Several researchers have studied these instabilities in the wakes of roughness elements [21, 33, 34, 24, 35]. They have noticed that there are two primary types of instabilities, varicose and sinuous, named for the appearance of undulations in the resulting streaks. Figure 1.1 shows a notional example of each. Recently, Kegerise et al. [36] and Choudhari et al. [37] have studied supersonic boundary-layer instabilities induced by roughness elements with various planform shapes through experiment, computational fluid dynamics (CFD) computations, and stability analysis. These studies reveal the BiGlobal instability mechanisms that can lead to transition but they do not aid in understanding the transient growth process that generated the basic state.

While the $\mathrm{Re}_{kk,\mathrm{crit}}$ correlations are effective for incompressible flows, their usage for compressible flows is much more uncertain[9, 10]. If transient growth theory could be extended to explain why these correlations work at low speeds, it could then be used for better transition prediction at high speeds.

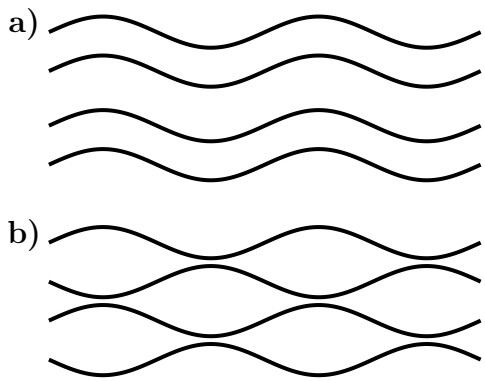

Figure 1.1: Notional example of **a)** sinuous and **b)** varicose modes. Flow is from left to right and lines represent streamlines in the streamwise-spanwise plane.

1.3 Research Objectives

The research challenge from Denissen [38] is:

> "There is a great deal of work still needed to develop transient growth 'theory.' […] Formulating the optimization problem to find the maximum integrated growth rate of the resulting secondary disturbances would provide a way to make transient growth more physically meaningful as a design tool."

The work presented in this dissertation develops a framework for exactly this calculation. To make optimal disturbances more relevant to surface roughness, using objective functions other than the disturbance kinetic energy is required. Objective functions that provide a measure of secondary instability growth rate are particularly interesting. Optimizing over spatial growth rates will allow the following questions to be answered:

- What is the most destabilizing disturbance that has a maximum spanwise steady disturbance amplitude, $\max_{x,y}(u'_{\text{rms}})$?

- What is the most stabilizing disturbance that has a maximum spanwise steady disturbance amplitude, $\max_{x,y}(u'_{\text{rms}})$?

The answer to the first question will be the "most-dangerous" transient disturbance. The answer to the second will shed light on potential transition control possibilities.

This research makes several important contributions to the literature. First, the "most-critical" disturbances will be an additional benchmark for comparison of future transient growth studies. Past work on optimal disturbances has focused on disturbance kinetic energy. This is not a useful metric. Optimal disturbances will become a more relevant design tool if they are linked to instabilities through basic state distortion. Second, the most destabilizing initial disturbance is likely more similar to roughness-induced transient growth than previous optimal models. And, finally, this optimal formulation facilitates finding a control disturbance that could delay transition. A potential control disturbance will reduce the TS wave N-factor but may breakdown at lower amplitudes from increased three-dimensionality. If a potential control disturbance is found it will require further verification through DNS and experiment.

2. TRANSIENT GROWTH

Although much progress has been made in the last century in understanding the processes by which a laminar boundary layer becomes turbulent, we still cannot reliably predict the transition location in even the simplest case — a flat plate. Morkovin's [39] transition roadmap, shown in Fig. 2.1, summarizes these transition processes as they are currently understood. First, environmental disturbances generate small fluctuations in laminar boundary layers. These small fluctuations can grow exponentially in the case of primary growth mechanisms. Once a sufficient disturbance amplitude is reached the laminar boundary layer with finite fluctuations is unstable to secondary instabilities. This scenario is labeled path A in Fig. 2.1 and is the path associated with transition due to Tollmien–Schlichting (TS) waves and other primary modal instabilities such as the crossflow instability.

However, even for flows in which there are no exponentially growing instabilities, transition has been observed [11]. Two common examples of this 'sub-critical' transition are elevated freestream turbulence [40] and surface roughness [8]. Transient growth plays a role in both transition scenarios [17, 11] but a full understanding of the process remains elusive due to uncertainty in receptivity.

The growth of transient disturbances, unlike primary instabilities such as the TS wave, is completely dependent on the receptivity process. Receptivity is the process by which environmental disturbances enter the boundary layer. Optimal disturbances answered the receptivity question by finding the initial disturbances that lead to the largest disturbance kinetic energy growth downstream. One way to quantify receptivity is to decompose a disturbance into the continuous spectrum modes of the linear stability equation (LSE).

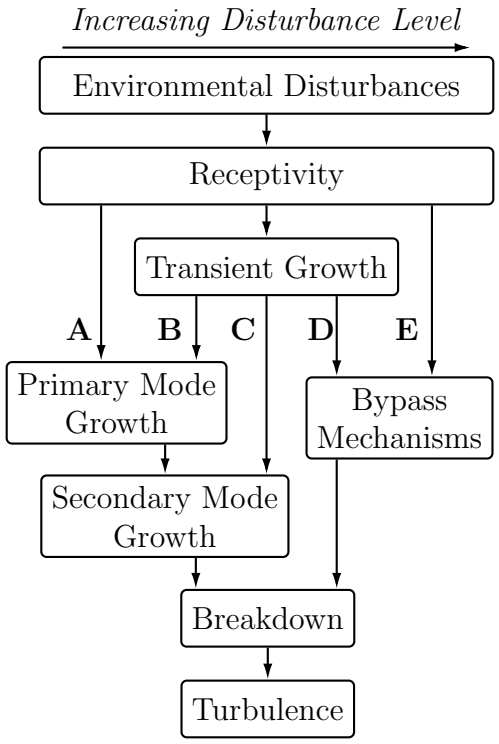

Figure 2.1: The path from laminar to turbulent flow summarized in the transition roadmap by Morkovin [39].

2.1 Continuous Spectrum

Following Denissen & White [20], the LSEs can be written as:

$$\frac{\partial \boldsymbol{\phi}}{\partial y} = \boldsymbol{A}\boldsymbol{\phi}, \tag{2.1}$$

where $\boldsymbol{\phi} = [\hat{u},\ D\hat{u},\ \hat{v},\ \hat{p},\ \hat{w},\ D\hat{w}]^T$. The boundary conditions for the LSEs are zero velocity fluctuations ($\hat{u} = \hat{v} = \hat{w} = 0$) at the wall and the freestream for a total of six boundary conditions. To admit continuous spectra solutions of the equations, instead of $\hat{u} = 0$, $\hat{v} = 0$, and $\hat{w} = 0$, the freestream boundary conditions are relaxed and only boundedness is required: $|\hat{u}| < \infty$, $|\hat{v}| < \infty$, and $|\hat{w}| < \infty$ as $y \to \infty$. Any particular disturbance includes a superposition of all the continuous spectrum modes and their sum must go to zero as $y \to \infty$.

In the freestream, the operator $\boldsymbol{A}$ reduces to a matrix of constant coefficients and solutions take the form $\boldsymbol{\phi} \propto e^{\lambda y}$. Since the LSEs are sixth order, there are six asymptotic freestream eigenvalues:

$$\begin{aligned}
\lambda_{1,2} &= \pm\sqrt{\alpha^2 + \beta^2)} \\
\lambda_{3,5} &= -\sqrt{i\left(\alpha - \mathrm{Re}_\delta F\right)\mathrm{Re}_\delta + \alpha^2 + \beta^2} \\
\lambda_{4,6} &= +\sqrt{i\left(\alpha - \mathrm{Re}_\delta F\right)\mathrm{Re}_\delta + \alpha^2 + \beta^2},
\end{aligned} \tag{2.2}$$

where α is the streamwise wavenumber, β is the spanwise wavenumber, Re_δ is the Reynolds number based on δ, and F is the nondimensional frequency.

There are two classes of solutions to the linear stability equations: discrete and continuous spectrum modes. Discrete modes, such as TS waves, asymptotically approach zero as $y \to \infty$ and are a linear combination of the eigenvectors associated with λ_2, λ_3, and λ_5, the eigenvalues with negative real part. There are a finite number

of discrete spatial eigenvalues, α, such that the boundary conditions at $y = 0$ are satisfied [41].

Continuous spectrum modes only require boundedness as $y \to \infty$. This requires $\mathrm{Re}(\lambda) \leq 0$ in the freestream. Solving for the spatial eigenvalues, α, such that $\lambda = ik$ where $k \in \mathbb{R}$ and $k > 0$, defines the continuous spectrum. Since freestream continuous spectrum solutions have the form e^{iky}, k can be interpreted as a wall-normal wavenumber. There are two types of continuous spectrum modes that occur on separate branches in the complex α plane, pressure and vorticity modes, named for their primary disturbance component. Pressure modes are obtained by setting $\lambda_{1-2} = ik$ whereas vorticity modes result from setting $\lambda_{3-6} = ik$. Since the spatial decay rates of pressure modes are orders of magnitude higher than vorticity modes they are typically ignored [20]. Setting $\lambda_{3-6} = ik$ to obtain the vorticity modes yields four solutions, that occur as two complex-conjugate pairs that represent upstream and downstream vorticity branches. The downstream vorticity branches are arbitrarily named the A and B branches [42].

For a given nondimensional frequency, Reynolds number, and basic state, the LSEs are solved by integrating from the freestream to the wall using a Gram–Schmidt orthonormalization procedure [43].

If the amplitudes of discrete modes and amplitude curves of continuous spectrum modes are known, the complete disturbance profile can be reconstructed:

$$\boldsymbol{\phi}(y) = \sum_{d} C_d \boldsymbol{\phi}_{\alpha_d}(y) + \sum_{j} \int_0^\infty C_j(k) \boldsymbol{\phi}_{\alpha_j}(y) dk \tag{2.3}$$

where indices d and j are for the discrete modes and branches of the continuous spectrum, respectively. Outside the boundary layer continuous spectrum modes have asymptotic solutions which oscillate in y, $\boldsymbol{\phi}_{\alpha_j} \propto f_m(k) e^{iky}$. Experiments show that

boundary layer disturbances decay far from the wall, $\boldsymbol{\phi}(y) \to 0$ as $y \to \infty$. Therefore from Eq. (2.3), integrals of this type must vanish:

$$\lim_{y\to\infty} \int_0^\infty C_j(k) f_m(k) e^{iky} dk = 0,$$

where $f_m(k)$ is from the linear combination of eigenvectors associated with λ_m. This is the Riemann–Lebesgue lemma and is satisfied as long as $C_j(k)f_m(k)$ is L_1 integrable.

In order to find the amplitudes of discrete and continuous spectrum modes, a set of functions that are orthogonal to $\boldsymbol{\phi}$ must be found. This requires finding an adjoint equation. The adjoint linear stability equations (ALSEs) and boundary conditions are found by multiplying Eq. (2.1) by $\boldsymbol{\psi}^T$ and integrating by parts:

$$\begin{aligned} & \frac{\partial \boldsymbol{\psi}}{\partial y} = -\boldsymbol{A}^T \boldsymbol{\psi} \\ y = 0: \quad & \psi_2 = \psi_4 = \psi_6 = 0 \\ y \to \infty: \quad & |\psi_2|,\ |\psi_4|,\ |\psi_6| < \infty. \end{aligned} \tag{2.4}$$

For the derivation of a biorthogonality condition, the matrix operator in Eqs. (2.1) & (2.4) needs to be factored into quantities independent of α. First, the state vector is augmented to remove non-linearities in α:

$$\tilde{\boldsymbol{\phi}} = \left[\hat{u},\ \frac{\partial \hat{u}}{\partial y},\ \hat{v},\ \hat{p}\hat{u},\ D\hat{u},\ \hat{v},\ \hat{p},\ \hat{w},\ D\hat{w},\ i\alpha\hat{u},\ i\alpha\hat{v},\ i\alpha\hat{w}\right]^T.$$

Then the augmented direct and adjoint equations are:

$$\frac{\partial \tilde{\boldsymbol{\phi}}}{\partial y} = \tilde{\boldsymbol{A}} \tilde{\boldsymbol{\phi}} \tag{2.5}$$

$$\frac{\partial \tilde{\boldsymbol{\psi}}}{\partial y} = -\tilde{\boldsymbol{A}}^T \tilde{\boldsymbol{\psi}} \tag{2.6}$$

where the boundary conditions are unchanged and the associated augmented matrix operators are given in Appendix C. This allows the augmented operator to be factored:

$$\tilde{\boldsymbol{A}} = \tilde{\boldsymbol{A}}_1 + i\alpha \tilde{\boldsymbol{A}}_2.$$

By taking the integral of $\tilde{\boldsymbol{\psi}}_{\alpha'}$, the augmented adjoint solution with spatial eigenvalue α', multiplied by Eq. (2.5), a biorthogonality condition is derived [42]. Using the factorization above, the integral becomes: ($D \equiv \partial/\partial y$)

$$\int_0^\infty \tilde{\boldsymbol{\psi}}_{\alpha'}^T D\tilde{\boldsymbol{\phi}}_\alpha dy = \int_0^\infty \tilde{\boldsymbol{\psi}}_{\alpha'}^T \left(\tilde{\boldsymbol{A}}_1 + i\alpha \tilde{\boldsymbol{A}}_2\right) \tilde{\boldsymbol{\phi}}_\alpha dy.$$

Integrating by parts, using the adjoint equation, Eq. (2.6), and using the direct and adjoint boundary conditions, the above equation becomes a biorthogonality inner product:

$$\left\langle \tilde{\boldsymbol{\phi}}_\alpha, \tilde{\boldsymbol{\psi}}_{\alpha'} \right\rangle \Big|_0^\infty = \int_0^\infty \tilde{\boldsymbol{\psi}}_{\alpha'}^T \tilde{\boldsymbol{A}}_2 \tilde{\boldsymbol{\phi}}_\alpha dy = Q_\alpha \delta(\alpha - \alpha'). \tag{2.7}$$

In Eq. (2.7), δ is a Dirac delta if $\tilde{\boldsymbol{\phi}}_\alpha$ and $\tilde{\boldsymbol{\psi}}_{\alpha'}$ are continuous spectrum modes and δ is a Kronecker delta if either is a discrete mode.

In the case of discrete modes, the normalization constant, Q_α, is found by numerically calculating the biorthogonal inner product since the integrand decays as $y \to \infty$. In the case of continuous spectrum modes, more care is needed. Following Tumin [42], the biorthogonal inner product over a narrow wave packet is expanded

into integrals in the boundary layer and freestream:

$$\begin{aligned}\lim_{\epsilon\to 0}\int_{k-\epsilon}^{k+\epsilon}\left\langle\tilde{\boldsymbol{\phi}}_\alpha,\tilde{\boldsymbol{\psi}}_{\alpha'}\right\rangle\Big|_0^\infty dk =& \lim_{\epsilon\to 0}\int_{k-\epsilon}^{k+\epsilon}\left\langle\tilde{\boldsymbol{\phi}}_\alpha,\tilde{\boldsymbol{\psi}}_{\alpha'}\right\rangle\Big|_0^L dk \\ &- \lim_{\epsilon\to 0}\int_{k-\epsilon}^{k+\epsilon}\left\langle\tilde{\boldsymbol{\phi}}_\alpha^\infty,\tilde{\boldsymbol{\psi}}_{\alpha'}^\infty\right\rangle\Big|_0^L dk \\ &+ \lim_{\epsilon\to 0}\int_{k-\epsilon}^{k+\epsilon}\left\langle\tilde{\boldsymbol{\phi}}_\alpha^\infty,\tilde{\boldsymbol{\psi}}_{\alpha'}^\infty\right\rangle\Big|_0^\infty dk\end{aligned} \tag{2.8}$$

where $\tilde{\boldsymbol{\phi}}_\alpha$ and $\tilde{\boldsymbol{\psi}}_{\alpha'}$ are continuous spectrum solutions of the direct and adjoint equations for eigenvalues $\alpha(k)$ and $\alpha'(k')$, respectively. The superscript ∞ indicates asymptotic solutions in the freestream and L is the edge of the boundary layer. The first two integrals on the right side vanish as $\epsilon \to 0$ because the integrands are finite. The asymptotic solutions can be written in terms of the freestream eigenvectors of Eq. (2.5):

$$\begin{aligned}\tilde{\boldsymbol{\phi}}_{\alpha,A}^\infty(y) &= \zeta_3\tilde{\boldsymbol{\phi}}_3^\infty e^{\lambda_3 y} + \zeta_5\tilde{\boldsymbol{\phi}}_5^\infty e^{\lambda_5 y} + \zeta_6\tilde{\boldsymbol{\phi}}_6^\infty e^{\lambda_6 y} \\ \tilde{\boldsymbol{\phi}}_{\alpha,B}^\infty(y) &= \zeta_3\tilde{\boldsymbol{\phi}}_3^\infty e^{\lambda_3 y} + \zeta_4\tilde{\boldsymbol{\phi}}_4^\infty e^{\lambda_4 y} + \zeta_6\tilde{\boldsymbol{\phi}}_6^\infty e^{\lambda_6 y} \\ \tilde{\boldsymbol{\psi}}_{\alpha',A}^\infty(y) &= \xi_3\tilde{\boldsymbol{\psi}}_3^\infty e^{\lambda_3' y} + \xi_5\tilde{\boldsymbol{\psi}}_5^\infty e^{\lambda_5' y} + \xi_4\tilde{\boldsymbol{\psi}}_4^\infty e^{\lambda_4' y} \\ \tilde{\boldsymbol{\psi}}_{\alpha',B}^\infty(y) &= \xi_3\tilde{\boldsymbol{\psi}}_3^\infty e^{\lambda_3' y} + \xi_4\tilde{\boldsymbol{\psi}}_4^\infty e^{\lambda_4' y} + \xi_4\tilde{\boldsymbol{\psi}}_4^\infty e^{\lambda_4' y}\end{aligned} \tag{2.9}$$

where ζ_j and ξ_j are the coefficients of the freestream eigenvectors ($\tilde{\boldsymbol{\phi}}_j^\infty$ and $\tilde{\boldsymbol{\psi}}_j^\infty$) so that the boundary conditions are satisfied. The last term on the right of Eq. (2.8) does not vanish and consists of integrals of the type [42]:

$$\lim_{\epsilon\to 0}\int_{k-\epsilon}^{k+\epsilon}\int_0^\infty e^{i(k-k')y}dydk = \pi\delta(k-k') \tag{2.10}$$

where δ is the Dirac delta. Q_α for continuous spectrum modes is then known explicitly:

$$Q_\alpha = \pi \boldsymbol{A}_2^{(ij)} \left(\zeta_3 \tilde{\boldsymbol{\phi}}_{j,3}^{\infty} \xi_6 \tilde{\boldsymbol{\psi}}_{i,6}^{\infty} + \zeta_5 \tilde{\boldsymbol{\phi}}_{j,5}^{\infty} \xi_6 \tilde{\boldsymbol{\psi}}_{i,6}^{\infty} + \zeta_6 \tilde{\boldsymbol{\phi}}_{j,6}^{\infty} \xi_3 \tilde{\boldsymbol{\psi}}_{i,3}^{\infty} + \zeta_6 \tilde{\boldsymbol{\phi}}_{j,6}^{\infty} \xi_5 \tilde{\boldsymbol{\psi}}_{i,5}^{\infty} \right) \tag{2.11}$$

where subscript i and j denote the component of the freestream eigenvectors, and summation is implied. There is a unique normalization constant for both the A and B modes which is obtained by using the A and B values of ζ_i, $\tilde{\boldsymbol{\phi}}_{j,i}^{\infty}$, ξ_j, and $\tilde{\boldsymbol{\psi}}_{i,j}^{\infty}$ in the equation above.

2.2 Receptivity

Provided that the boundary-layer disturbance created by an environmental disturbance is linear, its receptivity is quantified by the set of mode amplitude coefficients and functions, C_d and $C_j(k)$, that constitute the resulting boundary layer disturbance.

Tumin & Reshotko [44] examined approximating the effects of surface roughness using slip boundary conditions. The slip velocity at the surface, $y = 0$, was determined such that no-slip is enforced at the local roughness height, $y = hf(x, z)$, where h is the height of the roughness and $f(x, z)$ describes the shape. Assuming the receptivity is linear, the slip velocity boundary condition at $y = 0$ is:

$$u = -hf(x, z) \frac{\partial U}{\partial y}.$$

This requires $h/L \ll R_L^{-5/8}$ [45]. By taking the Fourier transform of the boundary condition, using Eq. (2.7), and the Residue theorem [38], the continuous spectrum receptivity coefficients can be found for the A and B vorticity branches:

$$C_A(k) = -\frac{2\pi}{Q_\alpha^A} \hat{u}_k \hat{\psi}_{k,1}^{(A)}|_0 \tag{2.12}$$

$$C_B(k) = -\frac{2\pi}{Q_\alpha^B}\hat{u}_k\hat{\psi}_{k,1}^{(B)}|_0, \tag{2.13}$$

where $\hat{u}_k$ is the Fourier transformed boundary condition:

$$\hat{u}_k = -\frac{h}{2\pi}\frac{\partial U}{\partial y}\int_{-\infty}^{\infty}\int_{-\infty}^{\infty} f(x,z)e^{i(\alpha(k)x+\beta z)}dxdz. \tag{2.14}$$

While the possibility of obtaining the receptivity coefficients, and therefore the full velocity field, directly from the roughness shape is appealing, for the cylindrical roughness case no transient growth is observed [44]. This is clearly at odds with several experiments that will be described in the next few sections. Tumin & Reshotko [44] attribute this discrepancy to violation of the very restrictive triple-deck assumptions on the roughness height.

Optimal theory was developed to eliminate the receptivity problem by finding the initial upstream disturbance which maximizes the relative disturbance kinetic energy growth downstream. Previous researchers [15, 17, 16] formulated the optimization problem as:

$$\begin{aligned} \text{maximize} \quad & g(\beta,\, \omega,\, \mathrm{Re}_\delta,\, x_{opt}) = \mathcal{E}(\boldsymbol{q}'|_{x_{opt}}) \\ \text{subject to} \quad & f(\beta,\, \omega,\, \mathrm{Re}_\delta) = \mathcal{E}(\boldsymbol{q}'|_0) - 1 = 0 \end{aligned}$$

where $\boldsymbol{q}' = [u', v', w']^T$, $\mathcal{E}$ is the disturbance kinetic energy operator defined as:

$$\mathcal{E}(\boldsymbol{q}') = \int_z\int_y \left(|u'|^2 + |v'|^2 + |w'|^2\right) dydz,$$

and $g(\beta,\, \omega,\, \mathrm{Re}_\delta,\, x_{opt})$ is the relative growth from $x = 0$ to $x = x_{opt}$. With the exception of Zuccher et al. [46], only linear optimal disturbances have been considered in the literature. Multiple researchers have performed nonlinear calculations but those are initiated by the optimal disturbance computed using linear theory. For

linear disturbances, the value in the constraint function is arbitrary. There have been three main techniques used to solve this linear optimization problem. A description of each is provided as a foundation for the main results of this dissertation.

First, Butler & Farrell [15] used variational calculus to solve the optimization problem. Using a Lagrange multiplier and writing the energy operator in matrix form, the optimization can be reduced to a single functional in terms of receptivity coefficients for the discretized spectra:

$$\mathcal{J} = \boldsymbol{C}_\alpha^H \boldsymbol{R}^H \boldsymbol{E} \boldsymbol{R} \boldsymbol{C}_\alpha - \lambda \left(\boldsymbol{C}_\alpha^H \boldsymbol{E} \boldsymbol{C}_\alpha - 1 \right)$$

where $\boldsymbol{R} = \text{diag}\{\exp(i\alpha x)\}$. The stationary points are determined by differentiating the functional:

$$\frac{\partial \mathcal{J}}{\partial \boldsymbol{C}_\alpha} = \boldsymbol{R}^H \boldsymbol{E} \boldsymbol{R} \boldsymbol{C}_\alpha - \lambda \boldsymbol{E} \boldsymbol{C}_\alpha = \boldsymbol{0}$$

$$\frac{\partial \mathcal{J}}{\partial \lambda} = \boldsymbol{C}_\alpha^H \boldsymbol{E} \boldsymbol{C}_\alpha - 1 = 0.$$

This results in a generalized eigenvalue problem where $\sup\{\lambda_i\}$ is the optimal growth factor.

Schmid & Henningson [47] used a somewhat different method to obtain the optimal solution. Since the energy matrix $\boldsymbol{E}$ is symmetric and positive definite, an alternative formulation is to use singular value decomposition. First $\boldsymbol{E} = \boldsymbol{F}^H \boldsymbol{F}$ is factored using Cholesky decomposition. The optimization problem is then rewritten as:

$$\max_{\|\boldsymbol{F}\boldsymbol{C}_\alpha\|_2 = 1} \|\boldsymbol{F} \boldsymbol{R} \boldsymbol{C}_\alpha\|_2.$$

Since the induced norm of a matrix $\boldsymbol{A}$ is equal to the largest singular value of $\boldsymbol{A}$ for

the case of the Euclidean norm:

$$\|\boldsymbol{A}\|_2 = \max_{\|\boldsymbol{x}\|_2=1} \|\boldsymbol{A}\boldsymbol{x}\|_2 = \Sigma_{\max}(\boldsymbol{A})$$

where $\Sigma_{\max}(\boldsymbol{A})$ is the largest singular value of $\boldsymbol{A}$. Then using the manipulation $\boldsymbol{F}\boldsymbol{C}_\alpha = \boldsymbol{x}$, the maximization problem can be written as

$$\max_{\|\boldsymbol{F}\boldsymbol{C}_\alpha\|_2=1} \|\boldsymbol{F}\boldsymbol{R}\boldsymbol{C}_\alpha\|_2 = \|\boldsymbol{F}\boldsymbol{R}\boldsymbol{F}^{-1}\|_2.$$

This last expression can be factored using singular value decomposition as:

$$\boldsymbol{F}\boldsymbol{R}\boldsymbol{F}^{-1} = \boldsymbol{U}\boldsymbol{\Sigma}\boldsymbol{V}^H$$

where $\boldsymbol{U}$ and $\boldsymbol{V}$ are unitary matrices and $\boldsymbol{\Sigma}$ is diagonal. The optimal growth rate is given by the largest singular value Σ_i and the receptivity coefficients are given by $\boldsymbol{C}_\alpha = \boldsymbol{F}^{-1}\boldsymbol{V}_i$.

Luchini [16] and Andersson et al. [17] used an optimization method based on the use of adjoint equations. If $\mathcal{A}$ is the operator that solves the initial value problem of propagating a disturbance downstream, $\mathcal{A}^+$ is the adjoint of this operator. The optimization problem can then be written using operator theory as:

$$g = \frac{\boldsymbol{q}'^{+}\mathcal{A}^{+}\boldsymbol{Q}_{\text{out}}\mathcal{A}\boldsymbol{q}'}{\boldsymbol{q}'^{+}\boldsymbol{Q}_{\text{in}}\boldsymbol{q}'}$$

where $\boldsymbol{Q}_{\text{out}}$ and $\boldsymbol{Q}_{\text{in}}$ are matrix representations of the energy norm at the output and input locations respectively. Careful observation reveals that this is a generalized eigenvalue problem:

$$\mathcal{A}^{+}\boldsymbol{Q}_{\text{out}}\mathcal{A}\boldsymbol{q}' = g\boldsymbol{Q}_{\text{in}}\boldsymbol{q}'.$$

Since only the largest value of g is needed, rapid convergence is achieved using power iterations:

$$\boldsymbol{q}'_{n+1} = \boldsymbol{Q}_{\text{in}}^{-1}\mathcal{A}^{+}\boldsymbol{Q}_{\text{out}}\mathcal{A}\boldsymbol{q}'_{n}.$$

This method is similar to the variational calculus method. However, by marching forwards and backwards of the direct and adjoint equations, the non-parallel assumption is not required.

The general finding is that counter-rotating streamwise vortices located high in the boundary layer generate the most disturbance kinetic energy growth. Andersson et al. [17] and Tumin & Reshotko [48] found that a spanwise wavenumber of $\beta = 0.45$ is optimal. Using the biorthogonal decomposition method explained above, a typical optimal disturbance is decomposed into its constituent continuous spectrum modes in Fig. 2.2.

White [18] first showed that transient growth produced by a periodic array of roughness elements is not well described by optimal theory. Fransson et al. [49] performed a similar experiment and showed that if optimal disturbances are rescaled so that the streamwise vortices occur lower in the boundary layer, the agreement with experimental measurements is much better. Later experiments by White & coworkers [19, 8] obtained higher quality measurements of roughness-induced transient growth.

Denissen & White [20] developed a method to decompose experimental measurements of the streamwise velocity within a transiently growing boundary layer into its constituent continuous spectrum modes. This provides a unique and complete characterization of the receptivity to surface roughness.

Rizzetta & Visbal [50] performed a DNS corresponding to the Ergin & White [8] experiment. The advantage of DNS is that all velocity information is known. This

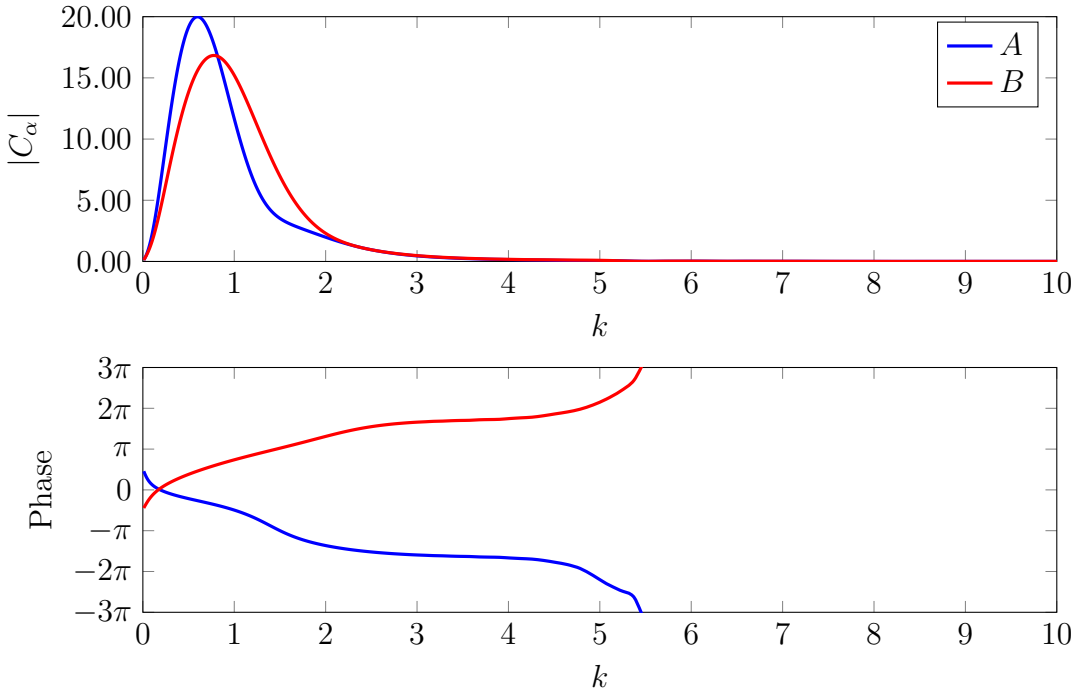

Figure 2.2: Continuous spectrum receptivity curves for an optimal disturbance computed using the methods of Tumin & Reshotko [48].

allows the complete data biorthogonal decomposition method of Tumin [42] to be used. Figures 2.3-2.6 show the receptivity curves for the first four spanwise wavelengths. The peak of $|C_\alpha|$ for all receptivity curves for the DNS data occurs at $k > 1.2$ whereas the maximum in Fig. 2.2 is at $k \approx 0.7$.

2.3 Summary & Research Objective

Understanding of transition has progressed steadily over the past century through studying the instabilities of laminar boundary layers. Paradoxically though, transition has been observed in flows which are linearly stable. One possible explanation of this sub-critical transition is transient growth. Transient growth has been observed in multiple experiments as the result of a laminar boundary layer encountering surface roughness. The main difficulty in studying transient growth is its intimate dependence

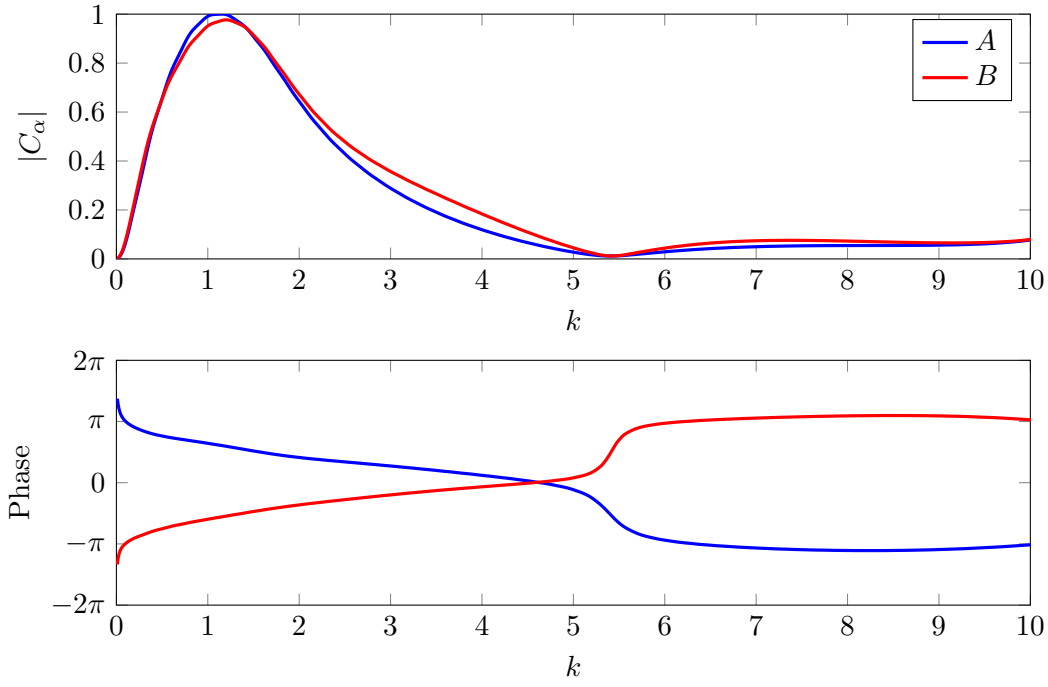

Figure 2.3: Continuous spectrum receptivity curves for λ_k spanwise wavelength of the DNS results of Rizzetta & Visbal [50].

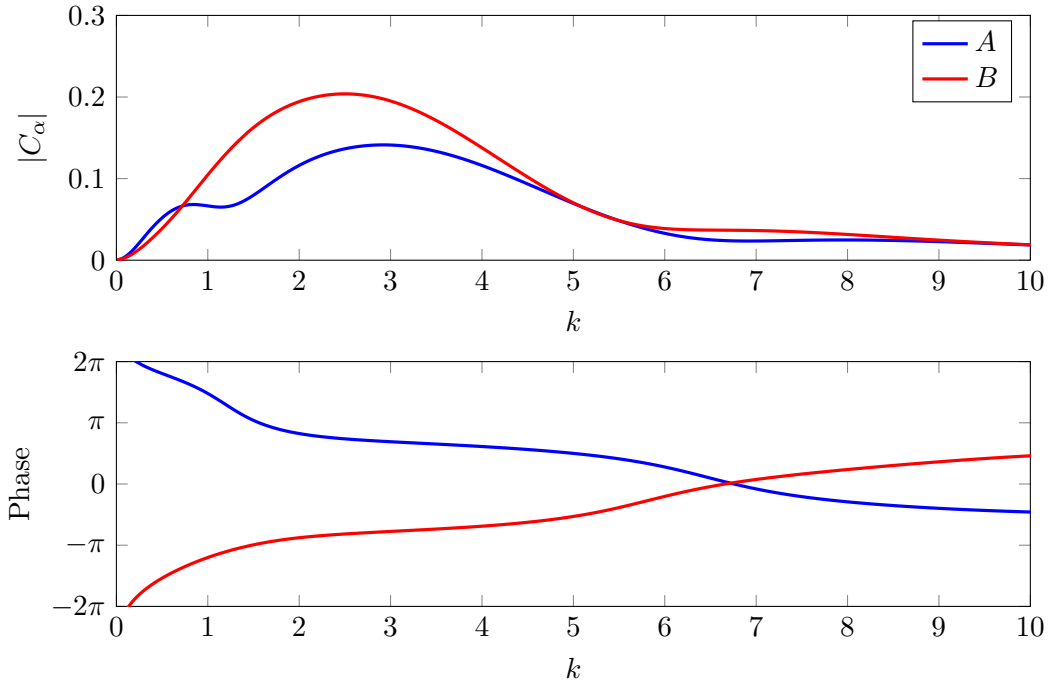

Figure 2.4: Continuous spectrum receptivity curves for $\lambda_k/2$ spanwise wavelength of the DNS results of Rizzetta & Visbal [50].

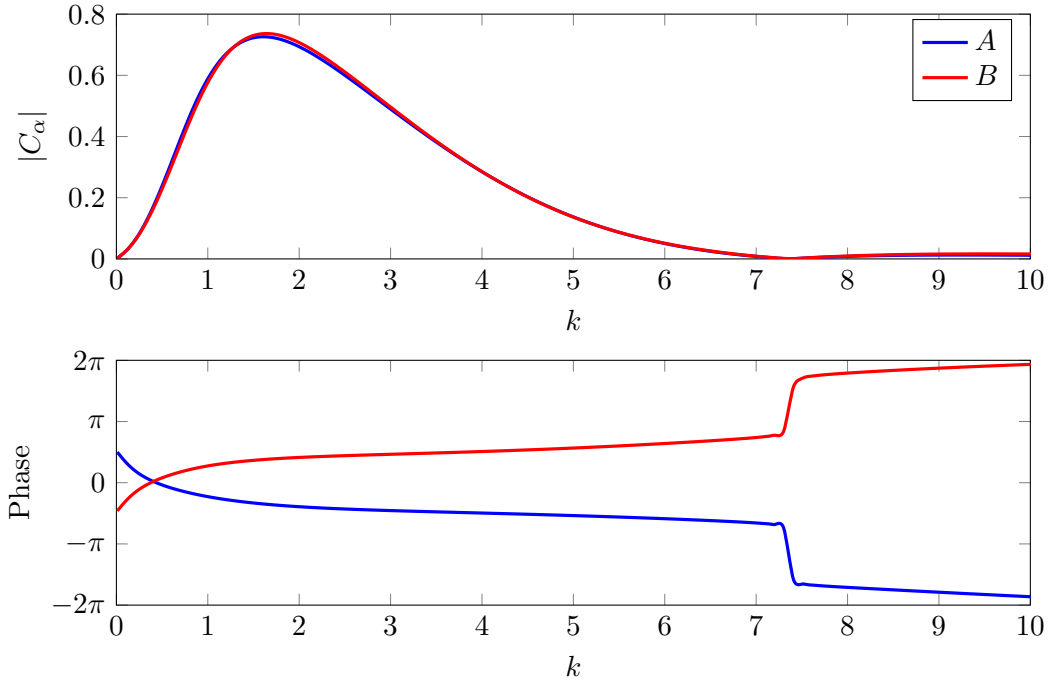

Figure 2.5: Continuous spectrum receptivity curves for $\lambda_k/3$ spanwise wavelength of the DNS results of Rizzetta & Visbal [50].

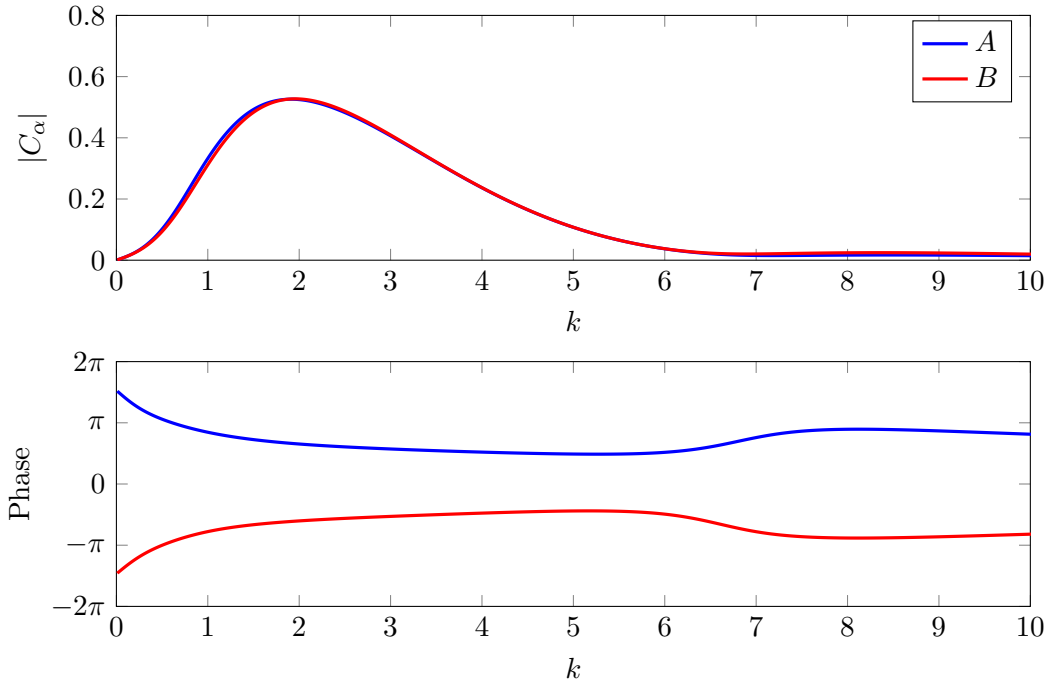

Figure 2.6: Continuous spectrum receptivity curves for $\lambda_k/4$ spanwise wavelength of the DNS results of Rizzetta & Visbal [50].

on the receptivity process.

To eliminate the receptivity question, optimal disturbances were developed to maximize the disturbance kinetic energy growth. Another method of solving the receptivity problem is to use linearized boundary conditions to decompose a roughness geometry into continuous spectrum modes of the LSEs. Unfortunately both approaches to receptivity do not well represent the experimental results.

Optimal disturbances excite slowly decaying continuous spectrum modes. These disturbances are located high in the boundary layer and must reach large amplitudes before secondary instabilities set in. On the other hand, linearized receptivity excites rapidly decaying continuous spectrum modes. These disturbances decay very quickly and do not grow enough to become unstable to secondary disturbances. Denissen & White [20] showed that realistic roughness-induced transient growth excites continuous spectrum modes with an intermediate decay rate. As a result, these realistic disturbances are much more unstable to secondary instabilities [24].

This suggests that the initial disturbance which maximizes the secondary instability growth rate may have commonality with observed roughness-induced transient growth. Finding these disturbances is the topic of this dissertation.

3. PROPAGATORS

A means of propagating an initial disturbance downstream is necessary to observe transient growth. There are several ways this can be accomplished. Two methods will be considered here: linear stability theory and marching of the parabolized Navier–Stokes (PNS) equations. Since the BiGlobal stability solver is only formulated for steady basic states, only steady disturbances will be considered. Additionally, the previous optimal disturbance work of Tumin & Reshotko [48] show that the disturbance kinetic energy growth is larger for steady than unsteady disturbances. This does not necessarily suggest that unsteady disturbances are more stable to secondary instabilities though. Although freestream turbulence induces unsteady disturbances in the boundary layer [40], subcritical roughness generates steady disturbances. [18, 19, 8] The accommodation of unsteady base flows in the BiGlobal secondary instability solver is not straight forward and therefore as a first step only steady transient growth is considered.

3.1 Linear Stability Theory

In the previous section transient growth was shown capable of being represented using solutions of the LSEs. The evolution of discrete and continuous spectrum modes of the LSEs can be used to propagate transiently growing steady disturbances downstream.

Using the parallel flow assumption, i.e. $\boldsymbol{V} = [U(y,z),\ 0,\ 0]^T$, initial velocity disturbances can be propagated downstream provided that the receptivity coefficients

and curves are known:

$$\mathbf{q}' = \int_\beta \left[\sum_v C_v \hat{\mathbf{q}}_v e^{i(\alpha_v x + \beta z)} + \sum_j \int_k C_j(k) \hat{\mathbf{q}}_j(k) e^{i[\alpha_j(k) x + \beta z]} dk \right] d\beta.$$

Since the base flow is decoupled from the disturbance quantities, the linear assumptions loses accuracy at large disturbance amplitudes. When using linear modes for the initial value problem, only small disturbance amplitudes can be examined. Non-parallel flows could be accommodated with linear stability theory [51, 52] but the treatment of non-parallel flows will instead be handled in a more straightforward manner by integrating the PNS equations.

Rizzetta & Visbal [50] performed a DNS of the experiment by Ergin & White [8]. These DNS results have been used by Denissen & White [20, 24] to study roughness receptivity and transient growth breakdown. Following Denissen & White [20], the DNS results have been decomposed into its continuous spectrum modes. The velocity field can then be reconstructed from these continuous spectra modes. Figure 3.1 compares the disturbance energy evolution for the first four spanwise wavelengths from the DNS and linearly reconstructed velocity fields. The decomposition was performed at $x - x_k = 25$ mm downstream of the roughness which enables accurate reconstruction of the disturbance energy evolution. Upstream of this location the flow is nonlinear due to the proximity of the roughness element and is not well-captured by linear theory. Far downstream in Fig. 3.1 the DNS and reconstructed disturbance energy evolution begins to show some slight deviation due to nonparallel growth not captured by the parallel flow linear theory.

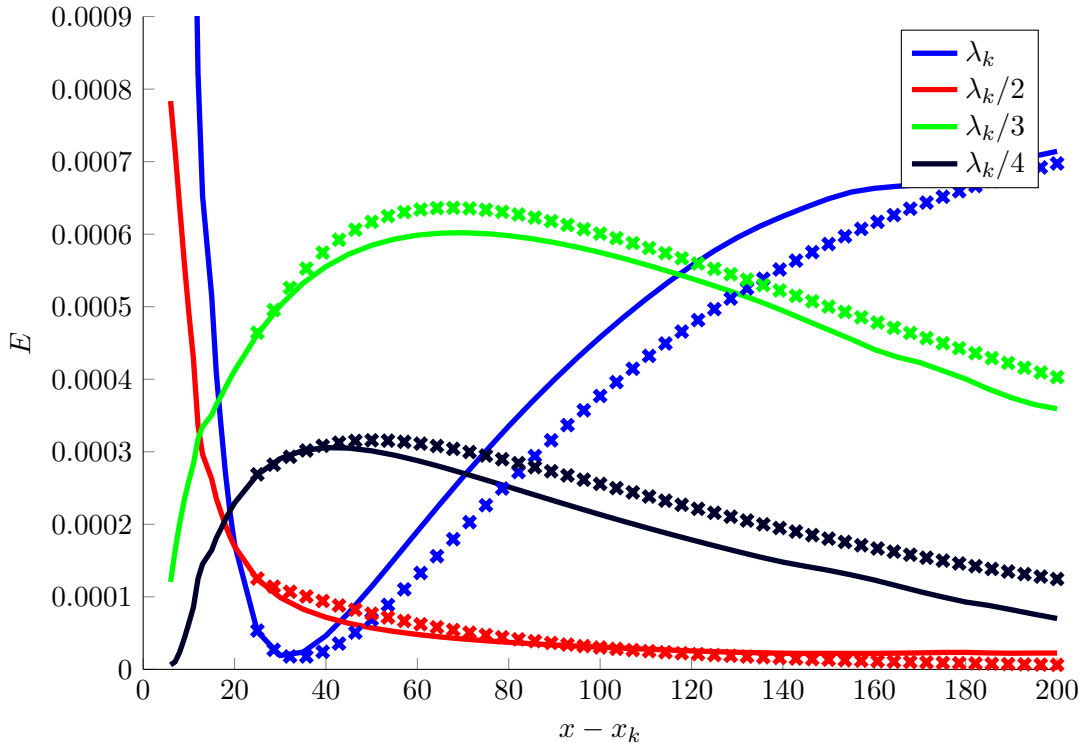

Figure 3.1: Comparison of disturbance energy evolution between the DNS of Rizzetta & Visbal [50] and linear theory. Initial condition for the linear theory was obtained using biorthogonal decomposition at $x - x_k = 25$ mm downstream of roughness. Lines are from DNS, crosses are from linear theory.

3.2 Parabolized Navier–Stokes (PNS) Equations

Since this research involves finding the optimal initial velocity disturbances that maximize secondary instabilities downstream, a method of propagating these steady velocity disturbances is needed. The steady Navier–Stokes equations for large Reynolds numbers with the flow primarily along one streamwise direction can be made parabolic [53]. Specifically, the viscous derivatives with respect to the streamwise direction are assumed to be much smaller than derivatives in the other two directions:

$$\frac{\partial}{\partial x} \ll \frac{\partial}{\partial y}, \frac{\partial}{\partial z}$$

$$\frac{\partial^2}{\partial x^2} \ll \frac{\partial^2}{\partial y^2}, \frac{\partial^2}{\partial z^2}.$$

Since the flow is incompressible, upstream influence due to the streamwise pressure gradient must be eliminated to ensure parabolic behavior of the equations in the streamwise direction. These assumptions result in the following governing equations for incompressible flat-plate flow:

$$\frac{\partial u}{\partial x} + \frac{\partial v}{\partial y} + \frac{\partial w}{\partial z} = 0$$

$$u\frac{\partial u}{\partial x} + v\frac{\partial u}{\partial y} + w\frac{\partial u}{\partial z} = -\frac{\partial p_\infty}{\partial x} + \frac{1}{Re}\left(\frac{\partial^2 u}{\partial y^2} + \frac{\partial^2 u}{\partial z^2}\right)$$

$$u\frac{\partial v}{\partial x} + v\frac{\partial v}{\partial y} + w\frac{\partial v}{\partial z} = -\frac{\partial p}{\partial y} + \frac{1}{Re}\left(\frac{\partial^2 v}{\partial y^2} + \frac{\partial^2 v}{\partial z^2}\right)$$

$$u\frac{\partial w}{\partial x} + v\frac{\partial w}{\partial y} + w\frac{\partial w}{\partial z} = -\frac{\partial p}{\partial z} + \frac{1}{Re}\left(\frac{\partial^2 w}{\partial y^2} + \frac{\partial^2 w}{\partial z^2}\right)$$

The PNS equations are written as general nonlinear equations and discretized using 4^{th}-order finite differences in the $y - z$ plane and 1^{st}-order backwards finite

differences in the x direction:

$$\boldsymbol{F}_i(\boldsymbol{Q}_0,\, \boldsymbol{Q}_1,\, \ldots,\, \boldsymbol{Q}_i) = \boldsymbol{0},$$

where $\boldsymbol{Q}_i = [u_i, v_i, w_i, p_i]^T$ and the subscript i indicates the streamwise position. The PNS equations are nonlinear functions of $\boldsymbol{Q}_i$ and Newton sub-iterations must be used to solve for $\boldsymbol{Q}_i$:

$$\frac{\partial \boldsymbol{F}_i}{\partial \boldsymbol{Q}_i}\Delta\boldsymbol{q} = -\boldsymbol{F}_i,$$

$$\boldsymbol{Q}_i^{(n+1)} = \boldsymbol{Q}_i^{(n)} + \Delta\boldsymbol{q}.$$

The solution is considered converged when:

$$\|\Delta\boldsymbol{q}\| < \epsilon_{\text{PNS}},$$

where $\epsilon_{\text{PNS}} \in [10^{-6},\, 10^{-3}]$ is chosen small enough to ensure converged results but large enough to avoid numerical round-off effects. For this numerical scheme to be stable, u_i must be strictly positive so that the parabolic nature of the equations is ensured. Methods for solving the PNS equations in reversed or separated flow conditions have been developed [54] but will not be considered here.

The PNS code developed for this research has been validated against two known solutions of the full Navier–Stokes equations — Blasius boundary layer flow and the DNS results of Rizzetta & Visbal [50]. Figure 3.2 shows the results of a solution of the PNS code which used the Blasius solution as an initial condition at $x = 300$ for a unit Reynolds number of 769 mm^{-1}. The displacement thickness (δ^*), momentum thickness (θ), and shape factor ($H = \delta^*/\theta$) all show near-exact agreement with Blasius theory.

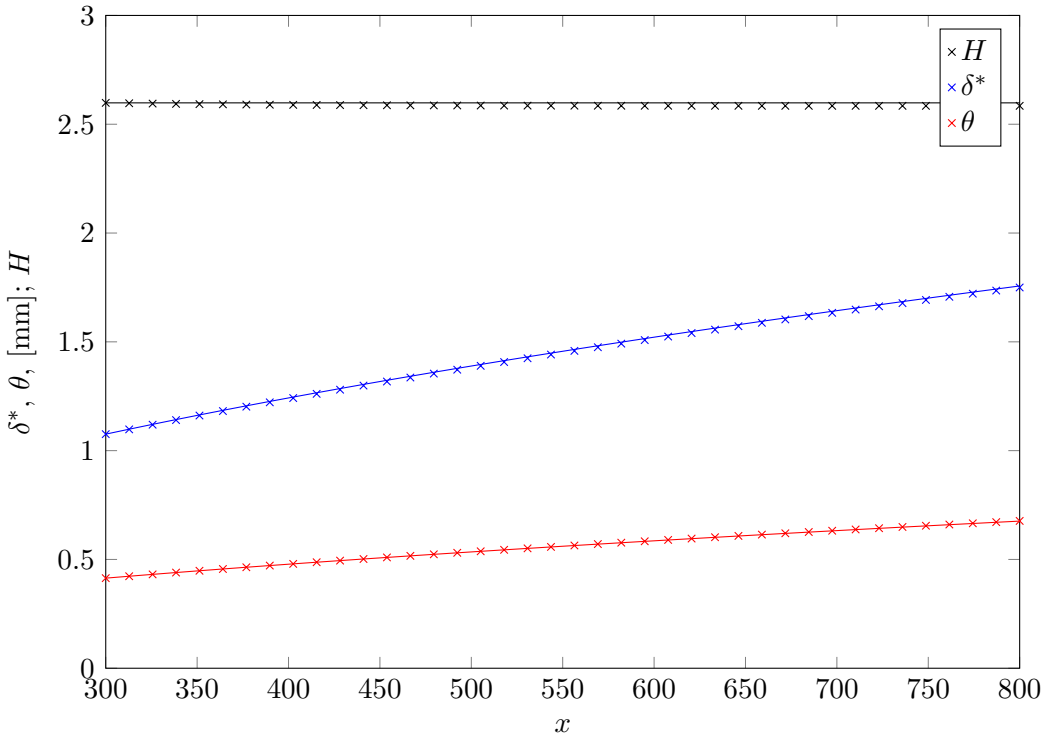

Figure 3.2: Initial condition was Blasius boundary layer solution at $x = 300$ for a unit Reynolds number of 769 mm^{-1}. PNS results are indicated by crosses and the Blasius theory is indicated by solid lines.

Figure 3.3 shows color contours of all three velocity components from the DNS results, 120 mm downstream of the roughness location. Overlaid are black contour lines from the PNS solution. The initial condition for the PNS equations was taken from the DNS results 12 mm downstream of the roughness. This is the first location where the DNS streamwise velocity is strictly positive, a necessary condition for the convergence of the PNS solution. At 120 mm downstream, only slight deviations between the two results are apparent. Figure 3.4 compares the DNS and PNS energy evolution for the first four spanwise wavelengths. Again, the initial condition for the PNS code was taken from the DNS results 12 mm downstream of the roughness.

Similar to Fig. 3.3, Fig. 3.5 shows color contours from the DNS results 120 mm downstream of the roughness location with black contour lines from the PNS solution overlaid. The initial condition for the PNS equations was taken from the DNS results 25 mm downstream of the roughness. Again only slight deviations between the two results are apparent at the 120 mm downstream. Figure 3.6 compares the DNS and PNS energy evolution for the first four spanwise wavelengths. In this plot, the initial condition for the PNS code was taken from the DNS results 25 mm downstream of the roughness. By moving the initial condition for the PNS code downstream the results become more accurate. This is because the streamwise viscous derivatives are likely more significant in the near wake of the roughness.

The PNS code is capable of accurately marching initial boundary layer solutions downstream as evidenced by the above comparisons to Blasius boundary-layer theory and the DNS results of Rizzetta & Visbal [50]. This provides confidence in the use of this PNS code in the optimization results to follow.

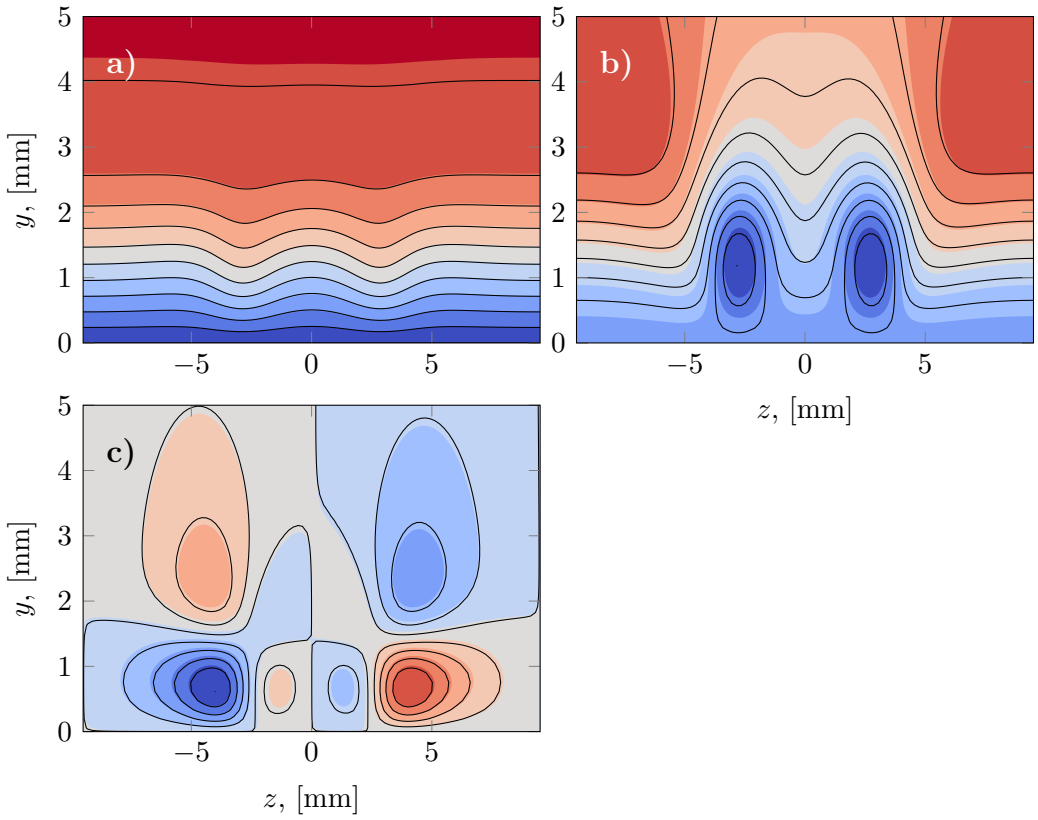

Figure 3.3: Velocity contours at $x - x_k = 120$ mm downstream of roughness. Color contours are from the DNS of Rizzetta & Visbal [50], lines are from PNS. Initial condition for the PNS is at $x - x_k = 12$ mm downstream of roughness. **a)** Streamwise velocity, U; **b)** spanwise velocity, V; **c)** wall-normal velocity, W.

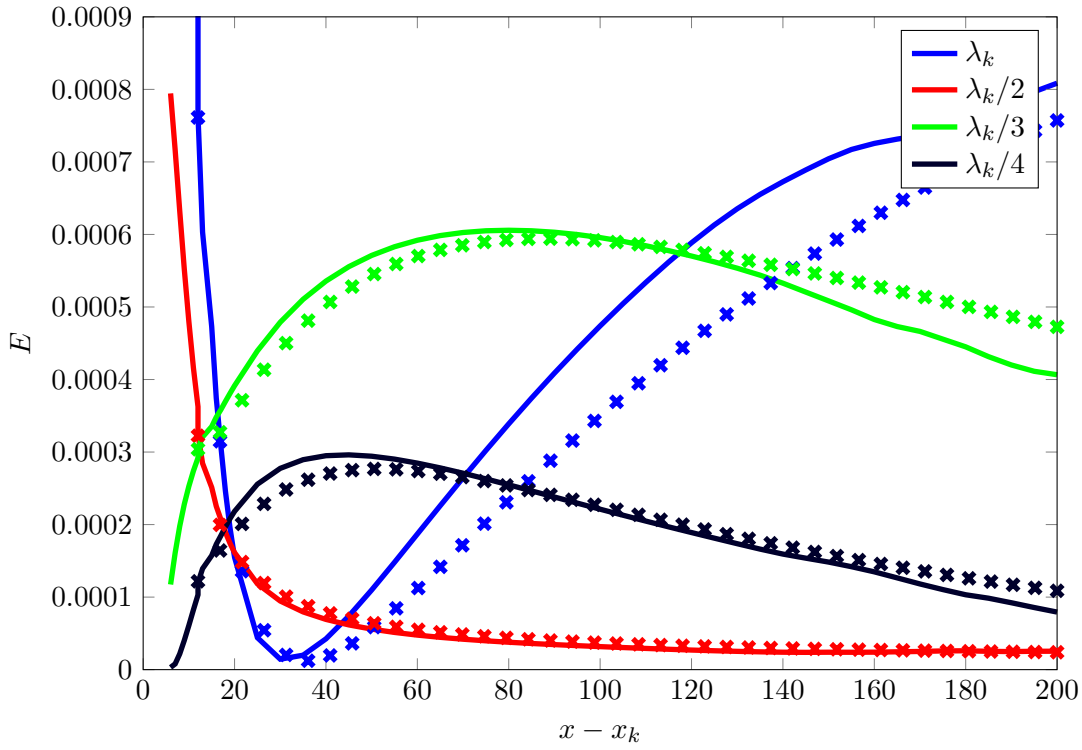

Figure 3.4: Comparison of disturbance energy evolution between the DNS of Rizzetta & Visbal [50] and PNS solutions. Initial condition for the PNS is at $x - x_k = 12$ mm downstream of roughness. Lines are from DNS, crosses are from PNS.

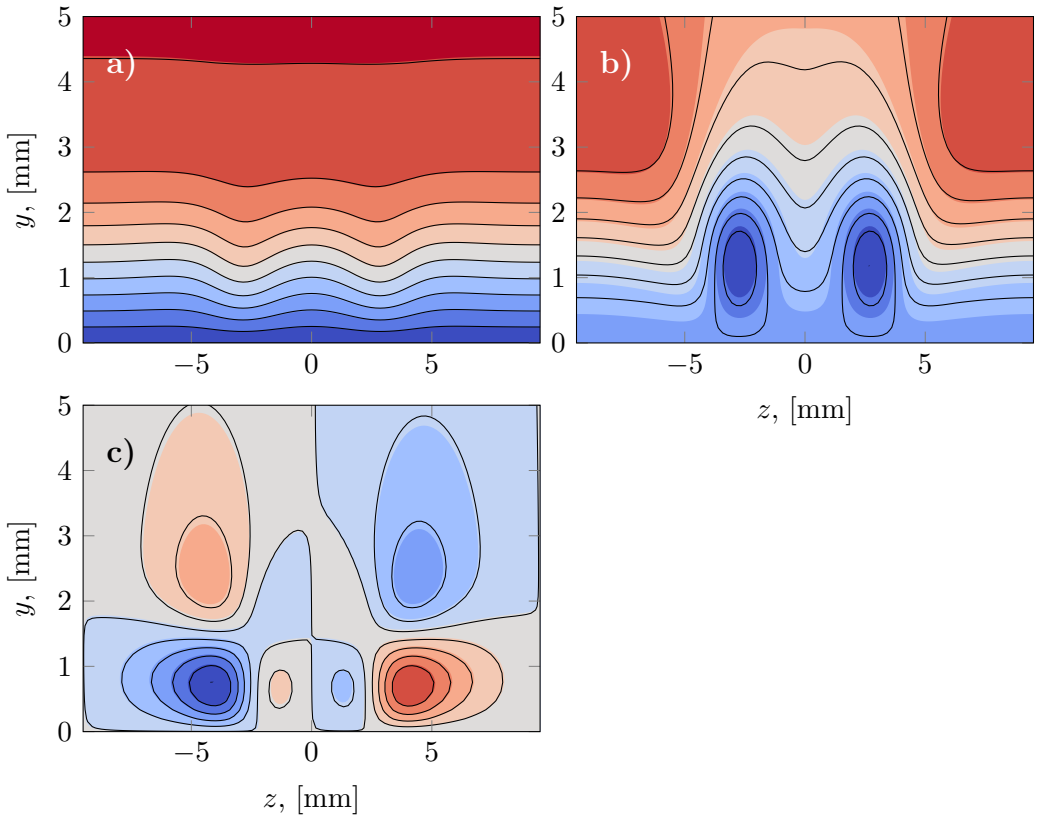

Figure 3.5: Velocity contours at $x - x_k = 120$ mm downstream of roughness. Color contours are from the DNS of Rizzetta & Visbal [50], lines are from PNS. Initial condition for the PNS is at $x - x_k = 25$ mm downstream of roughness. **a)** Streamwise velocity, U; **b)** spanwise velocity, V; **c)** wall-normal velocity, W.

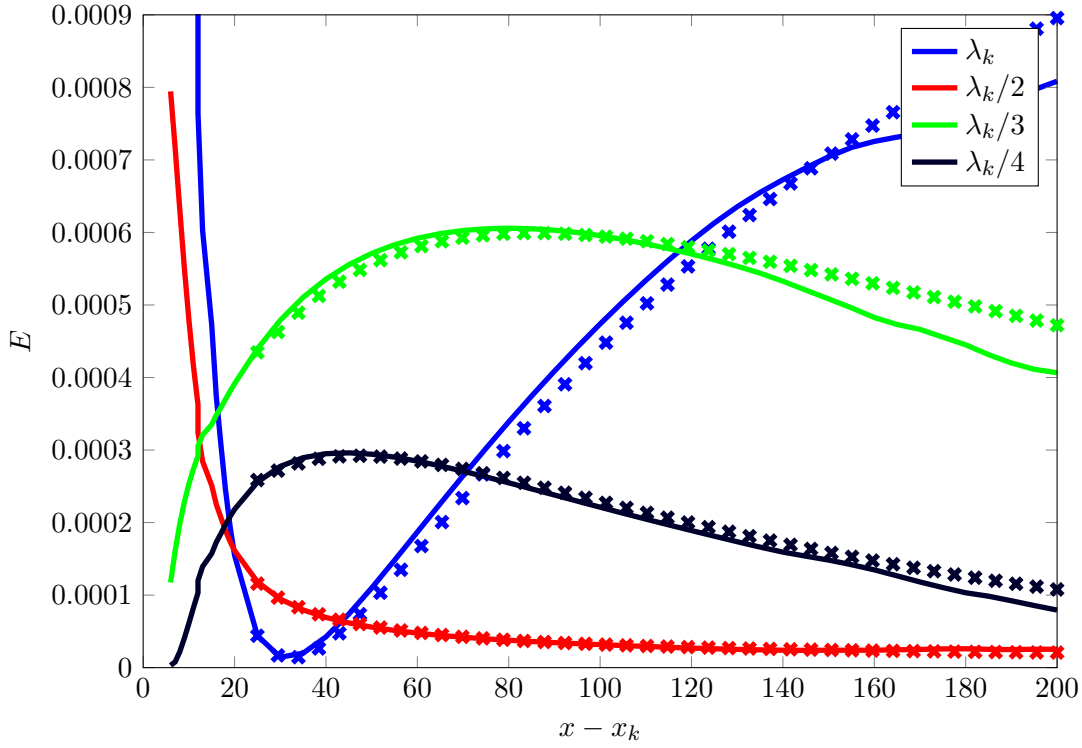

Figure 3.6: Comparison of disturbance energy evolution between the DNS of Rizzetta & Visbal [50] and PNS solutions. Initial condition for the PNS is at $x - x_k = 25$ mm downstream of roughness. Lines are from DNS, crosses are from PNS.

4. BIGLOBAL SECONDARY INSTABILITIES

Transient growth is characterized by algebraic disturbance growth followed by exponential decay. The process of transient growth alone does not lead to transition. However, if the algebraic disturbance growth is large enough, the distorted boundary layer can be unstable to "secondary instabilities." Secondary instabilities is in quotes because transient growth itself is not a primary instability.

TS wave growth rates and mode shapes are eigenvalue solutions of the one-dimensional LSEs. In an entirely similar process, "secondary instabilities" of transient growth can be found as eigenvalue solutions of the two-dimensional, or BiGlobal, LSEs. In this section, the detailed development of a BiGlobal secondary instability code is outlined. The code is validated against both incompressible and hypersonic experimental transient growth results.

4.1 Derivation of Stability Equations

To begin, the dimensional Navier–Stokes equations are reduced to non-dimensional form through the following scalings (tildes indicate dimensional quantities): The velocity vector is non-dimensionalized by the reference velocity, $\tilde{U}_{\text{ref}}$, lengths by the reference length, $\tilde{L}_{\text{ref}}$, the pressure by $\tilde{\rho}_{\text{ref}}\tilde{U}_{\text{ref}}^2$, time by $\tilde{L}_{\text{ref}}/\tilde{U}_{\text{ref}}$, and $\tilde{\lambda}$ by $\tilde{\mu}_{\text{ref}}$. All other quantities are non-dimensionalized by their corresponding reference values. Ideal gases are assumed. The non-dimensional compressible Navier–Stokes equations are: [55]

$$\frac{\partial \rho}{\partial t} + \nabla \cdot (\rho \boldsymbol{v}) = 0, \tag{4.1}$$

$$\rho \left[\frac{\partial \boldsymbol{v}}{\partial t} + (\boldsymbol{v} \cdot \nabla) \boldsymbol{v} \right] = -\nabla p + \frac{1}{\text{Re}_{\tilde{L}_{\text{ref}}}} \nabla \cdot \left[\mu \left(\nabla \boldsymbol{v} + \nabla \boldsymbol{v}^T \right) + \lambda \left(\nabla \cdot \boldsymbol{v} \right) \boldsymbol{I} \right], \tag{4.2}$$

$$\rho\left[\frac{\partial T}{\partial t}+(\boldsymbol{v}\cdot\nabla)\,T\right]=(\gamma-1)\,M_{\mathrm{ref}}^{2}\left(\frac{\partial p}{\partial t}+(\boldsymbol{v}\cdot\nabla)\,p\right)+\frac{1}{\mathrm{Re}_{\tilde{L}_{\mathrm{ref}}}\mathrm{Pr}}\nabla\cdot(k\nabla T)$$
$$+\frac{(\gamma-1)\,M_{\mathrm{ref}}^{2}}{\mathrm{Re}_{\tilde{L}_{\mathrm{ref}}}}\left(\frac{\mu}{2}\,\mathrm{Tr}\left\{\left[\nabla\boldsymbol{v}+(\nabla\boldsymbol{v})^{T}\right]^{2}\right\}+\lambda\,(\nabla\cdot\boldsymbol{v})^{2}\right),\quad(4.3)$$

$$\gamma M_{\mathrm{ref}}^{2}p=\rho T,\quad(4.4)$$

where $\mathrm{Re}_{\tilde{L}_{\mathrm{ref}}}$ is the Reynolds number based on $\tilde{L}_{\mathrm{ref}}$, $\mathrm{Pr}=\tilde{\mu}\tilde{C}_p/\tilde{k}$ is the Prandtl number, γ is the ratio of specific heats, M_{ref} is the Mach number based on reference velocity and temperature, $\boldsymbol{I}$ is the identity matrix, and Tr indicates the matrix trace operation. In general, the Prandtl number is non-constant. However, restricting calculations to air, a constant value of $\mathrm{Pr}=0.72$ and $\gamma=1.4$ is assumed. The non-dimensional dynamic viscosity coefficient is given as a function of temperature using Sutherland's law:

$$\mu=T^{\frac{3}{2}}\left(\frac{T_{\mathrm{ref}}+S}{T_{\mathrm{ref}}T+S}\right),$$

where $S=110.4$ K is the Sutherland temperature. The second coefficient of viscosity is found using Stokes' hypothesis, $\lambda=-\frac{2}{3}\mu$.

The velocity, density, pressure, temperature, thermal conductivity, and viscosity coefficients are separated into mean and fluctuating components:

$$q=\overline{q}(\xi,\eta,\zeta)+\epsilon q'(\xi,\eta,\zeta,t)$$

where ϵ is a small parameter, q represents the unknown variable, and ξ, η, and ζ are the coordinates of a general curvilinear coordinate system. Substituting the perturbed quantities into Eqs. (4.1)-(4.4) and extracting the $O(\epsilon)$ terms yields the linearized Navier–Stokes equations:

$$\frac{\partial\rho'}{\partial t}+\nabla\cdot\left(\rho'\overline{\boldsymbol{V}}+\overline{\rho}\boldsymbol{v}'\right)=0,\quad(4.5)$$

$$\overline{\rho}\left[\frac{\partial \boldsymbol{v}'}{\partial t}+\boldsymbol{v}'\cdot\nabla\overline{\boldsymbol{V}}+\overline{\boldsymbol{V}}\cdot\nabla\boldsymbol{v}'\right]+\rho'\overline{\boldsymbol{V}}\cdot\nabla\overline{\boldsymbol{V}}=-\nabla p'$$
$$+\frac{1}{\mathrm{Re}_{\tilde{L}_{\mathrm{ref}}}}\nabla\cdot\left[\overline{\mu}\left(\nabla\boldsymbol{v}'+\nabla\boldsymbol{v}'^{T}\right)+\mu'\left(\nabla\overline{\boldsymbol{V}}+\nabla\overline{\boldsymbol{V}}^{T}\right)+\left(\overline{\lambda}\nabla\cdot\boldsymbol{v}'+\lambda'\nabla\cdot\overline{\boldsymbol{V}}\right)\boldsymbol{I}\right], \quad (4.6)$$

$$\begin{aligned}\overline{\rho}\left[\frac{\partial T'}{\partial t}+\boldsymbol{v}'\cdot\nabla\overline{T}+\overline{\boldsymbol{V}}\cdot\nabla T'\right]+\rho'\overline{\boldsymbol{V}}\cdot\nabla\overline{T}&=(\gamma-1)M_{\mathrm{ref}}^2\left(\frac{\partial p'}{\partial t}+\overline{\boldsymbol{V}}\cdot\nabla p'+\boldsymbol{v}'\cdot\nabla\overline{p}\right)\\&+\frac{1}{\mathrm{Re}_{\tilde{L}_{\mathrm{ref}}}\mathrm{Pr}}\nabla\cdot\left[k'\nabla\overline{T}+\overline{k}\nabla T'\right]\\&+\frac{(\gamma-1)M_{\mathrm{ref}}^2}{\mathrm{Re}_{\tilde{L}_{\mathrm{ref}}}}\Bigg(\overline{\mu}\,\mathrm{Tr}\left\{\left[\nabla\overline{\boldsymbol{V}}+\left(\nabla\overline{\boldsymbol{V}}\right)^{T}\right]\left[\nabla\boldsymbol{v}'+\left(\nabla\boldsymbol{v}'\right)^{T}\right]\right\}\\&+\frac{\mu'}{2}\,\mathrm{Tr}\left\{\left[\nabla\overline{\boldsymbol{V}}+\left(\nabla\overline{\boldsymbol{V}}\right)^{T}\right]^2\right\}+2\overline{\lambda}\left[\nabla\cdot\overline{\boldsymbol{V}}\right]\left[\nabla\cdot\boldsymbol{v}'\right]+\lambda'\left[\nabla\cdot\overline{\boldsymbol{V}}\right]^2\Bigg),\end{aligned} \quad (4.7)$$

Density fluctuations are eliminated through the use of the linearized ideal gas equation of state, Eq. (4.8).

$$\rho'=\frac{\gamma M_{\mathrm{ref}}^2}{\overline{T}}p'-\overline{\rho}\frac{T'}{\overline{T}}. \quad (4.8)$$

By formulating the linearized Navier–Stokes equations in terms of general curvilinear coordinates, Eqs. (4.5)-(4.8) apply to a variety of geometries by substituting the correct tensor calculus operators. Appendix A.3 provides an overview of finding these operators using covariant differentiation [56] which is used in this dissertation.

The linearized Navier–Stokes equations and associated stability eigenproblems, are greatly simplified assuming incompressibility, specifically, the following assumptions are made: $\rho'=0$, $\overline{\rho}=1$, $\mu'=0$, $\overline{\mu}=1$, and $\lambda'=0$. This results in the following continuity and momentum equations:

$$\nabla\cdot\boldsymbol{v}'=0, \quad (4.9)$$

$$\left[\frac{\partial \boldsymbol{v}'}{\partial t}+\boldsymbol{v}'\cdot\nabla\overline{\boldsymbol{V}}+\overline{\boldsymbol{V}}\cdot\nabla\boldsymbol{v}'\right]=-\nabla p'+\frac{1}{\mathrm{Re}_{\tilde{L}_{\mathrm{ref}}}}\left[\nabla^2\boldsymbol{v}'+\nabla\cdot\left(\nabla\boldsymbol{v}'\right)^{T}\right]. \quad (4.10)$$

The momentum and continuity equations are no longer coupled to the equation of state and energy equation and can be solved separately.

Boundary-layer flows are considered in the present work in which the parallel flow assumption is made:

$$\overline{\boldsymbol{V}} = \left[\overline{U}(\eta,\zeta),\ 0,\ 0\right]^T.$$

The reference values for non-dimensionalization are the boundary-layer edge values and the reference length is $\tilde{L}_{\text{ref}}^2 = \tilde{\delta}^2 = \tilde{\nu}_e\left(\tilde{x} - \tilde{x}_{\text{vle}}\right)/\tilde{U}_e$, where subscript e indicates edge conditions and $\tilde{x}$ is the streamwise distance downstream of the physical leading edge and $\tilde{x}_{\text{vle}}$ is the virtual leading edge location. The static pressure is assumed constant across the boundary layer, $\overline{p} = 1/\gamma M_e^2$ and $\overline{\rho} = 1/\overline{T}$ [57, 55].

In the case of boundary-layer flow in a Cartesian coordinate system, $(x,\ y,\ z)$, the inviscid linearized Navier–Stokes equations for an ideal gas can be reduced to a single equation for the pressure fluctuations:

$$\left(\frac{\partial}{\partial t} + \overline{U}\frac{\partial}{\partial x}\right)\nabla\cdot\left(\overline{T}\nabla p'\right) = 2\overline{T}\frac{\partial\overline{U}}{\partial y}\frac{\partial^2 p'}{\partial x\partial y} + 2\overline{T}\frac{\partial\overline{U}}{\partial z}\frac{\partial^2 p'}{\partial x\partial z} + M_e^2\left(\frac{\partial}{\partial t} + \overline{U}\frac{\partial}{\partial x}\right)^3 p'. \quad (4.11)$$

In the incompressible limit, Eq. (4.11) converges to the equation previously used by Hall & Horseman [58] and Henningson [59]. Analytical continuation [21] is necessary to obtain neutral and damped modes due to a logarithmic singularity in Tollmien's inviscid solutions [60]. Solving this single inviscid equation for pressure fluctuations is preferable to solving Eqs. (4.5)–(4.8) in the inviscid limit since the pressure gradients are much smaller than the velocity gradients and easier to resolve numerically, especially in the vicinity of the critical layer.

The preceding summary of linearized Navier–Stokes equations makes no refer-

ence to stability. Eqs. (4.5)-(4.8) are inhomogeneous in two directions under the boundary-layer approximations and accept a normal mode substitution:

$$\boldsymbol{q}'(\xi,\eta,\zeta,t) = \hat{\boldsymbol{q}}(\eta,\zeta)e^{i(\alpha\xi-\omega t)} + c.c.,$$

where $\boldsymbol{q}' = [u', v', w', p', T']^T$, α is the wavenumber associated with ξ, ω is the temporal wavenumber, and $c.c.$ is the complex-conjugate. In general both α and ω are complex-valued. For temporal stability $\alpha \in \mathbb{R}$, $\omega \in \mathbb{C}$ and for spatial stability $\alpha \in \mathbb{C}$, $\omega \in \mathbb{R}$. Experiments have shown that spatial stability is a better approximation for boundary layers [3]. Using the normal mode substitution yields a generalized eigenvalue problem:

$$\boldsymbol{A}\hat{\boldsymbol{q}} = \lambda \boldsymbol{B}\hat{\boldsymbol{q}},$$

where λ is α in the case of spatial stability and ω or c in the case of temporal stability. The eigenvalue appears nonlinearly in the spatial stability problem and in Eq. 4.11 and is handled through the use of companion matrices [61].

Oftentimes for spatial stability it is more convenient to work with the frequency, $\tilde{f}$ or F, instead of ω. The non-dimensional frequency is defined as:

$$F = \frac{2\pi\tilde{f}}{\mathrm{Re}'\tilde{U}_e} = \frac{\omega}{\mathrm{Re}_{\tilde{\delta}}},$$

where $\mathrm{Re}' = \tilde{U}_e/\tilde{\nu}$ is the unit Reynolds number. To facilitate comparison between solvers, temporal growth rates are approximately converted to spatial growth rates using Gaster's transformation [60].

4.2 Numerical Methods

The incompressible version of Eq. 4.11 has been solved using Floquet theory for periodic basic states in the spanwise direction and Chebyshev collocation in the wall-normal-direction [21, 62]. This results in a generalized eigenvalue problem with a block-diagonal matrix structure and poor sparsity. Significant computational performance improvement can be achieved by using high-order finite differences [53] instead of a Floquet approach. Finite-differences naturally result in sparse matrices allowing for efficient algorithms that do not perform operations on zero-valued elements. Very high-order finite difference methods can become unstable near the boundaries of the domain. To resolve this, the FD-q method [63] is used in the wall-normal direction to ensure uniform interpolation errors in the finite-difference approximations. For the experiments analyzed in this section, the basic state is periodic in the z-direction and standard high-order finite differences on a uniform grid with periodic boundary conditions are used. Fourth-order finite differences were used in all problems presented in this section.

A rational mapping [60] from $\grave{\eta} \in [-1,\ 1]$ to η is used which clusters points within the boundary layer for the wall-normal direction:

$$\eta = a\frac{1+\grave{\eta}}{b-\grave{\eta}} \qquad a = \frac{\eta_i \eta_{\max}}{\eta_{\max} - 2\eta_i} \qquad b = 1 + \frac{2a}{\eta_{\max}}.$$

The values of η_i and $\eta_{\max}$ roughly correspond to the boundary layer thickness, δ_{99}, and three to four times δ_{99}, respectively. Results presented in this section use between 150 and 250 discretization points in both the spanwise and wall-normal directions.

The sparse matrices are constructed using Tpetra, a templated distributed sparse matrix package within the Trilinos project [64]. The generalized eigenvalue problem is solved using the Arnoldi iteration method [65].

To target specific internal eigenvalues near σ, a shift-invert transformation is used:

$$\boldsymbol{A}\boldsymbol{x} = \lambda \boldsymbol{B}\boldsymbol{x} \qquad \longrightarrow \qquad \boldsymbol{C}\boldsymbol{x} = \left(\boldsymbol{A} - \sigma \boldsymbol{B}\right)^{-1} \boldsymbol{B}\boldsymbol{x} = \frac{1}{\lambda - \sigma}\boldsymbol{x}. \tag{4.12}$$

This transformation maps eigenvalues near σ towards infinity and leads to rapid convergence for the Arnoldi iterations. In practice, σ is chosen corresponding to a phase speed $c_r \in [U_{\min},\, U_{\max}]$. At every iteration, the matrix $\boldsymbol{A} - \sigma \boldsymbol{B}$ must be inverted. A one-time LU decomposition is computed using PARDISO [66, 67, 68], a multi-threaded sparse LU decomposition library. Each Arnoldi iteration uses forward and backward substitution of the LU decomposition to solve this equation:

$$\boldsymbol{b}_{i+1} = \left(\boldsymbol{A} - \sigma \boldsymbol{B}\right)^{-1} \boldsymbol{B}\boldsymbol{b}_i,$$

which is then used to form a Krylov subspace [69]:

$$\mathcal{K}_n\left(\boldsymbol{C},\, \boldsymbol{b}_0\right) = \operatorname{span}\left\{\boldsymbol{b}_0,\, \boldsymbol{C}\boldsymbol{b}_0,\, \boldsymbol{C}^2\boldsymbol{b}_0,\, \ldots,\, \boldsymbol{C}^{n-1}\boldsymbol{b}_0\right\} = \operatorname{span}\left\{\boldsymbol{b}_0,\, \boldsymbol{b}_1,\, \boldsymbol{b}_2,\, \ldots,\, \boldsymbol{b}_{n-1}\right\}.$$

From this subspace an orthonormal basis is extracted into the matrix $\boldsymbol{V}_n$ using Gram–Schmidt orthonormalization. The problem is then projected onto the upper Hessenberg matrix $\boldsymbol{H}_n$:

$$\boldsymbol{V}_n^H \boldsymbol{C} \boldsymbol{V}_n = \boldsymbol{H}_n.$$

For sufficiently large n, the eigenvalues of $\boldsymbol{H}_n$ are approximately equal to the largest eigenvalues of $\boldsymbol{C}$. Since $\boldsymbol{H}_n$ is an $n \times n$ matrix, dense eigenvalue methods can be used to quickly obtain these approximate eigenvalues and eigenvectors. If $\boldsymbol{y}^{(j)}$ denotes the j^{th} eigenvector of the matrix $\boldsymbol{H}_n$, the corresponding eigenvector to the original

problem is found as:

$$\boldsymbol{x}^{(j)} = \boldsymbol{V}_n \boldsymbol{y}^{(j)}.$$

The Arnoldi iteration method produces an unordered set of eigenvalues and corresponding eigenvectors. Many of the results below consider the behavior of these modes as a parameter such as $\mathrm{Re}_{\tilde{\delta}}$ or F is varied. Thus, a method of tracking the instability modes is necessary. There are several potential tracking methods including nearest neighbor searches using eigenvalue perturbation methods or linear extrapolation. The current approach uses correlation of the $\hat{u}$ disturbance quantities. The correlation of two mode shapes is computed using:

$$\left\langle \hat{u}^{(1)},\ \hat{u}^{(2)} \right\rangle = \left| \frac{\mathrm{cov}\left(\hat{u}^{(1)},\ \hat{u}^{(2)}\right)}{\sqrt{\mathrm{cov}\left(\hat{u}^{(1)},\ \hat{u}^{(1)}\right) \mathrm{cov}\left(\hat{u}^{(2)},\ \hat{u}^{(2)}\right)}} \right|,$$

where cov indicates covariance. Matching progresses in order of growth rate with the most unstable modes matched first. If multiple modes from the second set have a correlation greater than 0.65 with a mode from the first set, the matching mode is selected using a nearest neighbor search of a linear extrapolation of this subset of eigenvalues.

Later in this work, the BiGlobal code will be used to compute transient disturbances that maximize secondary instability growth rates. Since the optimization will require many executions of the BiGlobal code, it must be efficient. Table 4.1 shows typical solution times and peak memory usage for all solvers. The inviscid solvers are nearly an order-of-magnitude faster than the viscous solvers. However, the inviscid mode shapes do not compare as well with the experimental data. This comparison is shown in the next section.

In this section, two coordinate systems are used: Cartesian coordinates, $(x,\ y,\ z)$,

Table 4.1: Typical single solution times of the BiGlobal stability solvers for all combinations of inviscid/viscous, temporal/spatial, and incompressible/compressible assumptions. Measurements are based on computations of the low-speed discrete roughness wake using a 150×150 grid, 4^{th}-order finite differences, Krylov-subspace length of 100, and 8 threads.

Viscous	Spatial	Compressible	Time, [s]	Peak Memory, [GB]
			6	0.3
	X		11	0.6
		X	12	0.6
	X	X	13	0.7
X			46	2.0
X	X		54	2.5
X		X	106	3.5
X	X	X	115	4.3

for the flat-plate data and orthogonal coordinates, $(x,\ y,\ \phi)$, for the cone geometry. For the flat-plate, the x coordinate is aligned with the freestream direction, y is the coordinate normal to the wall, and z is the spanwise coordinate. The cone coordinate system is defined by its transformation to Cartesian coordinates $\bar{x}^j$:

$$\bar{x}^1 = x\cos\theta - y\sin\theta$$

$$\bar{x}^2 = -(R + y\cos\theta + x\sin\theta)\sin\phi$$

$$\bar{x}^3 = (R + y\cos\theta + x\sin\theta)\cos\phi,$$

where x is the distance along the surface of the cone from the measurement plane, y is the wall-normal distance from the surface of the cone, ϕ is the azimuthal coordinate, θ is the cone half-angle, and R is the cone radius at the measurement plane.

4.3 Low-Speed Secondary Instabilities

In a recent low-speed experiment, Kuester & White [70] examined the "shielding" effect of small distributed roughness around larger amplitude discrete roughness in

the Texas A&M University Klebanoff–Saric Wind Tunnel [71]. The authors tested three different spanwise-periodic roughness configurations, a deterministic distributed roughness patch, a slanted rectangle, and the combination of the two by taking detailed hot-wire measurements at multiple streamwise locations in the wake. For each case, the periodic spanwise wavelength was 32 mm. The 1 mm tall discrete roughness was located 918 mm downstream of the leading edge and the 0.85 mm tall distributed roughness between 878 and 1006 mm downstream of the leading edge. The roughness was manufactured using rapid prototyping and installed flush in a flat-plate boundary layer. Only the discrete and combined roughness cases will be considered.

Tests were performed at $\mathrm{Re}' = 544.3$ mm^{-1} and $\mathrm{Re}' = 690.5$ mm^{-1} resulting in roughness Reynolds numbers of $\mathrm{Re}_{kk} = 151$ and $\mathrm{Re}_{kk} = 220$. At $\mathrm{Re}_{kk} = 151$, both roughness configurations generated low- and high-speed streaks in the boundary layer but did not cause transition. At $\mathrm{Re}_{kk} = 220$, both roughness configurations generated a turbulent wedge downstream. For the discrete configuration, the wedge formed 15 boundary layer thicknesses downstream, whereas for the combined roughness, transition was delayed by 2 boundary layer thicknesses due to a weak shielding effect whereby the distributed roughness reduced the wake instability of the discrete element [72]. The measured unsteady disturbance growth also suggests a smaller instability growth rate in the wake of the combined compared to the discrete roughness.

Figure 4.1a shows lines of steady contours of $\overline{U}$ and color contours of u'_{rms} at $\tilde{x} = 950$ mm for the discrete roughness configuration. Figure 4.1b shows the basic state at $\tilde{x} = 950$ mm for the combined roughness configuration. Weaker gradients are visible in the "combined" roughness basic state which is caused by the shielding effect. The wakes are asymmetric because of the asymmetry in the slanted rectangle discrete roughness. Most of the results presented in the next section correspond to

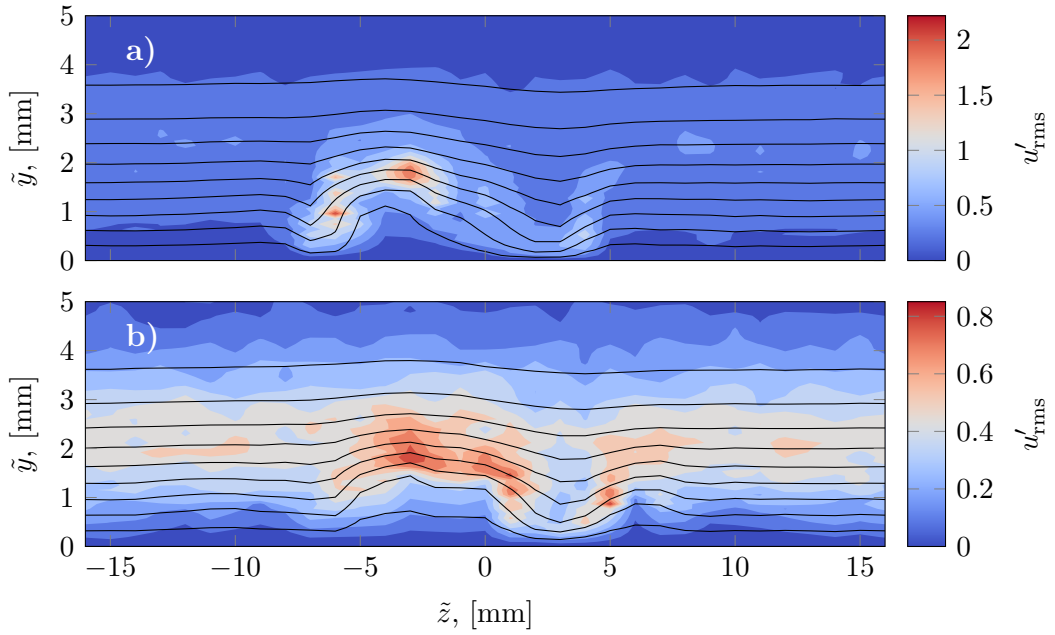

Figure 4.1: Experimental incompressible phase-lock averaged basic states and streamwise fluctuations from Kuester & White [70]. Lines are steady contours of $\overline{U}$, colors are contours of u'_{rms}. **a)** Discrete roughness basic state at $\tilde{x} = 950$ mm. **b)** Combined roughness basic state at $\tilde{x} = 950$ mm.

the basic states at this streamwise location.

For the low-speed discrete roughness case, there are two unstable modes at $\tilde{x} = 950$ mm. The most unstable is a varicose-type instability and the more stable mode is of sinuous-type. The asymmetry of the basic state precludes any symmetry assumptions in the computations and makes distinguishing varicose and sinuous instabilities difficult. Nevertheless, examining the two modes shown in Fig. 4.2 both varicose and sinuous characteristics can be seen. The varicose-type mode has a large center lobe with two smaller amplitude and nearly 180° out-of-phase side lobes. The sinuous-type mode has two large lobes that are nearly 180° out-of-phase with each other.

The color contours of u'_{rms} in Fig. 4.1 include contributions from the entire frequency range. For more meaningful comparisons to the BiGlobal calculations, the

unsteady fluctuations for both roughness configurations have been digitally filtered between $430 - 470$ Hz. The growth of the filtered unsteady disturbance energy for the discrete roughness case is plotted along with the spatial growth rate of the most unstable mode at $\tilde{x} = 950$ mm and $\tilde{f} = 450$ Hz from the BiGlobal stability calculations for each solver in Fig. 4.3. Although the BiGlobal growth rates are slightly lower than seen in the experiment, the agreement is quite good. The discrepancy may result from the parallel flow assumption, nonlinear effects, and additional energy content from the sinuous instability.

The filtered unsteady fluctuations are compared to the most unstable BiGlobal mode shapes for all solvers at matching frequencies in Fig. 4.4 for the discrete roughness configuration and in Fig. 4.5 for the combined roughness configuration. All mode shapes are similar but there is a noticeable distinction between the two inviscid modes and the two viscous modes. The calculated varicose-type viscous mode shapes agree very well with the measured unsteady fluctuations for both roughness configurations.

Additionally, spatial N-factors based on measurements at $\tilde{x} = 928$, 935, 942.5, and 950 mm were computed for several unstable modes and are compared to the experimental temporal power spectrum measured in the vicinity of the largest unsteady fluctuations in Figs. 4.6 and 4.7 for the discrete and combined roughness cases, respectively. The agreement between the experimental power spectra and the BiGlobal spatial N-factors is excellent.

Kuester & White [70] observed that the lower-amplitude distributed roughness "shielded" the larger-amplitude discrete roughness in the combined case. In agreement with this observation, the largest N-factor computed for the combined roughness case is about 10% less than the largest for the discrete case. However, there are two additional unstable modes (referred to as mode III and mode IV) present in the

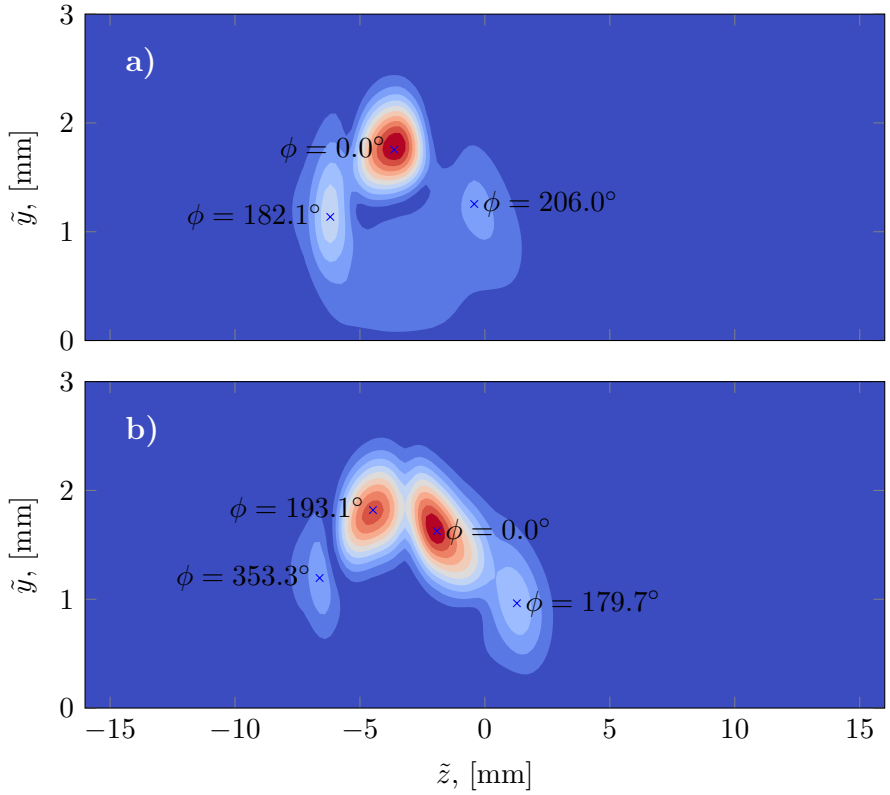

Figure 4.2: BiGlobal mode shapes computed for the low-speed, discrete roughness case at $\tilde{f} = 450$ Hz and $\tilde{x} = 950$ mm using the incompressible, viscous, spatial solver. Colors indicate $|\hat{u}|$ and the relative phase, ϕ, of $\hat{u}$ is indicated for the main lobes. **a)** Varicose-type mode. **b)** Sinuous-type mode.

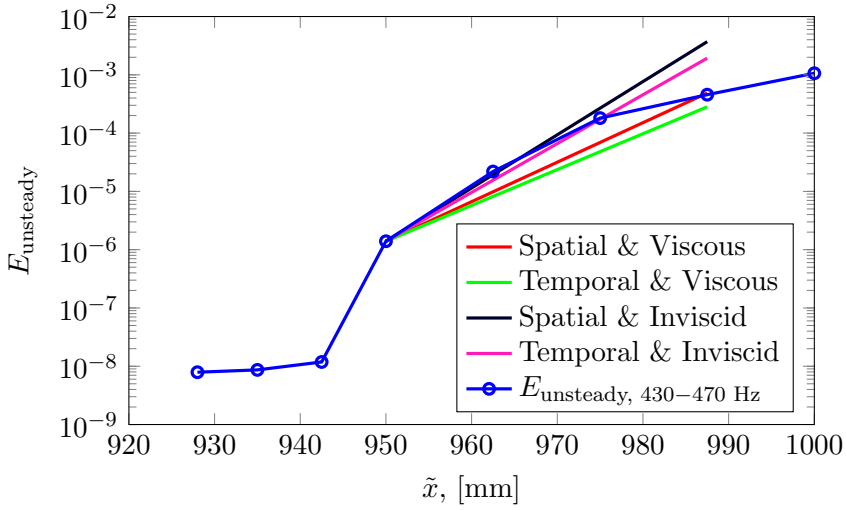

Figure 4.3: Comparison of experimentally measured energy evolution and BiGlobal growth rates for all solvers for the discrete roughness case. Stability calculations were performed for $\tilde{f} = 450$ Hz at $\tilde{x} = 950$ mm, blue lines are experimental unsteady disturbance energy over a narrow frequency band.

combined roughness case that were not present in the discrete case.

4.4 High-Speed Secondary Instabilities

Separately, Sharp [73] conducted a hypersonic roughness experiment in the Texas A&M Mach 6 Quiet Tunnel [74]. The experiment measured the transiently growing wake of an azimuthally spaced array of 18 cube-like discrete roughness elements on a slightly blunted 5° half-angle straight cone. The roughness height is approximately equal to the boundary-layer thickness at the roughness location. Detailed wake measurements were obtained using a Pitot probe mounted on an azimuthal traverse. Despite the limited (~40 second) run time of the facility, detailed contour maps of both the steady and unsteady total pressure at multiple streamwise locations were obtained by matching run-to-run tunnel conditions. Three unit Reynolds numbers were tested but only the largest, $\text{Re}' = 9.4 \times 10^6$ m^{-1}, is considered here. Measurements were obtained at three streamwise locations, $\tilde{x}/\tilde{L}_s = 0.86,\ 0.90,$ and 0.94, where $\tilde{x}$ is the

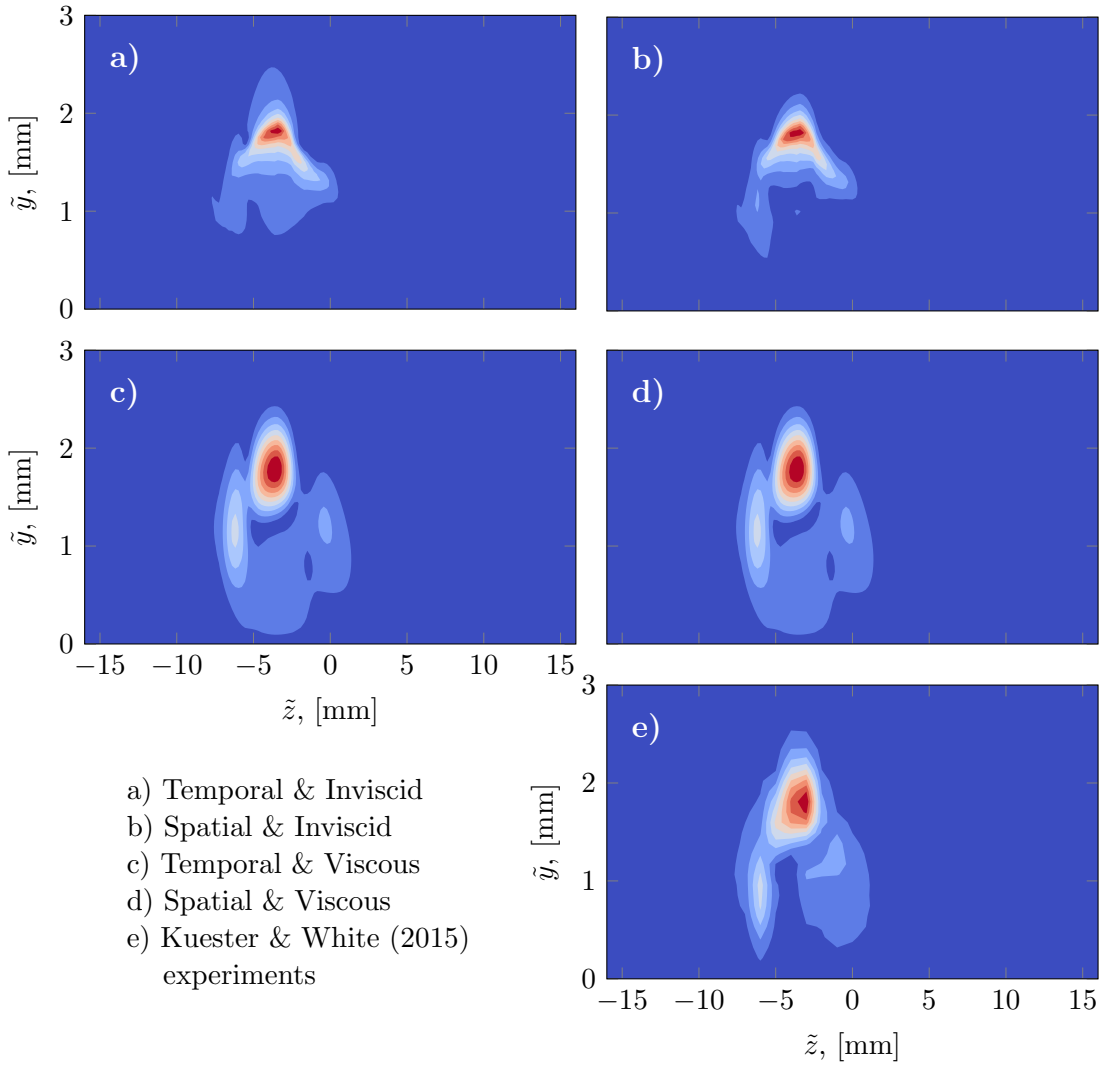

Figure 4.4: Comparison of BiGlobal modes shapes to the discrete roughness experimental data. Top plots are $|\hat{u}|$ for $\tilde{f} = 450$ Hz from stability calculations for all solvers, bottom plot is u'_{rms} digitally band-pass filtered over 430 - 470 Hz and phase-lock averaged in span from the incompressible experiment of Kuester & White [70].

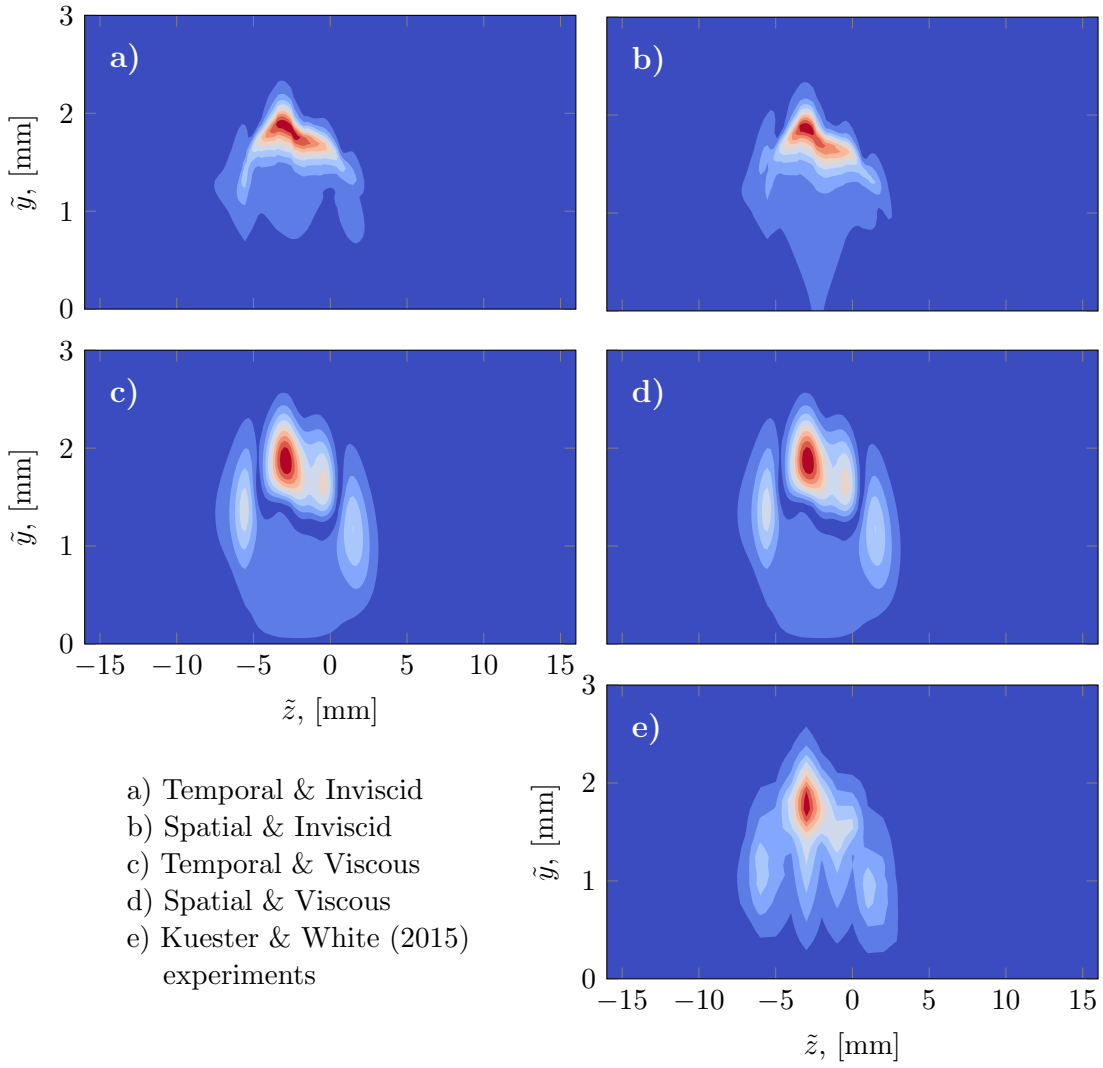

Figure 4.5: Comparison of BiGlobal modes shapes to the combined roughness experimental data. Top plots are $|\hat{u}|$ for $\tilde{f} = 450$ Hz from stability calculations for all solvers, bottom plot is u'_{rms} digitally band-pass filtered over 430 - 470 Hz and phase-lock averaged in span from the incompressible experiment of Kuester & White [70].

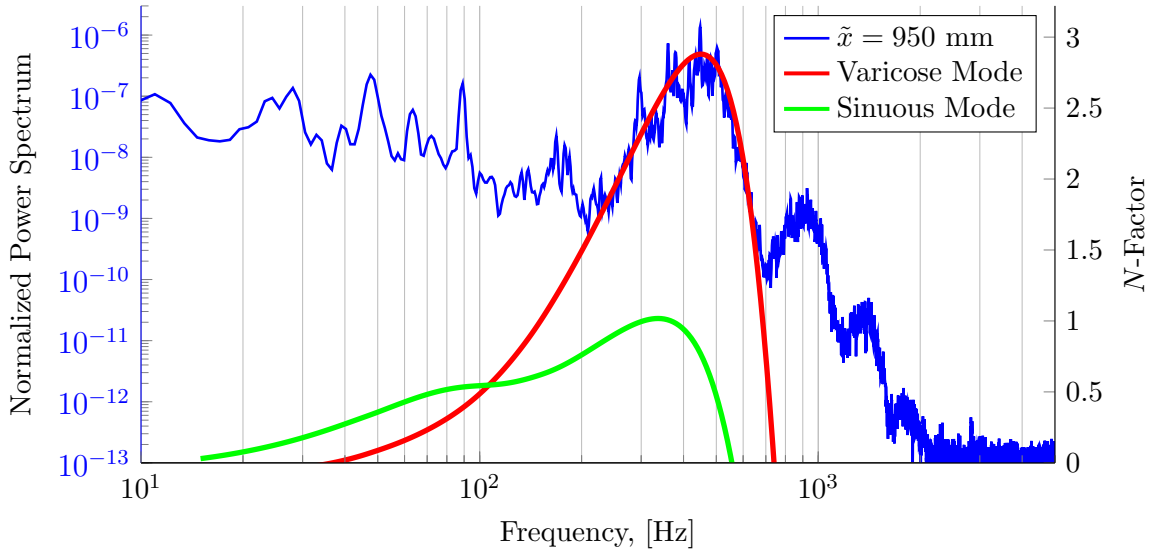

Figure 4.6: Comparison of spatial and viscous BiGlobal N-factors to experimental temporal power spectrum for the discrete roughness case. Blue line is the spectrum at $\tilde{x} = 950$ mm at a point in the wake near the largest u'_{rms} fluctuations. Red and green lines correspond to the spatial N-factors for the varicose- and sinuous-type instabilities, respectively.

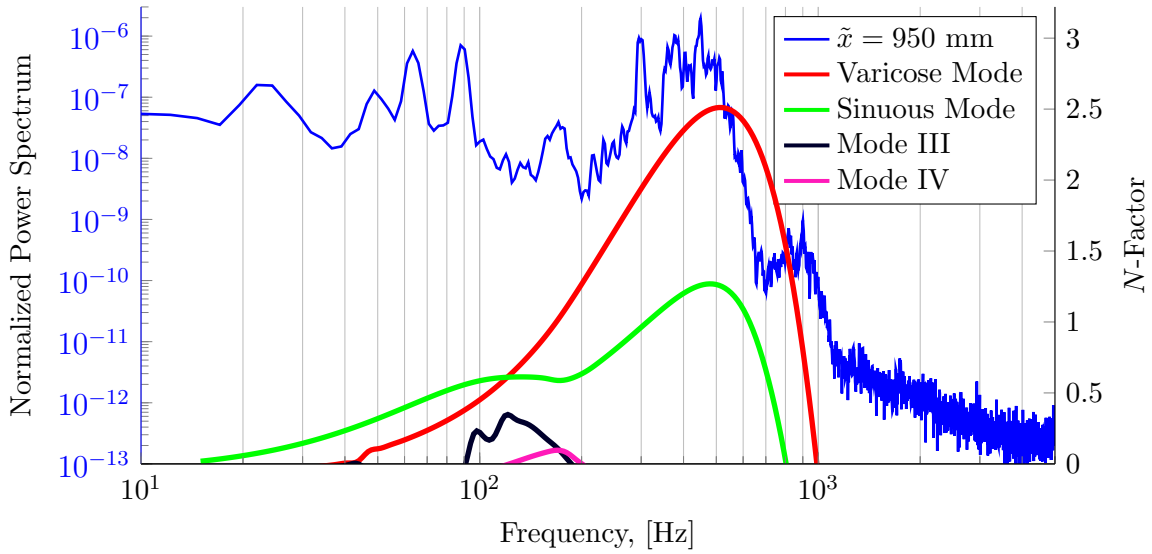

Figure 4.7: Comparison of spatial and viscous BiGlobal N-factors to experimental temporal power spectrum for the combined roughness case. Blue line is the spectrum at $\tilde{x} = 950$ mm at a point in the wake near the largest u'_{rms} fluctuations. Red and green lines correspond to the spatial N-factors for the varicose- and sinuous-type instabilities, respectively. Two additional modes with small positive N-factors were computed.

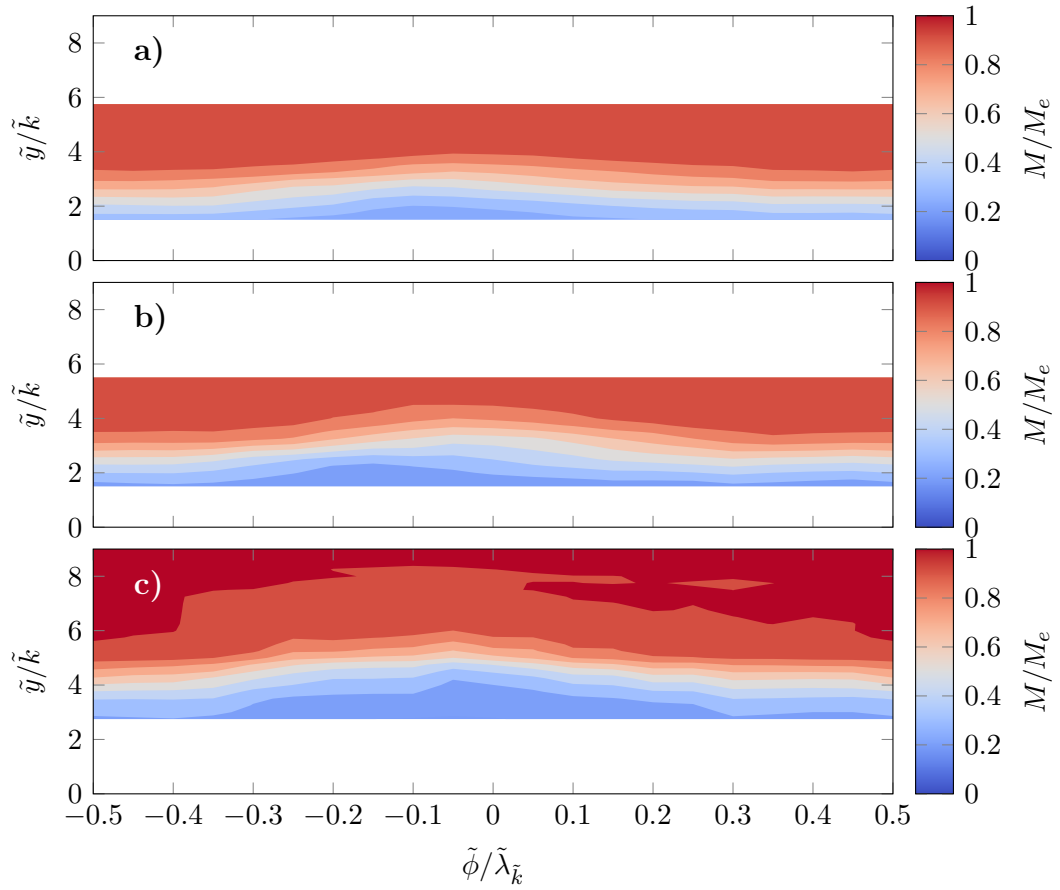

Figure 4.8: Phase-lock averaged Mach number contours at three streamwise locations from the hypersonic experiment of Sharp [73]. **a)** $\tilde{x}/\tilde{L}_s = 0.86$. **b)** $\tilde{x}/\tilde{L}_s = 0.90$. **c)** $\tilde{x}/\tilde{L}_s = 0.94$

.

axial distance from the equivalent sharp tip of the cone and $\tilde{L}_s$ is the axial length of the equivalent sharp cone. Figure 4.8 shows contours of experimentally measured Mach number at each streamwise location. For use in the stability calculations these Mach number contours will be manipulated to extract basic state $\overline{U}$ and $\overline{T}$ values.

Steady high- and low-speed streaks are measured which monotonically grow in the streamwise direction. Between the first and second streamwise locations the total unsteady disturbance energy decreases. However, between the second and the

last streamwise locations the total unsteady disturbance energy shows slight growth. Total steady disturbance energy is defined as:

$$E_{\text{rms}} = \int_0^\infty \gamma p {M'}^2_{\text{rms}} dy,$$

where M'_{rms} is the azimuthal root-mean-square of the steady spanwise Mach number disturbance and the total unsteady disturbance energy is defined as:

$$e_{\text{rms}} = \int_0^\infty \int_0^{\lambda_\phi} p'_{0,\text{rms}} d\phi dy,$$

where $p_{0,\text{rms}}$ is the temporal root-mean-square of the unsteady total pressure [73]. The behavior, which was found in Sharp [73], is shown in Fig. 4.9. The evolution of the steady and unsteady flow is consistent with the mid-wake region observed at low speeds by Ergin & White [8]. Figure 4.10 shows the measured unsteady total pressure fluctuations at $\tilde{x}/\tilde{L}_s = 0.94$ measured by Sharp [73].

Since the primary measurements in the $M_\infty = 6$ experiment by Sharp [73] were obtained using a Pitot tube, only the Mach number is measured and only at a few x locations. The BiGlobal stability methods developed in section 4.2 require both the streamwise velocity, $\overline{U}(y, \phi)$, and the temperature profile, $\overline{T}(y, \phi)$. Since the Mach number is a function of both $\overline{U}(y, \phi)$ and $\overline{T}(y, \phi)$ the problem is ill-posed and more information is needed.

The simple assumption that streamwise vortices merely redistribute parcels of fluid is used to provide closure. It is assumed that streamwise vortices redistribute temperature and streamwise velocity equivalently. Thus the basic-state temperature

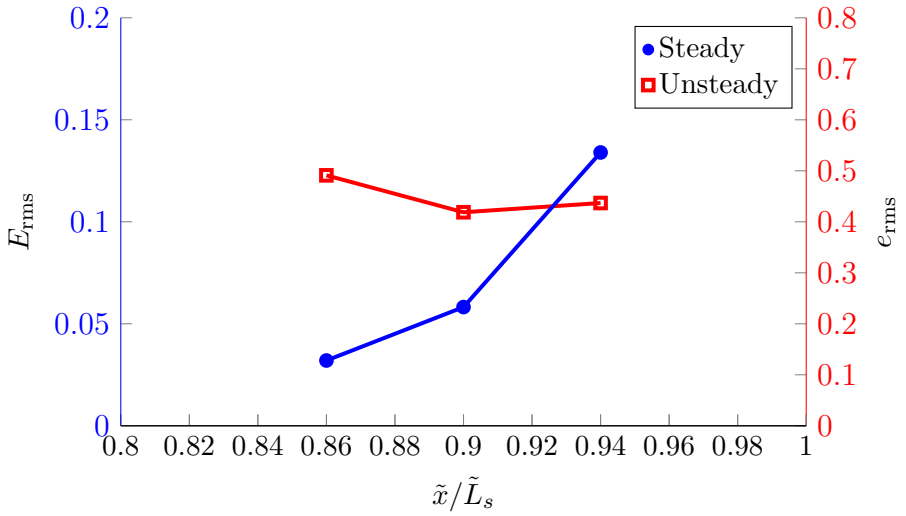

Figure 4.9: Steady and unsteady energy evolution of the total pressure fluctuations measured in the experiment by Sharp [73]. The total steady energy, E_{rms}, grows monotonically in the streamwise direction while the total unsteady energy, e_{rms}, decays then grows.

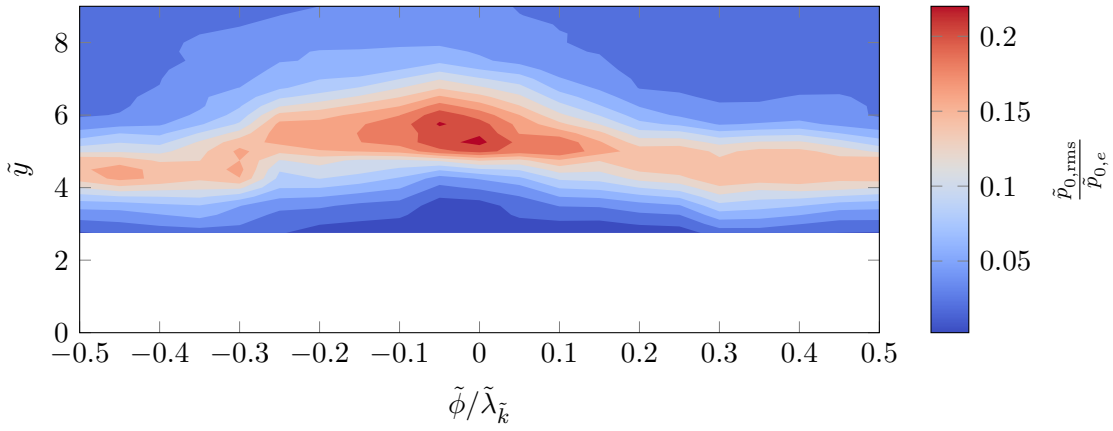

Figure 4.10: Phase-lock averaged unsteady total pressure fluctuations at $\tilde{x}/\tilde{L}_s = 0.94$ measured in the experiment by Sharp [73]. All measurements were above the sonic line.

is assumed to be a function of the basic-state streamwise velocity:

$$\overline{T}(y,\phi) = f(\overline{U}(y,\phi)).$$

The coupling between temperature and streamwise velocity is calibrated using a compressible self-similar solution of the boundary-layer equations under the Mangler–Levy–Lees transformation [55]. This allows the basic state information to be found by solving this nonlinear equation for $\overline{U}(y,\phi)$:

$$\overline{M}(y,\phi) = \frac{\tilde{U}_e \overline{U}(y,\phi)}{\sqrt{\gamma \tilde{\mathcal{R}} \tilde{T}_e f(\overline{U}(y,\phi))}},$$

where $\tilde{\mathcal{R}}$ is the gas constant for air, 287 J kg^{-1} K^{-1}.

Due to numerous difficulties performing hypersonic experiments, the mean and unsteady measurements are not as well resolved as for the low-speed experiment. The two lowest points for the $\tilde{x}/\tilde{L}_s = 0.94$ case and the lowest point for the $\tilde{x}/\tilde{L}_s = 0.90$ case were omitted. The experimental basic state quantities are extrapolated to the wall whose temperature was measured in the experiment. A Fourier transform is taken in the azimuthal direction of the basic state quantities and only the DC component and fundamental wavelength are retained. Symmetry is also enforced since the roughness is symmetric. Figure 4.11 shows both the streamwise velocity and temperature basic states extracted using the procedure above for the data at $\tilde{x}/\tilde{L}_s = 0.86$.

Because of the ambiguity in obtaining the basic state temperature and velocity, only qualitative comparisons can be made between the BiGlobal stability results and the experimental data. All calculations for the hypersonic experiment were obtained using the compressible, viscous, and spatial BiGlobal solver. Figure 4.12 shows the spatial

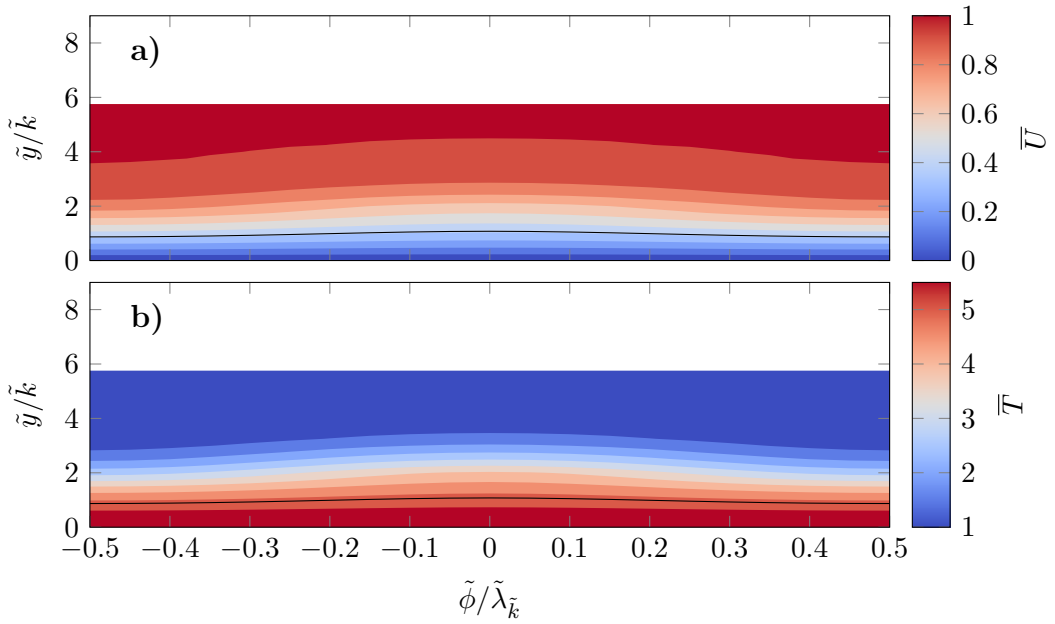

Figure 4.11: Hypersonic basic state at $\tilde{x}/\tilde{L}_s = 0.86$. The sonic line is indicated by the black line. **a)** Contour plot of streamwise velocity basic state. **b)** Temperature basic state contours.

secondary growth rates as a function of frequency for $\tilde{x}/\tilde{L}_s = 0.86$, $\tilde{x}/\tilde{L}_s = 0.90$, and $\tilde{x}/\tilde{L}_s = 0.94$. Weak instabilities, shown in Fig. 4.12, are present at both $\tilde{x}/\tilde{L}_s = 0.86$ and $\tilde{x}/\tilde{L}_s = 0.90$. These results are consistent with the experimentally measured evolution of the unsteady disturbance energy shown in Fig. 4.9.

Mode shapes of $\hat{p}$ and $\hat{T}$ were converted to mode shapes of total pressure using linearized isentropic relations. The calculated total pressure disturbances of the four most unstable modes at $\tilde{x}/\tilde{L}_s = 0.94$ for $\tilde{f}_1 = 30.1$ kHz and $\tilde{f}_2 = 65$ kHz are shown in Figs. 4.13 and 4.14, respectively. The total pressure fluctuations are confined to a narrow band high in the boundary layer similar to the experimental measurements shown in Fig. 4.10. Additionally, a combination of the two dominant instability modes, shown in Figs. 4.13a and 4.14a, are likely present in the unsteady total pressure measurements shown in Fig. 4.10. The results for $\tilde{x}/\tilde{L}_s = 0.94$ suggest that although

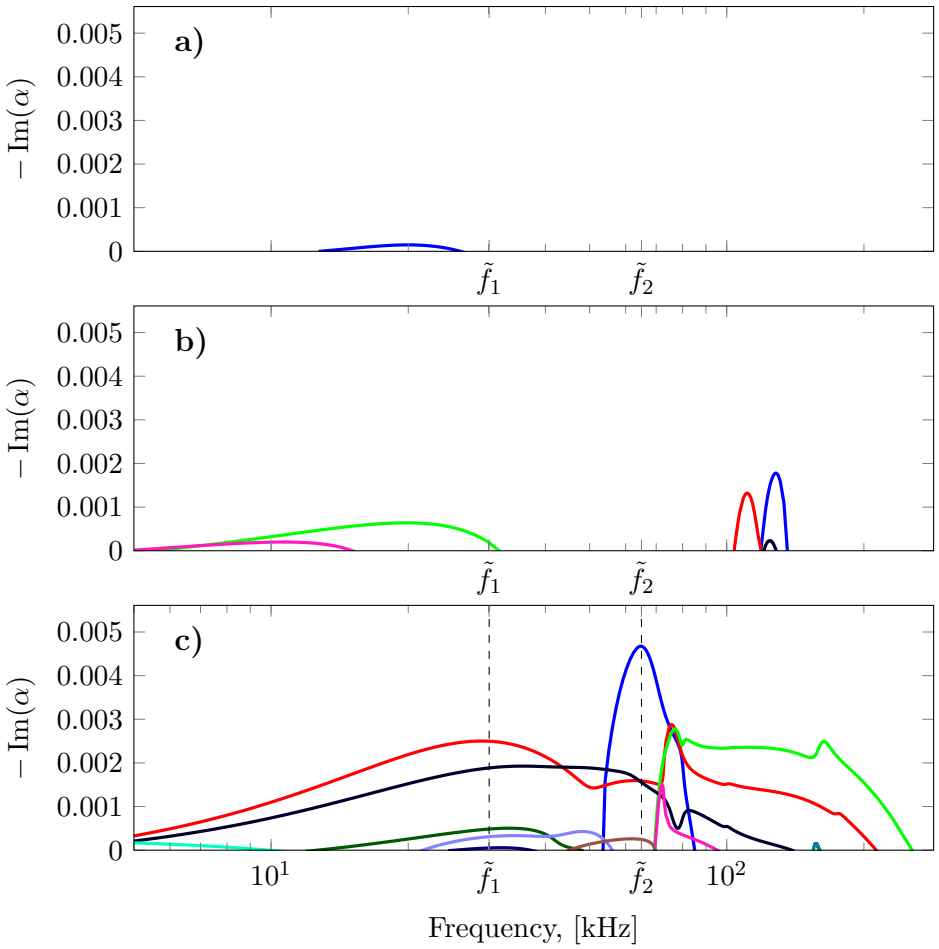

Figure 4.12: Spatial secondary instability growth rates for the hypersonic experiment of Sharp [73]. Matching colors between plots do not necessarily indicate matching modes. **a)** $\tilde{x}/\tilde{L}_s = 0.86$. **b)** $\tilde{x}/\tilde{L}_s = 0.90$. **c)** $\tilde{x}/\tilde{L}_s = 0.94$.

the Sharp [73] experiment did not reveal transition, only a slightly higher Reynolds number or a longer cone might have transitioned.

4.5 Summary & Conclusions

This section described the development of a framework of BiGlobal stability solvers for incompressible/compressible, temporal/spatial, viscous/inviscid secondary instability computations of roughness-induced transient growth. These solvers are

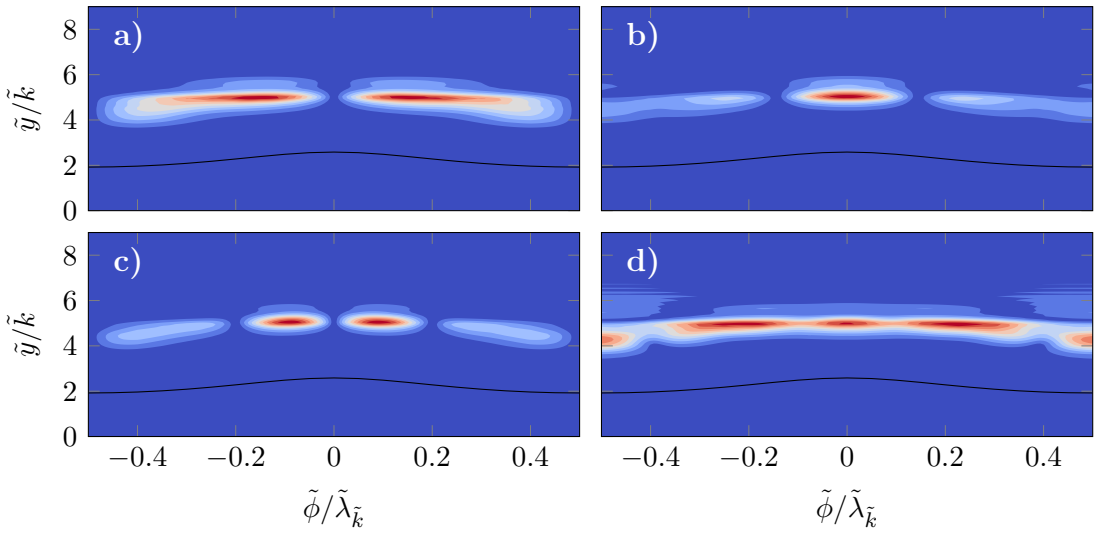

Figure 4.13: Computed total pressure disturbance mode shapes at $\tilde{f} = 30.1$ kHz corresponding to $\tilde{x}/\tilde{L}_s = 0.94$ in the hypersonic experiment by Sharp [73]. The sonic line is indicated by the black line. **a)** $c_r = 0.86$, $\alpha_i = -0.0025$. **b)** $c_r = 0.88$, $\alpha_i = -0.0018$. **c)** $c_r = 0.89$, $\alpha_i = -0.0004$. **d)** $c_r = 0.86$, $\alpha_i = -0.0004$.

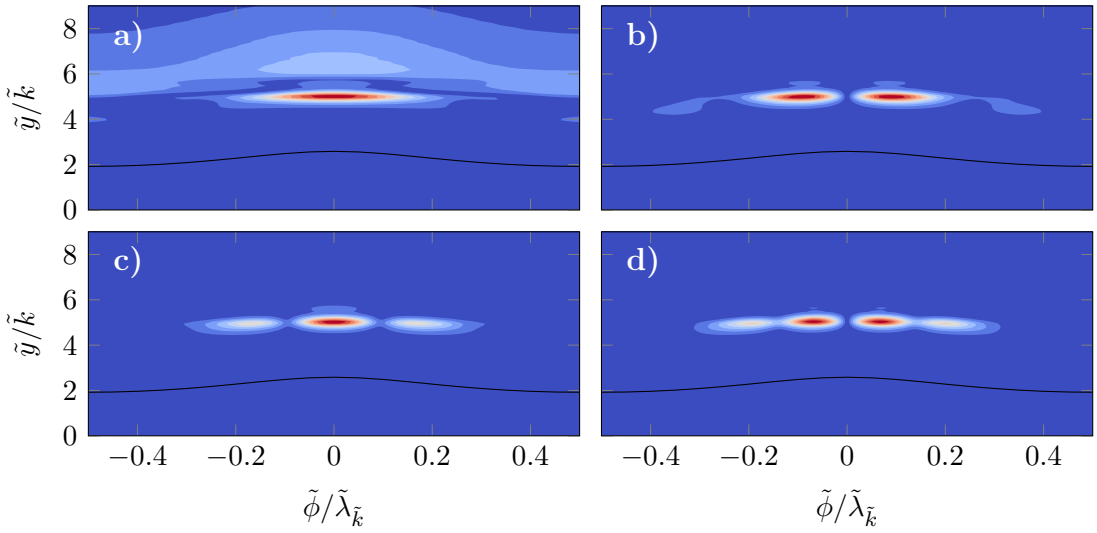

Figure 4.14: Computed total pressure disturbance mode shapes at $\tilde{f} = 65$ kHz corresponding to $\tilde{x}/\tilde{L}_s = 0.94$ in the hypersonic experiment by Sharp [73]. The sonic line is indicated by the black line. **a)** $c_r = 0.89$, $\alpha_i = -0.0044$. **b)** $c_r = 0.89$, $\alpha_i = -0.0017$. **c)** $c_r = 0.89$, $\alpha_i = -0.0015$. **d)** $c_r = 0.91$, $\alpha_i = -0.0002$.

fast and robust, both of which are qualities needed for their use in the main results of Section 5. The solvers were applied to experimental basic states for both low-speed and hypersonic flows.

Kuester & White [70] performed a low-speed experiment to examine the shielding effect of smaller distributed roughness surrounding larger discrete roughness. BiGlobal secondary instabilities were computed for two roughness configurations: discrete roughness only and combined discrete roughness shielded by distributed roughness. The computed growth rates and mode shapes were compared for each BiGlobal solver. The computed growth rates are slightly lower than the measured unsteady disturbance energy growth rate over a similar frequency range, however, the most unstable streamwise velocity mode shape shows excellent agreement with the experimental data. Spatial N-factors were computed for each roughness case and the agreement is excellent when compared to the experimental temporal power spectrum at a point near the largest u'_{rms} fluctuations.

Sharp [73] obtained detailed measurements of the local Mach number behind an azimuthally spaced array of roughness elements. The assumption that transient growth only redistributes parcels of fluid was used to extract the basic state temperature and velocity from the measured Mach numbers. As a result, only qualitative comparisons can be made between the computations and experiment. Nevertheless, the spectrum of secondary instabilities at the three streamwise locations is consistent with the measured total unsteady disturbance energy growth and decay. Additionally, the dominate instability mode shapes agree well with unsteady total pressure measurements at the most downstream location.

Validation of the BiGlobal secondary instability codes against both low- and high-speed experiments provides increased confidence in the continued use of the solvers. The inviscid secondary instability mode shapes are noticeably different from

the otherwise equivalent viscous mode shapes. The inviscid secondary instability growth rates were also approximately 30% higher than the viscous growth rates for the low-speed experiment. Despite these short-comings, the inviscid solvers are almost an order-of-magnitude faster in execution time than the viscous solvers. The effect of temporal or spatial analysis on the secondary instability results is much less significant than the differences between the inviscid and viscous solvers. Very little improvement in execution time is achieved using the temporal/viscous solvers compared to the spatial/viscous solvers. Therefore the spatial/viscous solver will be used exclusively for the optimization in Section 5.

5. SECONDARY INSTABILITY BASED OPTIMAL DISTURBANCES

While optimal disturbances computed by Andersson et al. [17], Tumin & Reshotko [48], and others [16, 46] show some agreement with transition due to freestream turbulence, they show many differences with physically realized roughness-induced transient growth [20, 24]. Denissen & White [20] showed that a periodic array of cylindrical roughness elements within a flat-plate boundary layer excites continuous spectrum modes of the LSEs with larger wall-normal wave numbers. Traditional optimal disturbances, those which maximize the steady disturbance energy growth, excite continuous spectrum modes with smaller wall-normal wave numbers and smaller spatial decay rates compared to those excited by roughness. Denissen & White [24] also show that roughness-induced transient growth is much more unstable to secondary instabilities than traditional optimal disturbances. Therefore optimal disturbances are not the "most-dangerous" disturbances for transition.

5.1 Theory and Motivation

To make optimal disturbances more relevant to surface roughness, using objective functions other than the steady disturbance kinetic energy is required. Objective functions that provide a measure of secondary instability growth rate are particularly interesting. Optimizing over spatial growth rates or N-factors allow the following questions to be answered:

- What is the most destabilizing disturbance that has a maximum spanwise steady disturbance amplitude, $\max_{x,y}(u'_{\mathrm{rms}})$?
- What is the most stabilizing disturbance that has a maximum spanwise steady

disturbance amplitude, $\max_{x,y}(u'_{\mathrm{rms}})$?

The answer to the first question will be more representative of the "most-dangerous" transient disturbance than traditional optimal disturbances. The answer to the second will shed light on potential control possibilities. The solution to both problems is formulated in general terms as:

$$\begin{aligned} \text{maximize} \quad & g(\boldsymbol{Q}_k,\, \alpha_k,\, \hat{\boldsymbol{q}}_k) \\ \text{subject to} \quad & \boldsymbol{f}(\boldsymbol{Q}_k,\, \alpha_k,\, \hat{\boldsymbol{q}}_k) = \boldsymbol{0}. \end{aligned}$$

As an example, the objective and constraint functions for finding the disturbance of fixed disturbance amplitude $\max_{x,y}(u'_{\mathrm{rms}})$ that reaches the largest spatial growth rate is:

$$g(\hat{\boldsymbol{q}}_k,\, \alpha_k,\, \boldsymbol{Q}_k) = -\mathrm{imag}\,(\alpha_{N_x-1})$$

$$\boldsymbol{f}(\hat{\boldsymbol{q}}_k,\, \alpha_k,\, \boldsymbol{Q}_k) = \begin{pmatrix} \boldsymbol{A}_k(\boldsymbol{Q}_k)\hat{\boldsymbol{q}}_k - \alpha_k \boldsymbol{B}_k(\boldsymbol{Q}_k)\hat{\boldsymbol{q}}_k \\ \hat{\boldsymbol{q}}_k^H \hat{\boldsymbol{q}}_k - 1 \\ \boldsymbol{F}_i(\boldsymbol{Q}_0,\, \boldsymbol{Q}_1,\, \ldots,\, \boldsymbol{Q}_i) \end{pmatrix} = \boldsymbol{0}$$

where $\boldsymbol{A}_k(\boldsymbol{Q}_k)\hat{\boldsymbol{q}}_k - \alpha_k \boldsymbol{B}_k(\boldsymbol{Q}_k)\hat{\boldsymbol{q}}_k = \boldsymbol{0}$ is the BiGlobal eigenvalue problem, $\boldsymbol{F}_i(\boldsymbol{Q}_0, \boldsymbol{Q}_1, \ldots, \boldsymbol{Q}_i) = \boldsymbol{0}$ represents propagation of an initial disturbance downstream, $k = 0, 1, \ldots, N_x - 1$, and $i = 1, 2, \ldots, N_x - 1$. Two x indices, i and k, are necessary since $\boldsymbol{Q}_0$ is the vector of free parameters. Multiple constraint functions are necessary due to the complexity of the problem. The first and second constraint equations specify the stability equations for the modified basic state. While the third constraint represents disturbance propagation from the initial to final streamwise location.

In order to accommodate the parabolic Navier–Stokes and BiGlobal secondary instability codes, a robust optimization method must be developed. This is a nonlinear optimization problem with many free parameters. Most nonlinear optimization meth-

ods require the gradient of the objective function with respect to the free parameters to be known. In this case, the free parameters are the initial velocity disturbances. Computing the gradient using finite differences is prohibitively expensive so adjoint optimization is used. There are two types of adjoint optimization: discrete and continuous [75]. Both methods have been used extensively in the literature. Continuous adjoint methods first derive the adjoint equation directly from the continuous governing equations. Discrete adjoint methods derive the adjoint of the discretized governing equations. This research uses discrete adjoint optimization to take advantage of the independently developed PNS and BiGlobal secondary instability codes. The advantage of the discrete approach is straightforward implementation of boundary conditions.

The gradient of a general objective function can be written as: [76]

$$\left.\frac{dg}{d\boldsymbol{p}}\right|_{\boldsymbol{f}=\boldsymbol{0}} = \frac{\partial g}{\partial \boldsymbol{p}} - \boldsymbol{\lambda}^T \frac{\partial \boldsymbol{f}}{\partial \boldsymbol{p}},$$

where the adjoint equation for $\boldsymbol{\lambda}$ is:

$$\left(\frac{\partial \boldsymbol{f}}{\partial \boldsymbol{x}}\right)^T \boldsymbol{\lambda} = \left(\frac{\partial \boldsymbol{g}}{\partial \boldsymbol{x}}\right)^T. \tag{5.1}$$

To put the most-critical disturbance problem in this notation, we note that:

$$\boldsymbol{x} = \left[\hat{\boldsymbol{q}}_k,\ \alpha_k,\ \boldsymbol{Q}_i\right]^T,$$

$$\boldsymbol{p} = \boldsymbol{Q}_0,$$

$$\boldsymbol{\lambda} = \left[\hat{\boldsymbol{\lambda}}_k,\ \beta_k, \boldsymbol{\Lambda}_i\right].$$

Expanding $\frac{\partial \boldsymbol{f}}{\partial \boldsymbol{x}}$ results in a very sparse matrix:

$$\frac{\partial \boldsymbol{f}}{\partial \boldsymbol{x}} = \begin{bmatrix}
(\boldsymbol{A}_0 - \alpha_0 \boldsymbol{B}_0) & 0 & 0 & 0 & -\boldsymbol{B}_0 \hat{\boldsymbol{q}}_0 & 0 & 0 & 0 & 0 & 0 & 0 \\
0 & (\boldsymbol{A}_1 - \alpha_1 \boldsymbol{B}_1) & 0 & 0 & 0 & -\boldsymbol{B}_1 \hat{\boldsymbol{q}}_1 & 0 & 0 & \left[\frac{\partial}{\partial \boldsymbol{Q}_1}(\boldsymbol{A}_1 - \alpha_1 \boldsymbol{B}_1)\right] \hat{\boldsymbol{q}}_1 & 0 & 0 \\
0 & 0 & (\boldsymbol{A}_2 - \alpha_2 \boldsymbol{B}_2) & 0 & 0 & 0 & -\boldsymbol{B}_2 \hat{\boldsymbol{q}}_2 & 0 & 0 & \left[\frac{\partial}{\partial \boldsymbol{Q}_2}(\boldsymbol{A}_2 - \alpha_1 \boldsymbol{B}_2)\right] \hat{\boldsymbol{q}}_2 & 0 \\
0 & 0 & 0 & \ddots & 0 & 0 & 0 & \ddots & 0 & 0 & \ddots \\
2\hat{\boldsymbol{q}}_0^H & 0 & 0 & 0 & 0 & 0 & 0 & 0 & 0 & 0 & 0 \\
0 & 2\hat{\boldsymbol{q}}_1^H & 0 & 0 & 0 & 0 & 0 & 0 & 0 & 0 & 0 \\
0 & 0 & 2\hat{\boldsymbol{q}}_1^H & 0 & 0 & 0 & 0 & 0 & 0 & 0 & 0 \\
0 & 0 & 0 & \ddots & 0 & 0 & 0 & 0 & 0 & 0 & 0 \\
0 & 0 & 0 & 0 & 0 & 0 & 0 & 0 & \frac{\partial \boldsymbol{F}_1}{\partial \boldsymbol{Q}_1} & 0 & 0 \\
0 & 0 & 0 & 0 & 0 & 0 & 0 & 0 & \frac{\partial \boldsymbol{F}_2}{\partial \boldsymbol{Q}_1} & \frac{\partial \boldsymbol{F}_2}{\partial \boldsymbol{Q}_2} & 0 \\
0 & 0 & 0 & 0 & 0 & 0 & 0 & 0 & \vdots & \vdots & \ddots
\end{bmatrix}.$$

When the adjoint equation, Eq. (5.1), is fully expanded, an optimization algorithm becomes apparent:

1. Solve the forward PNS equations:

$$\boldsymbol{F}_i(\boldsymbol{Q}_0,\, \boldsymbol{Q}_1,\, \ldots,\, \boldsymbol{Q}_i) = \boldsymbol{0}$$

$$\frac{\partial \boldsymbol{F}_i}{\partial \boldsymbol{Q}_i}\Delta \boldsymbol{q} = -\boldsymbol{F}_i$$

$$\boldsymbol{Q}_i^{(n+1)} = \boldsymbol{Q}_i^{(n)} + \Delta \boldsymbol{q}$$

2. Compute the BiGlobal stability at each x-location:

$$\boldsymbol{A}_k \hat{\boldsymbol{q}}_k - \alpha_k \boldsymbol{B}_k \hat{\boldsymbol{q}}_k = \boldsymbol{0}$$

3. Compute the objective function $g(\boldsymbol{Q}_k,\, \hat{\boldsymbol{q}}_k,\, \alpha_k)$

4. Compute the left-eigenvectors and normalization of BiGlobal stability problem (the adjoint solution):

$$\left(\boldsymbol{A}_k - \alpha_k \boldsymbol{B}_k\right)^T \hat{\boldsymbol{\lambda}}_k = \left(\frac{\partial g}{\partial \hat{\boldsymbol{q}}_k}\right)^T - 2\beta_k \overline{\hat{\boldsymbol{q}}_k}$$

For solutions to exist, $\beta_k = \frac{1}{2}\hat{\boldsymbol{q}}_k^T \left(\frac{\partial g}{\partial \hat{\boldsymbol{q}}_k}\right)^T$ because $\left(\boldsymbol{A}_k - \alpha_k \boldsymbol{B}_k\right)^T$ is singular. However for all cases considered the objective function does not depend on the BiGlobal modes shapes, $\hat{\boldsymbol{q}}_k$, so the right-hand-side of the above equation is zero. The following eigenvalue problem and normalization equation is then solved:

$$\left(\boldsymbol{A}_k - \alpha_k \boldsymbol{B}_k\right)^T \hat{\boldsymbol{\lambda}}_k = \boldsymbol{0}$$

$$-\hat{\boldsymbol{q}}_k^T \boldsymbol{B}_k^T \hat{\boldsymbol{\lambda}}_k = \frac{\partial g}{\partial \alpha_k}.$$

5. March the adjoint PNS equations upstream in x with inhomogeneous forcing from the adjoint BiGlobal solution:

$$\left(\frac{\partial \boldsymbol{F}_j}{\partial \boldsymbol{Q}_i}\right)^T \boldsymbol{\Lambda}_j = \left(\frac{\partial g}{\partial \boldsymbol{Q}_i}\right)^T - \sum_{j=i+1}^{N_x-1} \left(\frac{\partial \boldsymbol{F}_j}{\partial \boldsymbol{Q}_i}\right)^T \boldsymbol{\Lambda}_j - \left\{\frac{\partial}{\partial \boldsymbol{Q}_i}\left[\left(\boldsymbol{A}_i - \alpha_i \boldsymbol{B}_i\right)\hat{\boldsymbol{q}}_i\right]\right\}^T \hat{\boldsymbol{\lambda}}_i$$

6. Finally, find the gradient using:

$$\frac{dg}{d\boldsymbol{Q}_0} = \frac{\partial g}{\partial \boldsymbol{Q}_0} - \sum_{j=1}^{N_x-1} \boldsymbol{\Lambda}_j^T \frac{\partial \boldsymbol{F}_j}{\partial \boldsymbol{Q}_0} - \hat{\boldsymbol{\lambda}}_0^T \left\{\frac{\partial}{\partial \boldsymbol{Q}_0}\left[\left(\boldsymbol{A}_0 - \alpha_0 \boldsymbol{B}_0\right)\hat{\boldsymbol{q}}_0\right]\right\}$$

In some cases, the gradient must be smoothed in order to ensure independence from discretization. The smoothing method is the same as that advocated by Siva & Jameson [75]. The smoothed gradient is found as a solution to the following diffusion equation:

$$\left(\boldsymbol{I} - \epsilon \nabla^2\right) \overline{\frac{dg}{d\boldsymbol{Q}_0}} = \Re\left(\frac{dg}{d\boldsymbol{Q}_0}\right),$$

where $\overline{\frac{dg}{d\boldsymbol{Q}_0}}$ is the smoothed gradient, ϵ is a smoothing parameter, and $\Re$ projects the gradient onto the real axis.

The smoothing mechanism in the above equation can be demonstrated by assuming that the gradients are simple one-dimensional sinusoids, $\overline{\frac{dg}{d\boldsymbol{Q}_0}} = \overline{G} e^{ikx}$ and $\frac{dg}{d\boldsymbol{Q}_0} = G e^{ikx}$. Substituting these expressions into the smoothing equation shows $\overline{G} = (1 + \epsilon k^2)^{-1} G$. Thus, short wavelength fluctuations are highly damped. This smoothing method is only used for the traditional optimal disturbance objective function. The cases that include secondary instabilities in the optimization do not require smoothing.

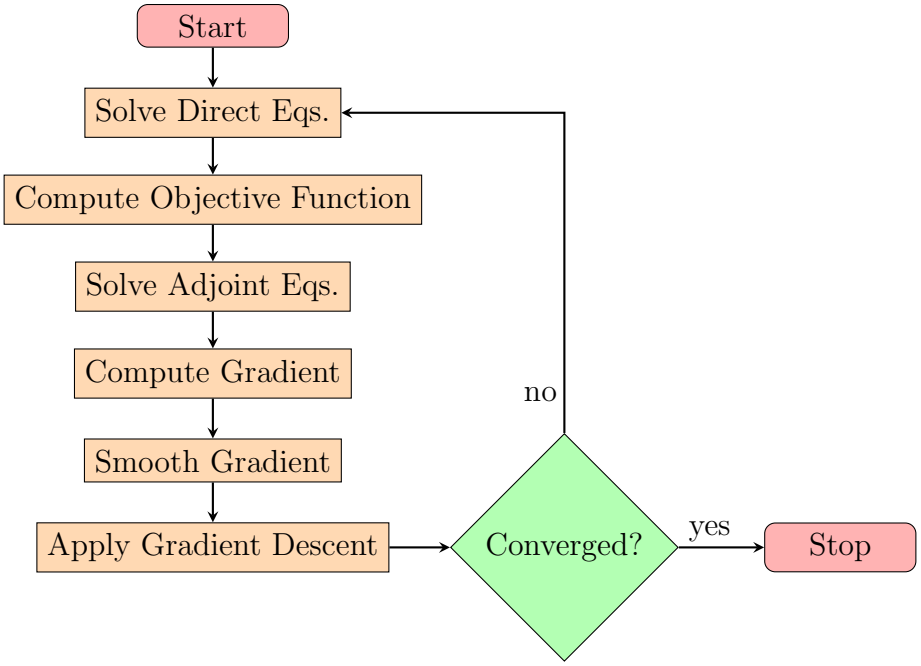

Figure 5.1: Flow chart showing the adjoint optimization process. The direct equations refers to both the PNS and BiGlobal solvers and gradient smoothing is only used as necessary.

This research makes use of the gradient-descent algorithm. At each iteration, the adjoint method given above is used to compute the gradient of the objective function with respect to the initial state vector. The initial state vector is then updated as:

$$\boldsymbol{Q}_0^{(n+1)} = \boldsymbol{Q}_0^{(n)} + \gamma \overline{\frac{dg}{d\boldsymbol{Q}_0}},$$

where γ is a parameter that controls the convergence rate. The γ parameter is positive for maximization problems and negative for minimization problems. If γ is too large, the convergence may suffer due to overshoot. At every iteration the disturbance kinetic energy of the initial state is set equal to that of the previous iteration:

$$\boldsymbol{Q}_0^{(n+1)} = \frac{\mathcal{E}(\boldsymbol{Q}_0^{(n)})}{\mathcal{E}(\boldsymbol{Q}_0^{(n+1)})} \boldsymbol{Q}_0^{(n+1)}. \tag{5.2}$$

This optimization algorithm is summarized in Fig. 5.1.

Enforcement of the $\max_{x,y}(u'_{\text{rms}})$ parameter is carried out using a predictor-corrector step of the propagation equations. The initial state from Eq. (5.2) is propagated by solving the PNS equations. The corrector step is obtained by linearly rescaling the predictor step to achieve the desired $\max_{x,y}(u'_{\text{rms}})$:

$$\boldsymbol{Q}_0^{(n+1)}|_{\text{corr.}} = \frac{\max_{x,y}(u'_{\text{rms}})}{\mathcal{R}(\boldsymbol{Q}_i^{(n+1)})}\boldsymbol{Q}_0^{(n+1)}|_{\text{pred.}},$$

where $\mathcal{R}(\boldsymbol{Q}_i^{(n+1)})$ is an operator that computes the maximum spanwise u'_{rms} over the entire streamwise and wall-normal domain. The corrector initial condition, $\boldsymbol{Q}_0^{(n+1)}|_{\text{corr.}}$, is then used for the remainder of the iteration.

The optimization method outlined above allows the evaluation of several different objective functions. Each of these cases reveal crucial details of the growth and breakdown of transient disturbances. The three main cases that will be considered are: traditional optimal disturbances, most-stabilizing disturbances, and most-destabilizing disturbances.

Ensuring converged solutions is important any time an iterative method is used. The optimization method used here consists of multiple separate codes that each must converge. First, the PNS code iterates until the Newton iterations have converged. The criteria used to assess this convergence was discussed in Section 3.2. In addition to the Newton iterations, convergence of the PNS code as a whole is assessed by comparing results from fine, medium, and coarse discretizations in the x, y, and z directions. The same comparison of discretizations is used to assess the convergence of the BiGlobal secondary instability code.

The gradient descent algorithm must also converge. Convergence is achieved when:

$$\frac{\mathcal{E}(\boldsymbol{Q}_0^{(n+1)} - \boldsymbol{Q}_0^{(n)})}{\mathcal{E}(\boldsymbol{Q}_0^{(n)})} < 10^{-5}. \tag{5.3}$$

A large portion of the following results consist of streamwise vortices. It is desirable to monitor the changes in location and strength of these streamwise vortices as parameters are varied. The λ_2 vortex identification method developed by Jeong & Hussain [77] will be used here. This method consists of computing the eigenvalues of the following tensor at every location in the flow:

$$\boldsymbol{T} = \boldsymbol{S}^2 + \boldsymbol{Q}^2, \tag{5.4}$$

where $\boldsymbol{S}$ and $\boldsymbol{Q}$ are the symmetric and antisymmetric portions of the velocity gradient:

$$\boldsymbol{S} = \frac{1}{2}\left[\nabla \boldsymbol{u} + (\nabla \boldsymbol{u})^T\right],$$

$$\boldsymbol{Q} = \frac{1}{2}\left[\nabla \boldsymbol{u} - (\nabla \boldsymbol{u})^T\right].$$

If $\boldsymbol{\lambda} = [\lambda_1,\ \lambda_2,\ \lambda_3]^T$ is a vector containing the eigenvalues of $\boldsymbol{T}$ where $\lambda_1 > \lambda_2 > \lambda_3$, then λ_2 is the quantity of interest. Locations with $\lambda_2 < 0$ are within a vortex core, with the center of the core at the local λ_2 minimum.

The previous work by Andersson et al. [17], Tumin & Reshotko [48], and others will be referred to in this section as traditional optimal disturbances. The objective function for traditional optimal disturbances is the steady disturbance kinetic energy at the optimization location divided by the initial upstream disturbance kinetic energy. Using the present optimization method to compute these traditional disturbances is used to validate the optimization scheme before incorporating secondary instabilities.

Figure 5.2 is a plot of the traditional optimal disturbance energy growth normalized by the change in Reynolds number between the upstream and optimization locations for several spanwise wavenumbers and disturbance amplitudes. Results using the PNS solver are compared to those from Andersson et al. [17] and Tumin & Reshotko [48]. The results from both of those works are for $\mathrm{Re}_{x_f} - \mathrm{Re}_{x_0} = 10^6$. Andersson et al. [17] used the leading edge as the initial upstream location, or $\mathrm{Re}_{x_0} = 0$. Tumin & Reshotko [48] employed the parallel flow assumption. The results of the present work were obtained using $\mathrm{Re}_{x_0} = 0.25 \times 10^6$ and $\mathrm{Re}_{x_f} = 1.25 \times 10^6$.

Traditional optimal growth factors computed here are of similar magnitude and are largest for similar spanwise wavenumbers. The results of the present method follow those of Andersson et al. [17] better than those of Ref. [48]. The difference is attributed to nonparallel effects. The difference in amplitude between the present results and Ref. [17] is due to differences in Re_{x_0}. Figure 5.3 shows the structure of counter-rotating streamwise vortices located high in the boundary layer that is typical of traditional optimal disturbances. The magnitude and direction of the arrows is computed using the initial spanwise and wall-normal velocity disturbances. At this initial location the streamwise velocity disturbance is zero. Similarly to Zuccher et al. [46], the optimization method used here allows nonlinear traditional optimal disturbances to be computed. Figure 5.4 shows the effects of increasing $\max_{x,y}(u'_{\mathrm{rms}})$ on the optimal disturbance kinetic energy growth. As $\max_{x,y}(u'_{\mathrm{rms}})$ increases, the optimal growth factor decreases.

5.1.1 Most-Unstable Disturbances

As mentioned several times now, the main goal of this research is to compute the initial disturbances that maximize secondary instability growth rates. The most-destabilizing disturbances are computed by maximizing the spatial growth

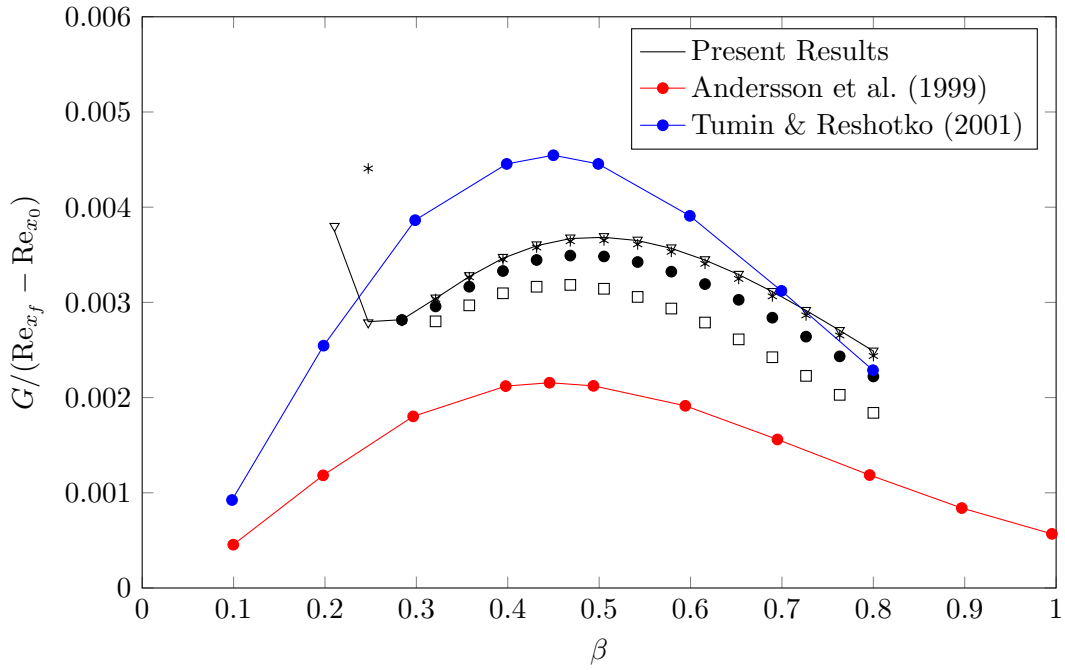

Figure 5.2: Optimal disturbance energy growth normalized by Reynolds number for several spanwise wavenumbers. Results using the present optimization method are compared to the results of Andersson et al. [17] and Tumin & Reshotko [48]. The present optimization method was used for multiple disturbance amplitudes, $\max_{x,y}(u'_{\mathrm{rms}})$: 0.001 (——), 0.01 (▽), 0.05 (∗), 0.10 (•), 0.15 (□). Results for $\beta < 0.2$ did not converge.

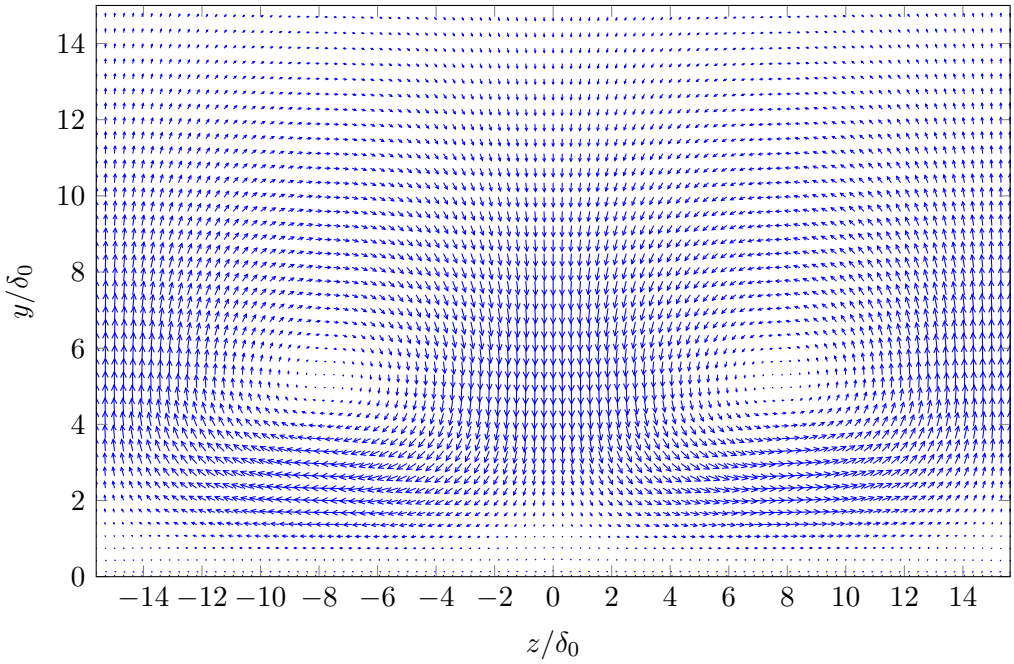

Figure 5.3: Similar to the results of Andersson et al. [17] and Tumin & Reshotko [48], the traditional optimal disturbance is counter-rotating streamwise vortices high in the boundary layer.

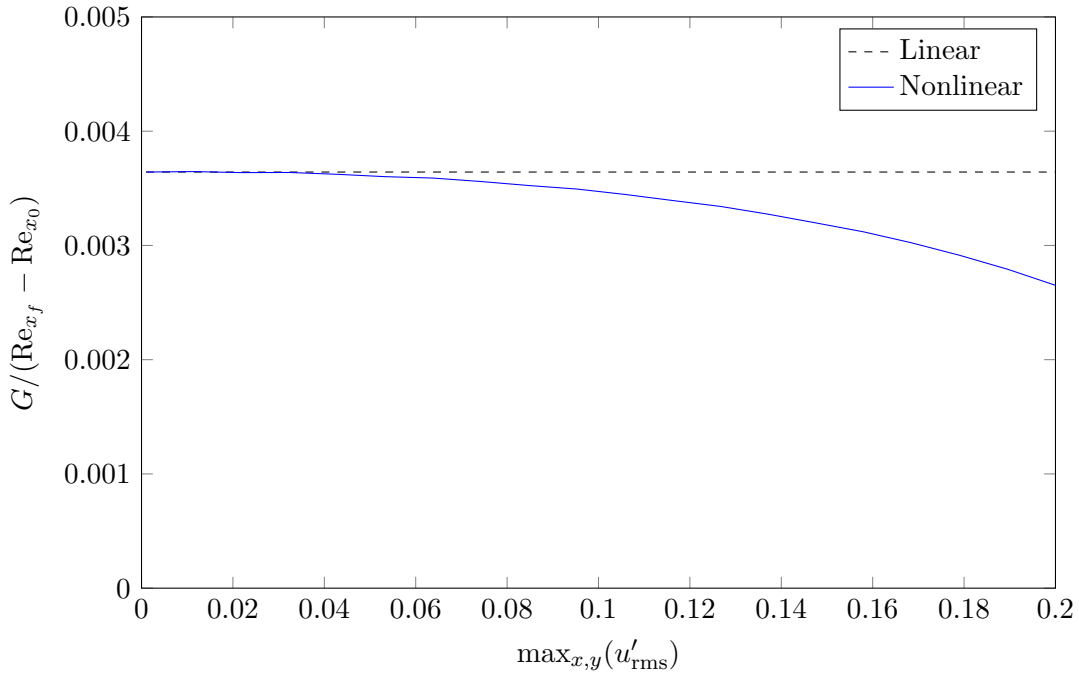

Figure 5.4: Comparison of linear and nonlinear optimal transient growth using the disturbance energy objective function.

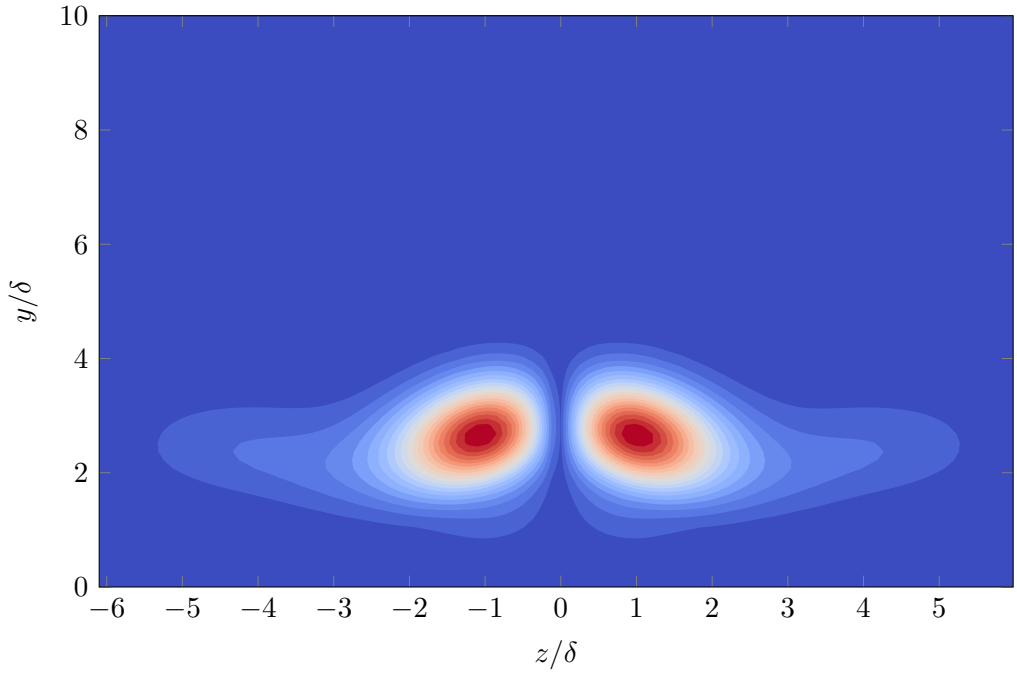

Figure 5.5: This is an example sinuous mode shape that is the result of the initial disturbance which maximizes the sinuous instability growth rate at $\mathrm{Re}_{x_f} = 0.32 \times 10^6$. Colors are contours of $|\hat{u}|$.

rate of the sinuous secondary instability. The sinuous instability has been shown to have a primary role in roughness-induced transition [24] and is the main instability investigated here. Figure 5.5 is an example sinuous mode shape that is the result of an initial disturbance that maximizes the sinuous mode growth rate at $\mathrm{Re}_{x_f} = 0.32 \times 10^6$. Figure 5.6 shows a vector plot of the initial disturbance that produces the sinuous instability in Figure 5.5. The most-destabilizing initial disturbance is counter-rotating streamwise vortices located much lower in the boundary layer than traditional optimal disturbances (Fig. 5.3). Additionally, the vortices are clustered more closely together as opposed to the even spanwise spacing of traditional optimal disturbances. Both of these characteristic have been observed in roughness experiments [18, 19, 8].

By performing the optimization for the most-destabilizing disturbance at multiple

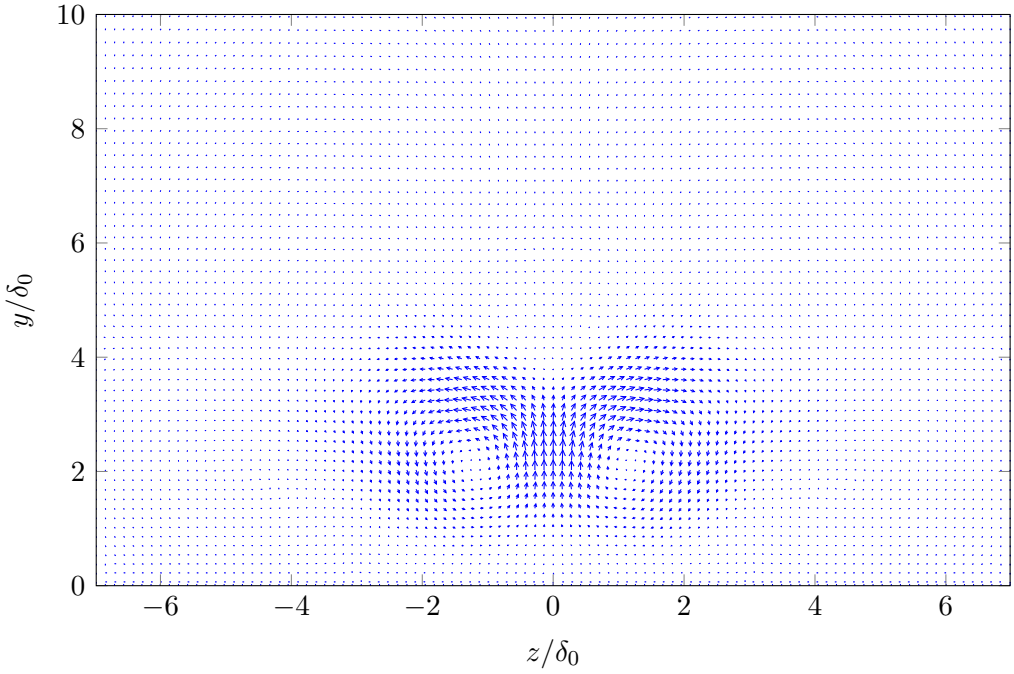

Figure 5.6: This is a plot of a characteristic initial disturbance at $\mathrm{Re}_{x_0} = 0.25 \times 10^6$ which maximizes the secondary instability growth rate at $\mathrm{Re}_{x_f} = 0.32 \times 10^6$. Compared to the traditional optimal disturbance, the streamwise vortices are closer together which increases gradients to which the sinuous instability is sensitive.

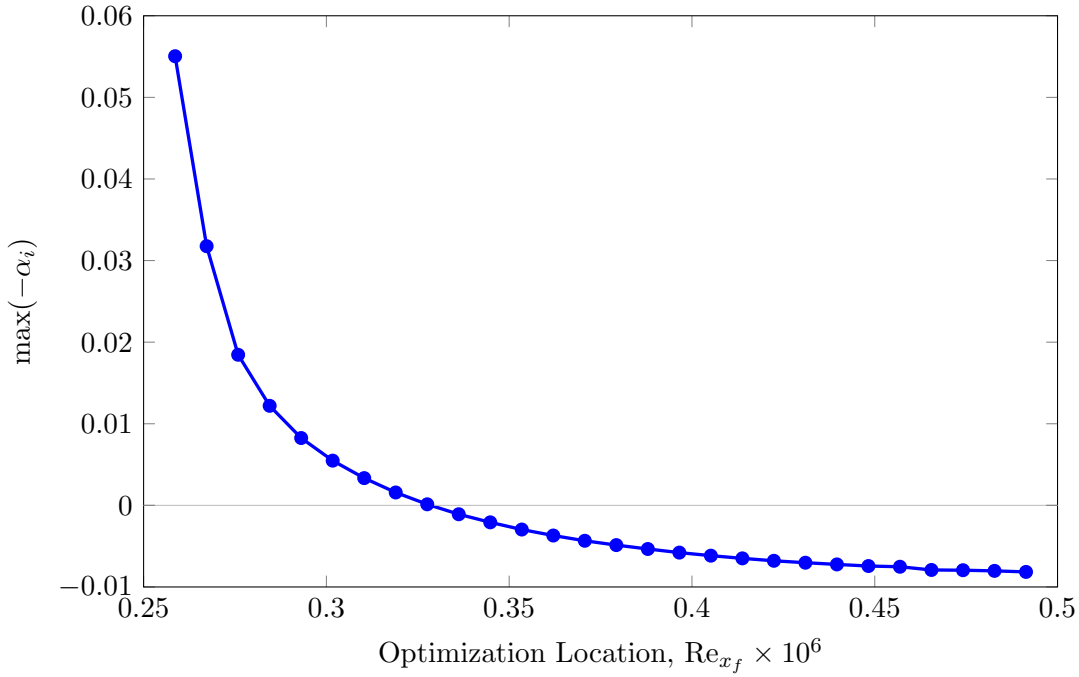

Figure 5.7: Envelope of the most unstable spatial growth rates for disturbances with a maximum $\max_{x,y}(u'_{\mathrm{rms}}) = 0.08$ versus Reynolds number based on the streamwise coordinate. Disturbances were computed using $\mathrm{Re}_{x_0} = 0.25 \times 10^6$, $F = 300 \times 10^{-6}$, and $\beta_0 = 0.45$.

locations, an envelope of the maximum spatial growth rate is obtained for steady transient disturbances with a maximum amplitude of $\max_{x,y}(u'_{\mathrm{rms}}) = 0.08$. This envelope is shown in Fig. 5.7. The corresponding maximum spatial N-factors are shown in Fig. 5.8. Both of these plots show that if transition does occur, it will be initiated in the immediate vicinity of the roughness. This effect was also observed by Denissen & White [24].

A key question in the literature [21, 46] is: "What is the minimum disturbance amplitude that can destabilize secondary instabilities?" Using traditional optimal disturbance theory the minimum amplitude for sinuous instability is $A = 0.26$ or

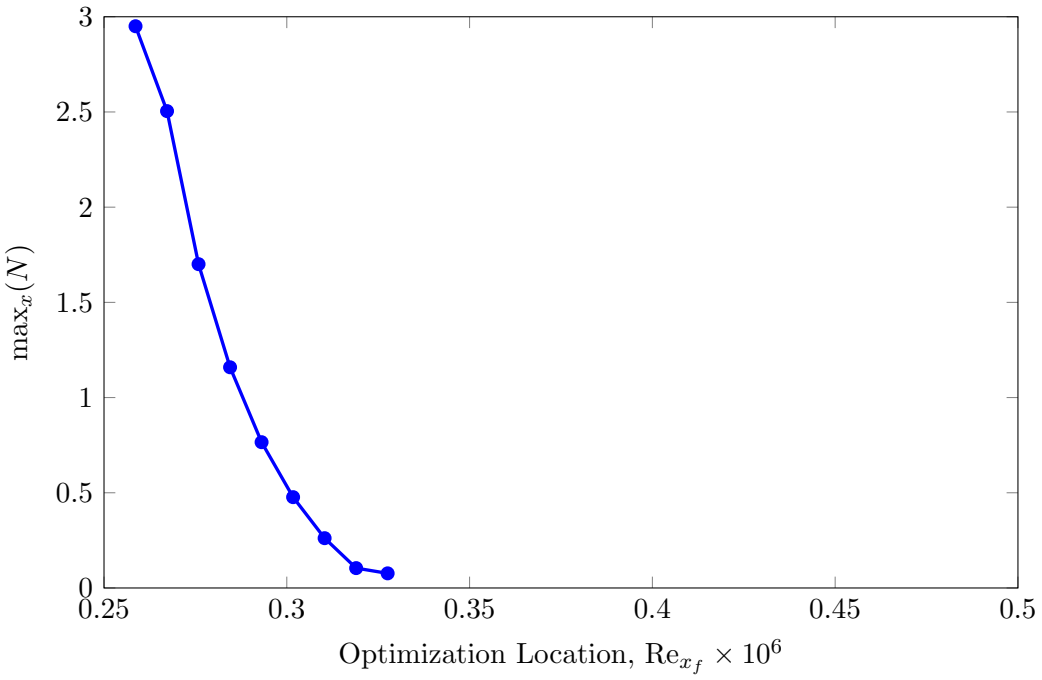

Figure 5.8: Maximum spatial N-factor over the entire domain as a function of the location of secondary instability optimization for $\max_{x,y}(u'_{\mathrm{rms}}) = 0.08$, $\mathrm{Re}_{x_0} = 0.25 \times 10^6$, $F = 300 \times 10^{-6}$, and $\beta_0 = 0.45$.

$\max_{x,y}(u'_{\text{rms}}) = 18\%$ [21]. The amplitude A is defined as:

$$A = \frac{1}{2}\left[\max_{y,z}(U - U_B) - \min_{y,z}(U - U_B)\right],$$

where U is the streamwise velocity basic state and U_B is the streamwise velocity of the Blasius solution. The optimization method developed here makes addressing this question easier. Figure 5.9 is a plot of $\max(-\alpha_i)$ versus disturbance spanwise root-mean-square amplitude for several optimization locations. This shows that a sinuous instability can occur for disturbances amplitudes as low as $\max_{x,y}(u'_{\text{rms}}) = 2.5\%$. This is consistent with roughness experiments that see subcritical transition with steady disturbance amplitudes only slightly higher than this value [8] and much lower than those reported by Andersson et al. [21].

Figure 5.10 is a plot of $\max(-\alpha_i)$ as a function of nondimensional frequency for several disturbance amplitudes. The envelope of sinuous mode growth rates reaches a local maximum between $F = 150 \times 10^{-6}$ and $F = 300 \times 10^{-6}$. Sinuous modes are able to achieve higher growth rates as F increases though. Convergence was not achieved beyond $F = 700 \times 10^{-6}$. Ergin & White [8] observed a band of amplified frequencies from 300 to 800 Hz, or approximately $F = 200 \times 10^{-6}$ to 600×10^{-6} which is consistent with the results in Fig. 5.10.

5.1.2 Tollmien–Schlichting Wave Stabilization

Previous researchers [22, 23, 78, 79] have shown that streamwise streaks in a boundary-layer can be stabilizing for TS waves. This optimization computes the disturbance that is most effective at TS wave stabilization. For both the most-stabilizing and the most-destabilizing disturbances, the objective function is $g = -\text{imag}(\alpha_{x_f})$ or the spatial growth rate at the optimization location. The computation of the objective function gradient is the same. A change in sign on the gradient descent

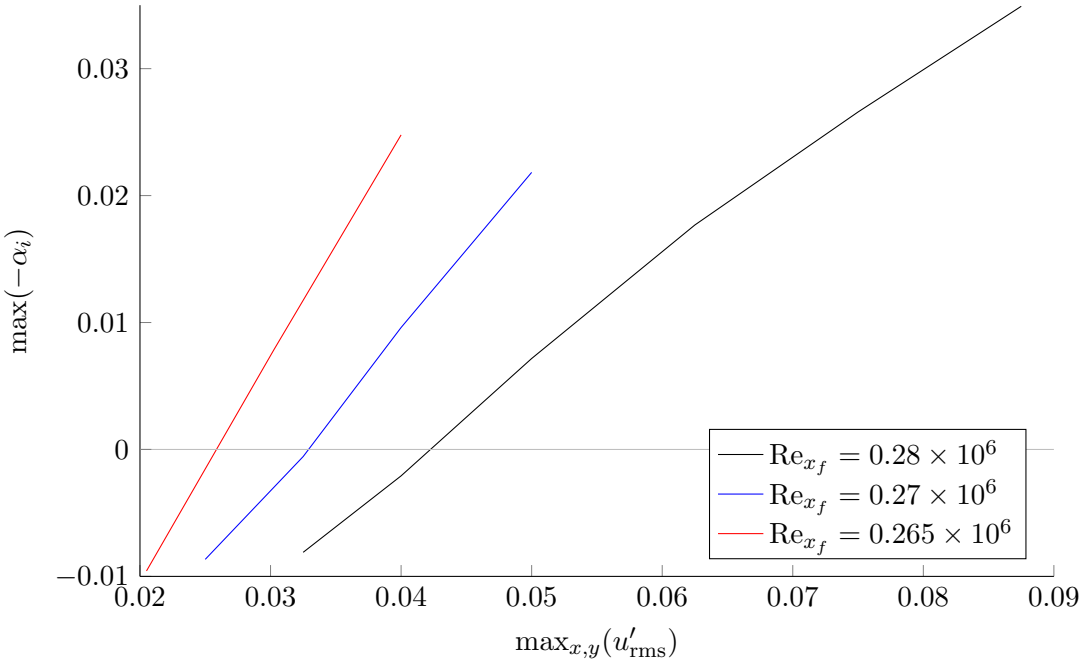

Figure 5.9: Maximum spatial sinuous mode growth rate as a function of the maximum transient growth steady amplitude, $\max_{x,y}(u'_{\mathrm{rms}})$, for three optimization locations: $\mathrm{Re}_{x_f} = 0.265 \times 10^6$, 0.27×10^6, and 0.28×10^6. For all cases shown in this plot, $\mathrm{Re}_{x_0} = 0.25 \times 10^6$, $\beta_0 = 0.45$, and $F = 300 \times 10^{-6}$.

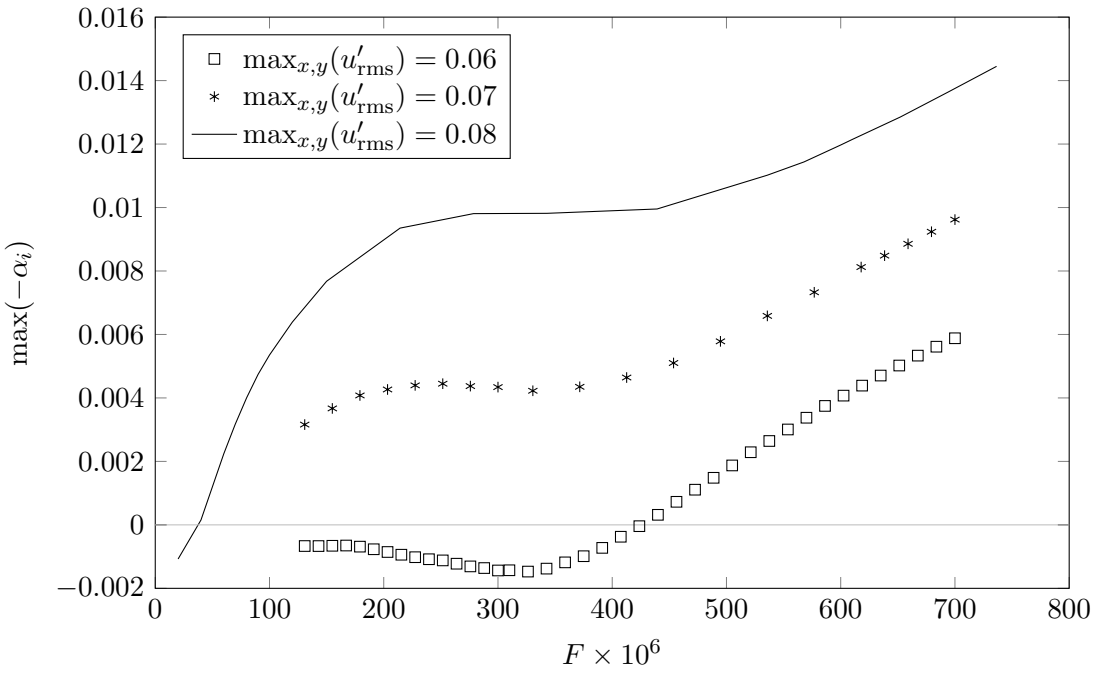

Figure 5.10: Maximum spatial sinuous mode growth rate as a function of nondimensional frequency for $\max_{x,y}(u'_{\text{rms}}) = 0.06$, 0.07, and 0.08, $\text{Re}_{x_0} = 0.25 \times 10^6$, $\text{Re}_{x_f} = 0.30 \times 10^6$, and $\beta_0 = 0.45$.

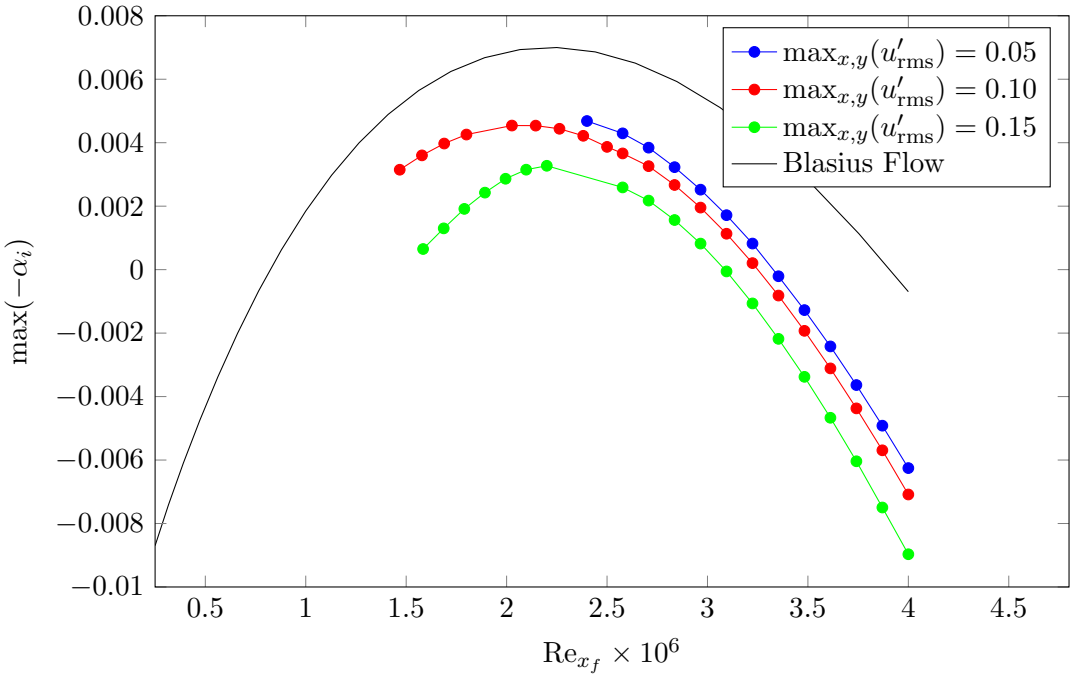

Figure 5.11: Minimization of spatial TS wave instability growth rate for several spanwise streak amplitudes, $\max_{x,y}(u'_{\text{rms}})$, as Re_{x_f} is varied compared to the TS growth rate for Blasius flow.

factor changes whether a maximization or minimization problem is being solved. The most-stabilizing disturbances are computed to minimize the spatial growth rate of TS waves and so the sign of the gradient descent factor is chosen accordingly.

Figure 5.11 is a plot of TS wave growth rate as a function of optimization location for several disturbance amplitudes. The optimization results are compared to the baseline Blasius boundary layer TS wave. The TS wave is stabilized for all optimization locations computed. The minimized TS wave growth rate as a function of nondimensional frequency is shown in Fig. 5.12. Comparison is again made to the Blasius TS wave growth rate. Based on these results, streamwise streaks are better at stabilizing TS waves at higher frequencies. Figure 5.13 is a plot of the minimized TS wave growth rate as a function of spanwise wavenumber. For $\text{Re}_{x_0} = 0.25 \times 10^6$,

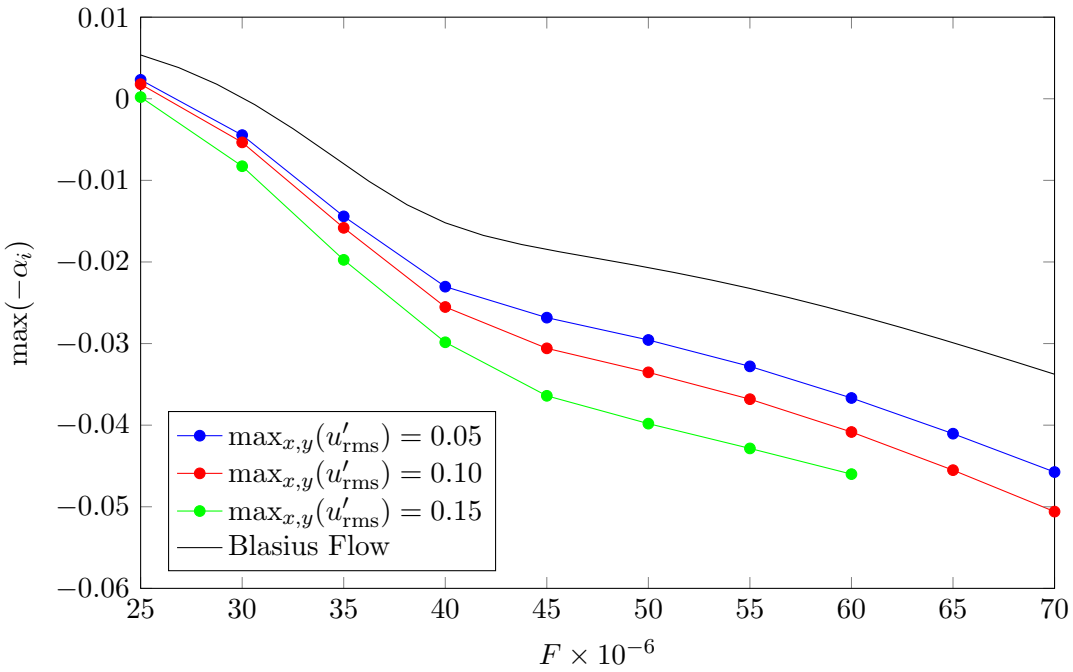

Figure 5.12: Minimization of spatial TS wave instability growth rate for several spanwise streak amplitudes, $\max_{x,y}(u'_{\text{rms}})$, for various nondimensional frequencies, F, compared to the TS growth rate for Blasius flow.

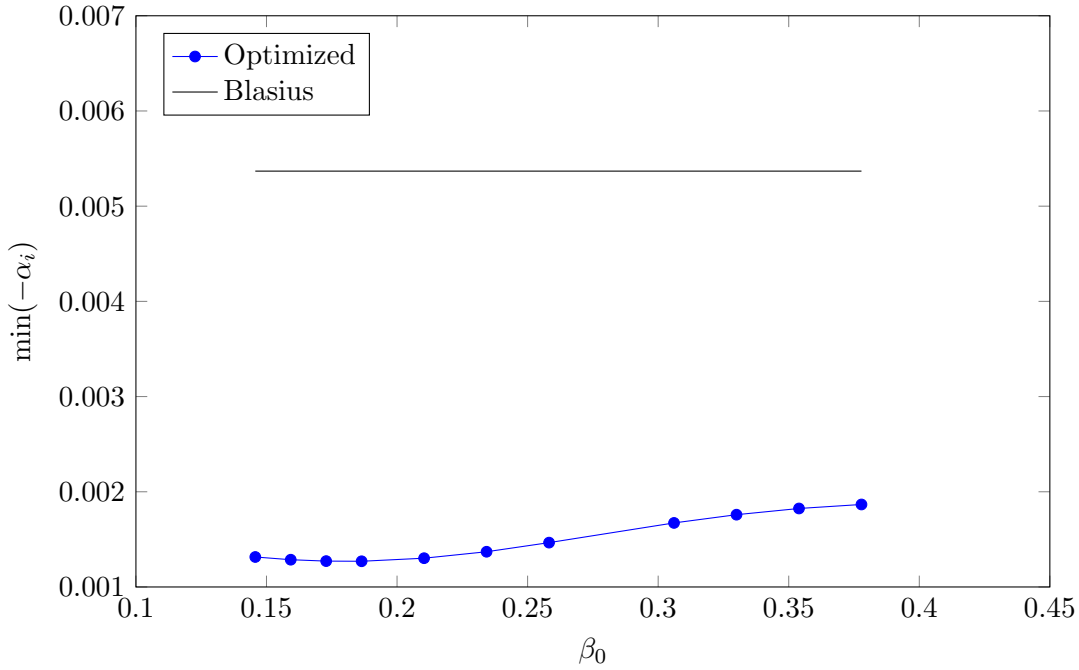

Figure 5.13: Minimization of spatial TS wave instability growth rate for varying spanwise wavenumber, β_0, compared to the TS growth rate for Blasius flow. $\mathrm{Re}_{x_0} = 0.25 \times 10^6$, $\mathrm{Re}_{x_f} = 0.30 \times 10^6$, $F = 25 \times 10^{-6}$, and $\max_{x,y}(u'_{\mathrm{rms}}) = 0.05$.

$\mathrm{Re}_{x_f} = 0.30 \times 10^6$, $F = 25 \times 10^{-6}$, and $\max_{x,y}(u'_{\mathrm{rms}}) = 0.05$, the best spanwise wavenumber for TS wave stabilization is $\beta_0 = 0.18$.

The initial disturbance that is best at stabilizing TS waves is similar to traditional optimal disturbances except located slightly lower in the boundary layer. An example of the streamwise vortex structure is shown in Fig. 5.14. An example of a spanwise modulated TS wave streamwise velocity mode shape is shown in Fig. 5.15.

There are a few caveats to using these disturbances to attempt to delay transition. First, if the transient growth induced streaks grow too large sinuous instabilities may appear. Second, while the TS wave growth rate is reduced by these disturbances, the resulting spanwise modulated TS wave may be unstable to secondary instabilities at a lower amplitude due to increased three dimensionality.

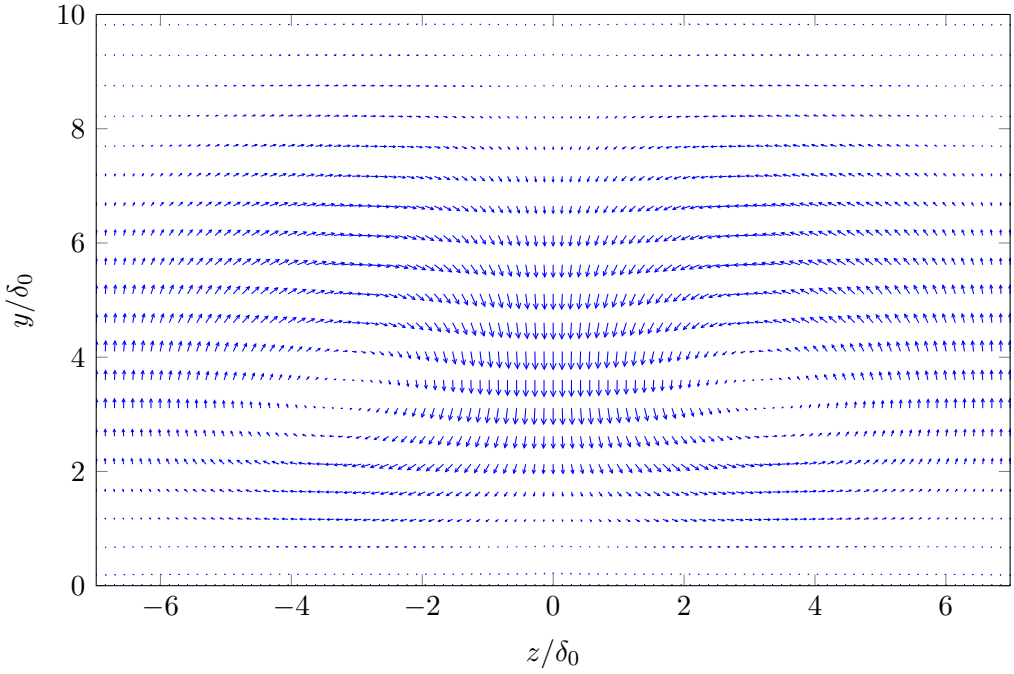

Figure 5.14: This is a plot of a characteristic initial disturbance which minimizes the TS wave growth rate at $\mathrm{Re}_{x_f} = 3.0 \times 10^6$, $F = 25 \times 10^{-6}$, $\beta_0 = 0.45$, and $\max_{x,y}(u'_{\mathrm{rms}}) = 0.15$. This initial disturbance is similar to the traditional optimal disturbances.

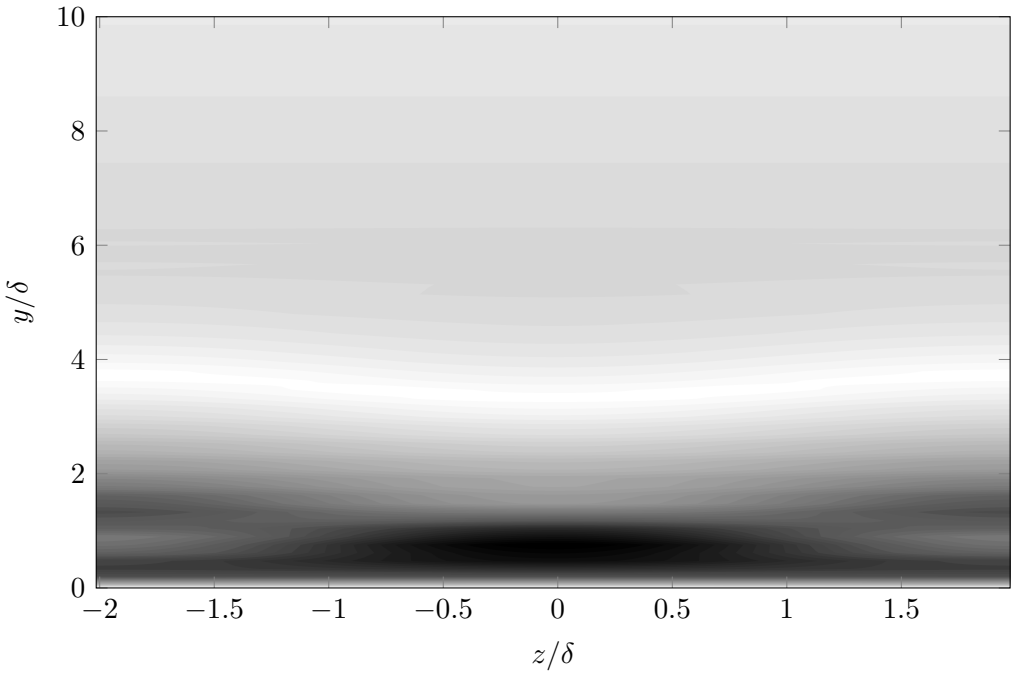

Figure 5.15: This is an example spanwise modulated TS mode shape that is the result of the initial disturbance which minimizes the spatial growth rate at $\mathrm{Re}_{x_f} = 3.0 \times 10^6$, $F = 25 \times 10^{-6}$, $\beta_0 = 0.45$, and $\max_{x,y}(u'_{\mathrm{rms}}) = 0.15$.

6. CONCLUSIONS AND FUTURE WORK

Transient growth helps explain roughness-induced transition to turbulence. Unlike primary instabilities of the LSE, such as TS waves, the disturbance growth rate is strongly dependent on receptivity. This fact is the main challenge in understanding transient growth. Previous researchers [17, 16, 48] addressed receptivity by computing the initial disturbances that caused the greatest disturbance kinetic energy growth. Although this approach sidesteps the receptivity question, the results were dissimilar to several experimental observations [18, 49, 19, 8] of laminar boundary layers encountering surface roughness.

Tumin [42] and Denissen & White [20] focused on the characterization of receptivity for known flows by extracting the amplitude functions for continuous spectrum modes of the LSE. This characterization unequivocally demonstrates that optimal disturbances and roughness-induced transient growth excite different continuous spectrum modes. In order to develop transient growth theory that is more characteristic of roughness, finding the disturbances that maximize secondary instability growth rate was the primary goal of this dissertation.

Nonlinear adjoint optimization of solutions of the PNS and BiGlobal stability equations has been used to compute optimal disturbances satisfying three objective functions: disturbance kinetic energy growth, sinuous instability growth rate, and TS wave growth rate. Computations involving the first objective function, referred to as traditional optimal disturbances, serve to validate the present optimization methods with previous results in literature. Maximization of sinuous instability growth rate results in transient disturbances similar to roughness-induced transient growth. And, finally, minimization of the TS wave growth rate reveals potential transition control

possibilities.

The traditional optimal disturbance results show good agreement with Andersson et al. [17] with slight differences in amplitude since the present computations were not started at the leading edge. Nonlinear effects reduce the disturbance kinetic energy growth by 25% at a disturbance amplitude of $\max_{x,y}(u'_{\text{rms}}) = 20\%$.

Maximizing the sinuous instability growth rate yields initial disturbances similar to observations from experiments and DNS. The initial disturbance that leads to the largest sinuous growth rate consists of counter-rotating streamwise vortices grouped together and located low in the boundary layer. Sinuous instabilities were found for disturbance amplitudes as low as $\max_{x,y}(u'_{\text{rms}}) = 2.5\%$. Similar to roughness experiments and the results of Denissen & White [24] there is a much larger potential for unstable sinuous modes in the near vicinity of the initial disturbance. Sinuous modes are shown to be unstable at nondimensional frequencies as low as $F = 50 \times 10^{-6}$ and up to at least $F = 700 \times 10^{-6}$.

Several previous researchers [22, 23, 78, 79] have shown that streamwise streaks can stabilize TS waves. However, this work was all based off of using linear traditional optimal disturbances as the initial condition. This research directly computes the disturbances that minimize the TS wave growth rate. These disturbances are evenly spaced similar to traditional optimal disturbances but are located slightly lower in the boundary layer. Significant stabilization can be realized, especially at higher frequencies. If one were to attempt to use these disturbances to delay transition, care would need to be taken not to generate too large of an amplitude and destabilize a sinuous mode.

Much of the parameter space for all three objective functions remains unexplored. Thus a future goal is the complete exploration of the parameter space. To accomplish this, the stability of both the PNS and optimization codes must be improved. A

first step in this direction would be to perform a Von Neumann stability analysis of the PNS code. This is not a straightforward task because there is nonuniform grid spacing in the wall-normal direction.

Once the parameter space has been more fully explored for incompressible Blasius flow, the next step would be to explore the parameter space for flow around an airfoil. This would be particularly interesting for the most-destabilizing disturbances as an analog for surface roughness and for the stabilization of TS waves for potential transition control.

For understanding future *in-situ* roughness configurations it is recommended to obtain the steady laminar flow using standard CFD methods with no turbulence modeling then compute the stability using the BiGlobal methods developed in Section 4.

REFERENCES

[1] Reynolds, O. (1883). "An experimental investigation of the circumstances which determine whether the motion of water shall be direct or sinuous, and of the law of resistance in parallel channels." In: *Proceedings of the Royal Society of London* 35.224-226, pp. 84–99.

[2] Tani, I. (1969). "Boundary-Layer Transition". In: *Annual Review of Fluid Mechanics* 1.1, pp. 169–196. ISSN: 1545-4479. DOI: 10.1146/annurev.fl.01.010169.001125. URL: http://dx.doi.org/10.1146/annurev.fl.01.010169.001125.

[3] Reshotko, E. (1976). "Boundary-Layer Stability and Transition". In: *Annual Review of Fluid Mechanics* 8.1, pp. 311–349. ISSN: 1545-4479. DOI: 10.1146/annurev.fl.08.010176.001523. URL: http://dx.doi.org/10.1146/annurev.fl.08.010176.001523.

[4] Reed, H. L., Saric, W. S., and Arnal, D. (1996). "Linear Stability Theory Applied to Boundary Layers". In: *Annual Review of Fluid Mechanics* 28.1, pp. 389–428. ISSN: 1545-4479. DOI: 10.1146/annurev.fl.28.010196.002133. URL: http://dx.doi.org/10.1146/annurev.fl.28.010196.002133.

[5] Smith, A. M. O. and Gamberoni, N. (1956). *Transition, pressure gradient and stability theory*. Douglas Aircraft Company, El Segundo Division.

[6] Van Ingen, J. (1956). *A suggested semi-empirical method for the calculation of the boundary layer transition region*. Tech. rep. Delft University of Technology.

[7] Borg, M. P. and Schneider, S. P. (2008). "Effect of Freestream Noise on Roughness-Induced Transition for the X-51A Forebody". In: *Journal of Spacecraft and Rockets* 45.6, pp. 1106–1116. ISSN: 1533-6794. DOI: 10.2514/1.38005. URL: http://dx.doi.org/10.2514/1.38005.

[8] Ergin, F. G. and White, E. B. (2006). "Unsteady and Transitional Flows Behind Roughness Elements". In: *AIAA Journal* 44.11, pp. 2504–2514. ISSN: 1533-385X. DOI: 10.2514/1.17459. URL: http://dx.doi.org/10.2514/1.17459.

[9] Reda, D. C. (2002). "Review and Synthesis of Roughness-Dominated Transition Correlations for Reentry Applications". In: *Journal of Spacecraft and Rockets* 39.2, pp. 161–167. ISSN: 0022-4650. DOI: 10.2514/2.3803. URL: http://dx.doi.org/10.2514/2.3803.

[10] Schneider, S. P. (2008). "Effects of Roughness on Hypersonic Boundary-Layer Transition". In: *Journal of Spacecraft and Rockets* 45.2, pp. 193–209. ISSN: 1533-6794. DOI: 10.2514/1.29713. URL: http://dx.doi.org/10.2514/1.29713.

[11] Reshotko, E. (2001). "Transient growth: A factor in bypass transition". In: *Physics of Fluids (1994-present)* 13.5, pp. 1067–1075. DOI: http://dx.doi.org/10.1063/1.1358308. URL: http://scitation.aip.org/content/aip/journal/pof2/13/5/10.1063/1.1358308.

[12] Ellingsen, T. and Palm, E. (1975). "Stability of linear flow". In: *Physics of Fluids (1958-1988)* 18.4, pp. 487–488. ISSN: 0031-9171. DOI: 10.1063/1.861156. URL: http://dx.doi.org/10.1063/1.861156.

[13] Landahl, M. T. (1977). "Dynamics of boundary layer turbulence and the mechanism of drag reduction". In: *Physics of Fluids (1958-1988)* 20.10, S55–S63. ISSN: 0031-9171. DOI: 10.1063/1.861759. URL: http://dx.doi.org/10.1063/1.861759.

[14] Landahl, M. T. (1980). "A note on an algebraic instability of inviscid parallel shear flows". In: *Journal of Fluid Mechanics* 98.02, pp. 243–251. ISSN: 1469-7645. DOI: 10.1017/s0022112080000122. URL: http://dx.doi.org/10.1017/S0022112080000122.

[15] Butler, K. M. and Farrell, B. F. (1992). "Three-dimensional optimal perturbations in viscous shear flow". In: *Physics of Fluids A: Fluid Dynamics (1989-1993)* 4.8, pp. 1637–1650. ISSN: 0899-8213. DOI: 10.1063/1.858386. URL: http://dx.doi.org/10.1063/1.858386.

[16] Luchini, P. (2000). "Reynolds-number-independent instability of the boundary layer over a flat surface: optimal perturbations". In: *Journal of Fluid Mechanics* 404, pp. 289–309. ISSN: 0022-1120. DOI: 10.1017/s0022112099007259. URL: http://dx.doi.org/10.1017/S0022112099007259.

[17] Andersson, P., Berggren, M., and Henningson, D. S. (1999). "Optimal disturbances and bypass transition in boundary layers". In: *Physics of Fluids* 11.1, p. 134. ISSN: 1070-6631. DOI: 10.1063/1.869908. URL: http://dx.doi.org/10.1063/1.869908.

[18] White, E. B. (2002). "Transient growth of stationary disturbances in a flat plate boundary layer". In: *Physics of Fluids (1994-present)* 14.12, pp. 4429–4439. DOI: http://dx.doi.org/10.1063/1.1521124. URL: http://scitation.aip.org/content/aip/journal/pof2/14/12/10.1063/1.1521124.

[19] White, E. B., Rice, J. M., and Ergin, F. G. (2005). "Receptivity of stationary transient disturbances to surface roughness". In: *Physics of Fluids (1994-present)* 17.6, 064109. DOI: http://dx.doi.org/10.1063/1.1938217. URL: http://scitation.aip.org/content/aip/journal/pof2/17/6/10.1063/1.1938217.

[20] Denissen, N. A. and White, E. B. (2009). "Continuous spectrum analysis of roughness-induced transient growth". In: *Physics of Fluids (1994-present)* 21.11. ISSN: 1070-6631. DOI: 10.1063/1.3264090. URL: http://dx.doi.org/10.1063/1.3264090.

[21] Andersson, P., Brandt, L., Bottaro, A., and Henningson, D. S. (2001). "On the breakdown of boundary layer streaks". In: *Journal of Fluid Mechanics* 428, pp. 29–60. ISSN: 0022-1120. DOI: 10.1017/s0022112000002421. URL: http://dx.doi.org/10.1017/S0022112000002421.

[22] Cossu, C. and Brandt, L. (2002). "Stabilization of Tollmien–Schlichting waves by finite amplitude optimal streaks in the Blasius boundary layer". In: *Physics of Fluids (1994-present)* 14.8, pp. L57–L60. ISSN: 1070-6631. DOI: 10.1063/1.1493791. URL: http://dx.doi.org/10.1063/1.1493791.

[23] Cossu, C. and Brandt, L. (2004). "On Tollmien–Schlichting-like waves in streaky boundary layers". In: *European Journal of Mechanics - B/Fluids* 23.6, pp. 815–833. ISSN: 0997-7546. DOI: 10.1016/j.euromechflu.2004.05.001. URL: http://dx.doi.org/10.1016/j.euromechflu.2004.05.001.

[24] Denissen, N. A. and White, E. B. (2013). "Secondary instability of roughness-induced transient growth". In: *Physics of Fluids (1994-present)* 25.11. ISSN: 1070-6631. DOI: 10.1063/1.4829482. URL: http://dx.doi.org/10.1063/1.4829482.

[25] Saric, W. S., Reed, H. L., and Kerschen, E. J. (2002). "Boundary-Layer Receptivity to Freestream Disturbances". In: *Annual Review of Fluid Mechanics* 34.1, pp. 291–319. ISSN: 1545-4479. DOI: 10.1146/annurev.fluid.34.082701.161921. URL: http://dx.doi.org/10.1146/annurev.fluid.34.082701.161921.

[26] Dryden, H. L. (1959). "Transition from laminar to turbulent flow". In: *Turbulent flows and heat transfer* 5, pp. 3–74.

[27] Smith, A. M. O. and Clutter, D. W. (1959). "The Smallest Height of Roughness Capable of Affecting Boundary-Layer Transition". In: *Journal of the Aerospace Sciences* 26.4, pp. 229–245. DOI: 10.2514/8.8019. URL: http://arc.aiaa.org/doi/abs/10.2514/8.8019.

[28] Tani, I. (1961). "Effect of two-dimensional and isolated roughness on laminar flow". In: *Boundary Layer and Flow Control*. Vol. 2. Pergamon Press, pp. 637–656.

[29] Von Doenhoff, A. E. and Braslow, A. L. (1961). "The effect of distributed surface roughness on laminar flow". In: *Boundary Layer and Flow Control*. Vol. 2. Pergamon Press, pp. 657–681.

[30] Sedney, R. (1973). "A survey of the effects of small protuberances on boundary-layer flows". In: *AIAA Journal* 11.6, pp. 782–792.

[31] Gregory, N. and Walker, W. (1956). *The effect on transition of isolated surface excrescences in the boundary layer*. Tech. rep. R&M 2779. Aeronautical Research Council.

[32] Klebanoff, P. S., Cleveland, W. G., and Tidstrom, K. D. (1992). "On the evolution of a turbulent boundary layer induced by a three-dimensional roughness element". In: *Journal of Fluid Mechanics* 237.-1, p. 101. ISSN: 1469-7645. DOI: 10.1017/s0022112092003379. URL: http://dx.doi.org/10.1017/S0022112092003379.

[33] Choudhari, M., Li, F., Chang, C.-L., Edwards, J., Kegerise, M., and King, R. (2010). "Laminar–Turbulent Transition behind Discrete Roughness Elements in a High-Speed Boundary Layer". In: 48^{th} *AIAA Aerospace Sciences Meeting Including the New Horizons Forum and Aerospace Exposition*. 1575. American Institute of Aeronautics and Astronautics, p. 2010. ISBN: http://id.crossref.org/isbn/978-1-60086-959-4. DOI: 10.2514/6.2010-1575. URL: http://dx.doi.org/10.2514/6.2010-1575.

[34] Kegerise, M. A., King, R. A., Owens, L. R., Choudhari, M. M., Norris, A. T., Li, F., and Chang, C.-L. (2012). "An experimental and numerical study of roughness-induced instabilities in a Mach 3.5 boundary layer". In: *RTO AVT-200 RSM-030 Specialists' Meeting on Hypersonic Laminar-Turbulent Transition* NF1676L-14423.

[35] De Tullio, N., Paredes, P., Sandham, N. D., and Theofilis, V. (2013). "Laminar–turbulent transition induced by a discrete roughness element in a supersonic boundary layer". In: *Journal of Fluid Mechanics* 735, pp. 613–646. ISSN: 1469-7645. DOI: 10.1017/jfm.2013.520. URL: http://dx.doi.org/10.1017/jfm.2013.520.

[36] Kegerise, M. A., King, R. A., Choudhari, M., Li, F., and Norris, A. T. (2014). "An Experimental Study of Roughness-Induced Instabilities in a Supersonic

Boundary Layer". In: 7^{th} *AIAA Theoretical Fluid Mechanics Conference*. DOI: 10.2514/6.2014-2501. URL: http://dx.doi.org/10.2514/6.2014-2501.

[37] Choudhari, M. M., Li, F., Bynum, M. D., Kegerise, M. A., and King, R. A. (2015). "Computations of Disturbance Amplification Behind Isolated Roughness Elements and Comparison with Measurements". In: 45^{th} *AIAA Fluid Dynamics Conference*. DOI: 10.2514/6.2015-2625. URL: http://dx.doi.org/10.2514/6.2015-2625.

[38] Denissen, N. A. (2011). "Roughness-induced Transient Growth: Continuous-spectrum Receptivity and Secondary Instability Analysis". Ph.D. dissertation. Texas A&M University.

[39] Morkovin, M. V., Reshotko, E., and Herbert, T. (1994). "Transition in open flow systems—a reassessment". In: *Bull. Am. Phys. Soc* 39.9, p. 1882.

[40] Westin, K. J. A., Boiko, A. V., Klingmann, B. G. B., Kozlov, V. V., and Alfredsson, P. H. (1994). "Experiments in a boundary layer subjected to free stream turbulence. Part 1. Boundary layer structure and receptivity". In: *Journal of Fluid Mechanics* 281.-1, p. 193. ISSN: 1469-7645. DOI: 10.1017/s0022112094003083. URL: http://dx.doi.org/10.1017/S0022112094003083.

[41] Grosch, C. E. and Salwen, H. (1978). "The continuous spectrum of the Orr–Sommerfeld equation. Part 1. The spectrum and the eigenfunctions". In: *Journal of Fluid Mechanics* 87.01, p. 33. ISSN: 1469-7645. DOI: 10.1017/s0022112078002918. URL: http://dx.doi.org/10.1017/S0022112078002918.

[42] Tumin, A. (2003). "Multimode decomposition of spatially growing perturbations in a two-dimensional boundary layer". In: *Physics of Fluids (1994-present)* 15.9, pp. 2525–2540. DOI: http://dx.doi.org/10.1063/1.1597453. URL: http://scitation.aip.org/content/aip/journal/pof2/15/9/10.1063/1.1597453.

[43] Scott, M. R. and Watts, H. A. (1977). "Computational Solution of Linear Two-Point Boundary Value Problems via Orthonormalization". In: *SIAM Journal on Numerical Analysis* 14.1, pp. 40–70. ISSN: 1095-7170. DOI: 10.1137/0714004. URL: http://dx.doi.org/10.1137/0714004.

[44] Tumin, A. and Reshotko, E. (2005). "Receptivity of a boundary-layer flow to a three-dimensional hump at finite Reynolds numbers". In: *Physics of Fluids* 17.9, p. 094101. ISSN: 1070-6631. DOI: 10.1063/1.2033907. URL: http://dx.doi.org/10.1063/1.2033907.

[45] Smith, F. T., Sykes, R. I., and Brighton, P. W. M. (1977). "A two-dimensional boundary layer encountering a three-dimensional hump". In: *Journal of Fluid Mechanics* 83.01, p. 163. ISSN: 1469-7645. DOI: 10.1017/s0022112077001128. URL: http://dx.doi.org/10.1017/S0022112077001128.

[46] Zuccher, S., Bottaro, A., and Luchini, P. (2006). "Algebraic growth in a Blasius boundary layer: Nonlinear optimal disturbances". In: *European Journal of Mechanics - B/Fluids* 25.1, pp. 1–17. ISSN: 0997-7546. DOI: 10.1016/j.euromechflu.2005.07.001. URL: http://dx.doi.org/10.1016/j.euromechflu.2005.07.001.

[47] Schmid, P. J. and Henningson, D. S. (1994). "Optimal energy density growth in Hagen–Poiseuille flow". In: *Journal of Fluid Mechanics* 277, pp. 197–225. ISSN: 1469-7645. DOI: 10.1017/s0022112094002739. URL: http://dx.doi.org/10.1017/S0022112094002739.

[48] Tumin, A. and Reshotko, E. (2001). "Spatial theory of optimal disturbances in boundary layers". In: *Physics of Fluids (1994-present)* 13.7, pp. 2097–2104. DOI: http://dx.doi.org/10.1063/1.1378070. URL: http://scitation.aip.org/content/aip/journal/pof2/13/7/10.1063/1.1378070.

[49] Fransson, J. H. M., Brandt, L., Talamelli, A., and Cossu, C. (2004). "Experimental and theoretical investigation of the nonmodal growth of steady streaks in a flat plate boundary layer". In: *Physics of Fluids* 16.10, p. 3627. ISSN: 1070-6631. DOI: 10.1063/1.1773493. URL: http://dx.doi.org/10.1063/1.1773493.

[50] Rizzetta, D. P. and Visbal, M. R. (2007). "Direct Numerical Simulations of Flow Past an Array of Distributed Roughness Elements". In: *AIAA Journal* 45.8, pp. 1967–1976. ISSN: 1533-385X. DOI: 10.2514/1.25916. URL: http://dx.doi.org/10.2514/1.25916.

[51] Saric, W. S. and Nayfeh, A. H. (1975). "Nonparallel stability of boundary-layer flows". In: *Physics of Fluids (1958-1988)* 18.8, pp. 945–950. ISSN: 0031-9171. DOI: 10.1063/1.861266. URL: http://dx.doi.org/10.1063/1.861266.

[52] Tumin, A. (2008). "Nonparallel Flow Effects on Roughness-Induced Perturbations in Boundary Layers". In: *Journal of Spacecraft and Rockets* 45.6, pp. 1176–1184. ISSN: 1533-6794. DOI: 10.2514/1.37136. URL: http://dx.doi.org/10.2514/1.37136.

[53] Paredes, P., Hermanns, M., Le Clainche, S., and Theofilis, V. (2013). "Order 10^4 speedup in global linear instability analysis using matrix formation". In: *Computer Methods in Applied Mechanics and Engineering* 253, pp. 287–304.

ISSN: 0045-7825. DOI: 10.1016/j.cma.2012.09.014. URL: http://dx.doi.org/10.1016/j.cma.2012.09.014.

[54] Rubin, S. G. and Tannehill, J. C. (1992). "Parabolized/Reduced Navier–Stokes Computational Techniques". In: *Annual Review of Fluid Mechanics* 24.1, pp. 117–144. ISSN: 1545-4479. DOI: 10.1146/annurev.fl.24.010192.001001. URL: http://dx.doi.org/10.1146/annurev.fl.24.010192.001001.

[55] Malik, M. (1990). "Numerical methods for hypersonic boundary layer stability". In: *Journal of Computational Physics* 86.2, pp. 376–413. ISSN: 0021-9991. DOI: 10.1016/0021-9991(90)90106-b. URL: http://dx.doi.org/10.1016/0021-9991(90)90106-B.

[56] Aris, R. (1990). *Vectors, tensors and the basic equations of fluid mechanics*. Courier Dover Publications.

[57] Anderson Jr., J. D. (2006). *Hypersonic and High-Temperature Gas Dynamics, Second Edition*. Second Edition. American Institute of Aeronautics and Astronautics. ISBN: http://id.crossref.org/isbn/978-1-60086-195-6. DOI: 10.2514/4.861956. URL: http://dx.doi.org/10.2514/4.861956.

[58] Hall, P. and Horseman, N. J. (1991). "The linear inviscid secondary instability of longitudinal vortex structures in boundary layers". In: *Journal of Fluid Mechanics* 232, pp. 357–375. ISSN: 1469-7645. DOI: 10.1017/s0022112091003725. URL: http://dx.doi.org/10.1017/S0022112091003725.

[59] Henningson, D. S. (1987). "Stability of parallel inviscid shear flow with mean spanwise variation". In: *NASA STI/Recon Technical Report N* 88, p. 28285.

[60] Schmid, P. J. and Henningson, D. S. (2001). *Stability and transition in shear flows*. Vol. 142. Springer.

[61] Bridges, T. and Morris, P. (1984). "Differential eigenvalue problems in which the parameter appears nonlinearly". In: *Journal of Computational Physics* 55.3, pp. 437–460. ISSN: 0021-9991. DOI: 10.1016/0021-9991(84)90032-9. URL: http://dx.doi.org/10.1016/0021-9991(84)90032-9.

[62] Denissen, N. and White, E. (2011). "Secondary Instability of Roughness Wakes and Optimal Disturbances". In: 49^{th} *AIAA Aerospace Sciences Meeting including the New Horizons Forum and Aerospace Exposition*. 562. American Institute of Aeronautics and Astronautics. ISBN: http://id.crossref.org/isbn/978-1-60086-950-1. DOI: 10.2514/6.2011-562. URL: http://dx.doi.org/10.2514/6.2011-562.

[63] Hermanns, M. and Hernández, J. A. (2007). "Stable high-order finite-difference methods based on non-uniform grid point distributions". In: *International Journal for Numerical Methods in Fluids* 56.3, pp. 233–255. ISSN: 1097-0363. DOI: 10.1002/fld.1510. URL: http://dx.doi.org/10.1002/fld.1510.

[64] Heroux, M. A., Phipps, E. T., Salinger, A. G., Thornquist, H. K., Tuminaro, R. S., Willenbring, J. M., Williams, A., Stanley, K. S., Bartlett, R. A., Howle, V. E., and al., et (2005). "An overview of the Trilinos project". In: *ACM Transactions on Mathematical Software* 31.3, pp. 397–423. ISSN: 0098-3500. DOI: 10.1145/1089014.1089021. URL: http://dx.doi.org/10.1145/1089014.1089021.

[65] Arnoldi, W. E. (1951). "The principle of minimized iterations in the solution of the matrix eigenvalue problem". In: *Quarterly of Applied Mathematics* 9.1, pp. 17–29.

[66] Kuzmin, A., Luisier, M., and Schenk, O. (2013). "Fast Methods for Computing Selected Elements of the Green's Function in Massively Parallel Nanoelectronic Device Simulations". In: *Lecture Notes in Computer Science*, pp. 533–544. ISSN: 1611-3349. DOI: 10.1007/978-3-642-40047-6_54. URL: http://dx.doi.org/10.1007/978-3-642-40047-6_54.

[67] Schenk, O., Bollhöfer, M., and Römer, R. A. (2008). "On Large-Scale Diagonalization Techniques for the Anderson Model of Localization". In: *SIAM Review* 50.1, pp. 91–112. ISSN: 1095-7200. DOI: 10.1137/070707002. URL: http://dx.doi.org/10.1137/070707002.

[68] Schenk, O., Wächter, A., and Hagemann, M. (2007). "Matching-based preprocessing algorithms to the solution of saddle-point problems in large-scale nonconvex interior-point optimization". English. In: *Computational Optimization and Applications* 36.2-3, pp. 321–341. ISSN: 0926-6003. DOI: 10.1007/s10589-006-9003-y. URL: http://dx.doi.org/10.1007/s10589-006-9003-y.

[69] Saad, Y. (2003). *Iterative methods for sparse linear systems*. Second Edition. SIAM.

[70] Kuester, M. S. and White, E. B. (2015). "Roughness Receptivity and Shielding in a Flat Plate Boundary Layer". In: *Journal of Fluid Mechanics (Under Review)*.

[71] Hunt, L., Downs, R., Kuester, M., White, E., and Saric, W. (2010). "Flow Quality Measurements in the Klebanoff-Saric Wind Tunnel". In: 27^{th} *AIAA Aerodynamic Measurement Technology and Ground Testing Conference*. 4538. American Institute of Aeronautics and Astronautics. ISBN: http://id.cross-

ref.org/isbn/978-1-62410-142-7. DOI: 10.2514/6.2010-4538. URL: http://dx.doi.org/10.2514/6.2010-4538.

[72] Drews, S. D. (2012). "Direct Numerical Simulation of Flow Past Quasti-Random Distributed Roughness". Master's thesis. University of Texas at Austin.

[73] Sharp, N. S. (2014). "Hypersonic Measurements of Roughness-Induced Transient Growth". Ph.D. dissertation. Texas A&M University.

[74] Hofferth, J., Bowersox, R., and Saric, W. (2010). "The Mach 6 Quiet Tunnel at Texas A&M: Quiet Flow Performance". In: 27^{th} *AIAA Aerodynamic Measurement Technology and Ground Testing Conference*. DOI: 10.2514/6.2010-4794. URL: http://dx.doi.org/10.2514/6.2010-4794.

[75] Nadarajah, S. and Jameson, A. (2000). "A comparison of the continuous and discrete adjoint approach to automatic aerodynamic optimization". In: *AIAA paper* 667, p. 2000.

[76] Johnson, S. G. (2007). *Notes on Adjoint Methods for 18.336*. http://ocw.mit.edu/courses/mathematics/18-335j-introduction-to-numerical-methods-fall-2010/lecture-notes/MIT18_335JF10_lec23b_hand.pdf.

[77] Jeong, J. and Hussain, F. (1995). "On the identification of a vortex". In: *Journal of Fluid Mechanics* 285.-1, p. 69. ISSN: 1469-7645. DOI: 10.1017/s0022112095000462. URL: http://dx.doi.org/10.1017/S0022112095000462.

[78] Bagheri, S. and Hanifi, A. (2007). "The stabilizing effect of streaks on Tollmien–Schlichting and oblique waves: A parametric study". In: *Physics of Fluids (1994-present)* 19.7. ISSN: 1070-6631. DOI: 10.1063/1.2746047. URL: http://dx.doi.org/10.1063/1.2746047.

[79] Shahinfar, S., Fransson, J. H. M., Sattarzadeh, S. S., and Talamelli, A. (2013). "Scaling of streamwise boundary layer streaks and their ability to reduce skin-friction drag". In: *Journal of Fluid Mechanics* 733, pp. 1–32. ISSN: 1469-7645. DOI: 10.1017/jfm.2013.431. URL: http://dx.doi.org/10.1017/jfm.2013.431.

[80] Archer, B. and Weisstein, E. W. (2015). "Lagrange Interpolating Polynomial". In: *MathWorld–A Wolfram Web Resource*. URL: http://mathworld.wolfram.com/LagrangeInterpolatingPolynomial.html.

[81] Fornberg, B. (1998). "Classroom Note: Calculation of Weights in Finite Difference Formulas". In: *SIAM Review* 40.3, pp. 685–691. ISSN: 1095-7200.

DOI: 10.1137/s0036144596322507. URL: http://dx.doi.org/10.1137/S0036144596322507.

[82] Eisinberg, A. and Fedele, G. (2005). "Vandermonde systems on Gauss–Lobatto Chebyshev nodes". In: *Applied Mathematics and Computation* 170.1, pp. 633–647. ISSN: 0096-3003. DOI: 10.1016/j.amc.2004.12.046. URL: http://dx.doi.org/10.1016/j.amc.2004.12.046.

[83] Müntz, C. (1913). "Solution direct de l'équation séculaire et de quelques problémes analogues transcendaants". In: *Comptus Rendus de l'Académie des Sciences* 156, pp. 43–46.

[84] Paredes, P., Rodríguez, D., and Theofilis, V. (2013). "Three-Dimensional Solutions of Trailing-Vortex Flows Using Parabolized Equations". In: *AIAA Journal* 51.12, pp. 2763–2770. ISSN: 1533-385X. DOI: 10.2514/1.j052338. URL: http://dx.doi.org/10.2514/1.J052338.

APPENDIX A

NUMERICAL METHODS

A.1 Finite Differences

The advent and widespread use of digital computers during the 20$^{\text{th}}$ century has enabled the simulation of many complex physical problems governed by partial differential equations (PDEs). Computers are able to obtain approximate solutions to these PDEs by approximating the continuous domain by many discrete points. The PDEs are then enforced at these discrete points using approximations of the derivatives. The main method of derivative approximation used in this work is *finite differences*.

Finite differences are approximations to the derivative of a quantity found by the weighted summation of the quantity at nearby points, where the weights depend solely on the discretization. For example, the derivative of a general function $f(x)$ can be written as:

$$\left.\frac{df}{dx}\right|_{x=x_i} \approx \delta_x[f](x_i) = \sum_{j=-q/2}^{q/2} c_j f_{i+j}, \tag{A.1}$$

where f_i are the function values at the discrete x coordinates x_i for $i = 0,\ 2,\ \ldots,\ N_x$, $N_x + 1$ is the total number of discrete x coordinates, $q + 1$ is the number of points used to approximate the derivative, and c_j are the finite difference weights determined from x_i. In the above equation a short-hand notation for finite differences has been introduced:

$$\left.\frac{df}{dx}\right|_{x=x_i} \approx \delta_x[f](x_i).$$

In this notation, δ is the finite difference operator, the subscript is the coordinate

along which the operator acts, the term in square brackets is the quantity that it acts on, and the discrete coordinate(s) in the parenthesis indicate the location of the approximation. Since the finite difference expansion in Eq. (A.1) has an equal number of points on both sides of the discrete coordinate where the derivative is being approximated, it is referred to as a central difference. Forwards and backwards differences are obtained when the limits on the summation are changed to $[0,\ q]$ and $[-q,\ 0]$, respectively. Forwards and backwards differences are often used at domain boundaries and for numerical considerations such as the use of upwind schemes for handling shockwaves in compressible CFD. In this section only central differences will be considered, however, similar methods can be used to obtain the weights c_j for both forward and backwards differences.

There are two main methods of obtaining the weights, c_j, for finite differences: Taylor series expansion and Lagrange interpolation. The Taylor series expansion technique is best for demonstrating the order of accuracy but the Lagrange interpolation method makes the process of determining the weights for arbitrary spaced grids trivial.

To obtain the finite difference approximation, $\delta_x[f](x_i)$, first expand $f(x)$ around $x = x_i$:

$$f(x) = f(x_i) + \frac{df(x_i)}{dx}(x - x_i) + \frac{d^2f(x_i)}{dx^2}\frac{(x - x_i)^2}{2} + \frac{d^3f(x_i)}{dx^3}\frac{(x - x_i)^3}{3!} + \cdots .$$

Now lets use the above Taylor series expansion to obtain expressions for $f(x_{i-1})$ and $f(x_{i+1})$:

$$f(x_{i-1}) = f(x_i) + \frac{df(x_i)}{dx}(x_{i-1} - x_i) + \frac{d^2f(x_i)}{dx^2}\frac{(x_{i-1} - x_i)^2}{2!} + \frac{d^3f(x_i)}{dx^3}\frac{(x_{i-1} - x_i)^3}{3!} + \cdots , \tag{A.2}$$

$$f(x_{i+1}) = f(x_i) + \frac{df(x_i)}{dx}(x_{i+1} - x_i) + \frac{d^2f(x_i)}{dx^2}\frac{(x_{i+1} - x_i)^2}{2!} + \frac{d^3f(x_i)}{dx^3}\frac{(x_{i+1} - x_i)^3}{3!} + \cdots . \tag{A.3}$$

Next Eq. (A.2) is subtracted from Eq. (A.3):

$$f(x_{i+1}) - f(x_{i-1}) = \frac{df(x_i)}{dx}(x_{i+1} - x_{i-1}) + \frac{d^2f(x_i)}{dx^2}\left[\frac{(x_{i+1} - x_i)^2 - (x_{i-1} - x_i)^2}{2!}\right] + \frac{d^3f(x_i)}{dx^3}\left[\frac{(x_{i+1} - x_i)^3 - (x_{i-1} - x_i)^3}{3!}\right] + \cdots . \tag{A.4}$$

After rearranging, an expression for the derivative is found:

$$\frac{df(x_i)}{dx} = \frac{f(x_{i+1}) - f(x_{i-1})}{(x_{i+1} - x_{i-1})} + \frac{d^2f(x_i)}{dx^2}\left[\frac{(x_{i-1} - x_i)^2 - (x_{i+1} - x_i)^2}{2!\,(x_{i+1} - x_{i-1})}\right] + \frac{d^3f(x_i)}{dx^3}\left[\frac{(x_{i-1} - x_i)^3 - (x_{i+1} - x_i)^3}{3!\,(x_{i+1} - x_{i-1})}\right] + \cdots . \tag{A.5}$$

For the special case of a uniform grid with spacing Δx, the finite difference expression above reduces to:

$$\frac{df(x_i)}{dx} = \frac{f(x_{i+1}) - f(x_{i-1})}{2\Delta x} - \frac{d^3f(x_i)}{dx^3}\left[\frac{\Delta x^2}{3!}\right] + \cdots . \tag{A.6}$$

The last term in the equation above is the leading truncation error of this finite difference approximation. The only portion of this term that the user has any control over is the grid spacing, Δx. This finite difference approximation is classified as 2^{nd}-order because the truncation error decreases proportionally to Δx^2 as the grid spacing is reduced. It is important to note that this expansion is only 1^{st}-order for non-uniform grid spacing. For uniform grid spacing the order of accuracy of central

finite differences is equal to q, where q is defined as in Eq. (A.1).

The other method of obtaining the finite difference weights is called Lagrange interpolation. A Lagrange interpolating polynomial [80] is the polynomial of least degree passing through the points $(x_j,\ f_j)$ for $j = 0,\ 2,\ \ldots,\ q$. The Lagrange interpolation polynomial, $P(x)$ can be written as:

$$P(x) = \sum_{j=0}^{q} P_j(x), \tag{A.7}$$

where

$$P_j(x) = f_j \prod_{\substack{k=0 \\ k \neq j}}^{q} \frac{x - x_k}{x_j - x_k}.$$

The finite difference weights are easily found by differentiating Eq. (A.7). For this work, the algorithm developed by Fornberg [81] has been used to obtain the finite difference weights on arbitrarily spaced grids.

A.2 FD-q Method

Higher-order finite differences (in this work defined as $q > 2$) can lead to inaccurate results near the edges of bounded domains. To illustrate this point, consider the following polynomial approximation of the function $u(x)$:

$$u(x) \approx f_i(x) = \sum_{j=s_i}^{s_i+q} c_{ij}(x) u_j,$$

where

$$s_i = \underbrace{0,\ \ldots,\ 0}_{q/2 \text{ times}},\ \underbrace{0,\ 1,\ \ldots,\ N_x - q}_{\text{centered FD}},\ \underbrace{N_x - q,\ \ldots,\ N_x - q}_{q/2 \text{ times}}.$$

Derivatives of $u(x)$ can then be found by taking derivatives of the interpolation polynomial $f_i(x)$. The error of this approximation is defined as:

$$\epsilon_i(x) = u(x) - f_i(x) = \pi_i(x)\frac{u^{(q+1)}(x)}{(q+1)!},$$

where

$$\pi_i(x) = \prod_{m=0}^{q}(x - x_{s_i+m}).$$

The error consists of two components: the $(q+1)^{\text{st}}$ derivative of $u(x)$ and the polynomial $\pi_i(x)$. Nothing can be done about the smoothness of the function being approximated, but $\pi_i(x)$ can be minimized over the domain of interest. [63] High-order finite differences become unstable near the domain boundaries because $\pi_i(x)$ grows rapidly as q is increased.

One solution developed by Hermanns & Hernandez [63], referred to as the FD-q method, is to solve for the grid x_j such that $\pi_i(x)$ is uniform over the domain. This entails solving a system of nonlinear equations to obtain the grid $x_j = [-1,\ 1]$ that must be mapped to the physical domain. As $q \to N_x$, the grid converges to the Gauss–Lobatto–Chebyshev nodes. [82]

A.3 Curvilinear Coordinates

The equations in sections 3.2 & 4.1 were left in terms of tensor calculus operators so that they could be applied to general curvilinear coordinates. A curvilinear coordinate system can be defined by the associated transformation to Cartesian coordinates:

$$\bar{x}^i = \bar{x}^i(x^1, x^2, x^3),$$

where $\bar{x}^i$ are the coordinates of a Cartesian coordinate system and x^j are coordinates of a general coordinate system [56]. The metric tensor is then defined as:

$$g_{ij} = \frac{\partial \bar{x}^k}{\partial x^i} \frac{\partial \bar{x}^k}{\partial x^j}.$$

For orthogonal coordinates, the metric tensor is diagonal and the following definition is convenient:

$$g_{ii} = h_i^2 \quad \text{(no summation)}.$$

All differentiation by the tensor calculus operators is expressed using covariant differentiation. The covariant derivative is defined for contravariant vectors as:

$$A^i_{;j} = \frac{\partial A^i}{\partial x^j} + \Gamma^i_{jk} A^k,$$

where A^i is an arbitrary contravariant vector and Γ^i_{jk} is the Christoffel symbol of the 2^{nd} kind and is defined as:

$$\Gamma^i_{jk} = \frac{1}{2} g^{im} \left(g_{mj,k} + g_{mk,j} - g_{jk,m} \right).$$

Differentiation of 2^{nd}-order tensors is similar:

$$T^i_{j;k} = \frac{\partial T^i_j}{\partial x^k} + \Gamma^i_{km} T^m_j - \Gamma^m_{kj} T^i_m.$$

Because the basic state data used is physical, the covariant and contravariant vectors and tensors must be converted to physical components. Physical components of contravariant and covariant vectors in orthogonal coordinates can be obtained as:

$$A(i) = h_i A^i,$$

$$A(i) = \frac{1}{h_i} A_i,$$

respectively with no summation on i. Physical components of tensors are obtained as if each index was treated independently, for example:

$$T(ij) = \frac{h_i}{h_j} T^i_j,$$

where T is an arbitrary second-order tensor and there is no summation on i or j. As an example, the convective operator is written in orthogonal coordinates as:

$$\begin{aligned}
\boldsymbol{A} \cdot \nabla \boldsymbol{B} &= \sum_j A(j) \frac{h_i}{h_j} \left[B^i_{;j} \right] \\
&= \sum_{j,k} A(j) \frac{h_i}{h_j} \left[\frac{\partial B^i}{\partial x^j} + \Gamma^i_{jk} B^k \right] \\
&= \sum_{j,k} A(j) \frac{h_i}{h_j} \left[\frac{\partial}{\partial x^j} \left(\frac{B(i)}{h_i} \right) + \Gamma^i_{jk} \frac{B(k)}{h_k} \right] \\
&= \sum_{j,k} A(j) \frac{h_i}{h_j} \left[\frac{1}{h_i} \frac{\partial B(i)}{\partial x^j} - \frac{B(i)}{h_i^2} \frac{\partial h_i}{\partial x^j} + \Gamma^i_{jk} \frac{B(k)}{h_k} \right],
\end{aligned}$$

with no summation on i.

A.4 Newton Iterations

Solutions to a linear system of equations are easily computed using methods such as LU decomposition or Gauss–Seidel. However, solutions to nonlinear systems of equations are not as easily obtained. One method to solve nonlinear systems is called

Newton iterations. First a general system of equations is written as:

$$\begin{aligned} f_1(x_1,\, x_2,\, \ldots,\, x_n) &= 0 \\ f_2(x_1,\, x_2,\, \ldots,\, x_n) &= 0 \\ &\vdots \\ f_n(x_1,\, x_2,\, \ldots,\, x_n) &= 0 \end{aligned}$$

and the values of $\boldsymbol{x} = [x_1,\, x_2,\, \ldots,\, x_n]^T$ that satisfy the equations above is desired. This system of equations can be written succinctly as:

$$\boldsymbol{F}(\boldsymbol{x}) = \boldsymbol{0}. \tag{A.8}$$

Newton iterations are the generalization of Newton's method for one variable to n variables. Similarly, an initial guess, $\boldsymbol{x}_0$ for the solution is needed. A linear approximation of $\boldsymbol{F}$ can be written as:

$$\boldsymbol{F}(\boldsymbol{x}) \approx \boldsymbol{F}(\boldsymbol{x}_0) + \left.\frac{\partial \boldsymbol{F}}{\partial \boldsymbol{x}}\right|_{\boldsymbol{x}_0} (\boldsymbol{x} - \boldsymbol{x}_0)\,, \tag{A.9}$$

where

$$\left.\frac{\partial \boldsymbol{F}}{\partial \boldsymbol{x}}\right|_{\boldsymbol{x}_0} = \begin{pmatrix} \frac{\partial f_1}{\partial x_1}(\boldsymbol{x}_0) & \frac{\partial f_1}{\partial x_2}(\boldsymbol{x}_0) & \frac{\partial f_1}{\partial x_3}(\boldsymbol{x}_0) & \cdots & \frac{\partial f_1}{\partial x_n}(\boldsymbol{x}_0) \\ \frac{\partial f_2}{\partial x_1}(\boldsymbol{x}_0) & \frac{\partial f_2}{\partial x_2}(\boldsymbol{x}_0) & \frac{\partial f_2}{\partial x_3}(\boldsymbol{x}_0) & \cdots & \frac{\partial f_2}{\partial x_n}(\boldsymbol{x}_0) \\ \vdots & \vdots & \vdots & \ddots & \vdots \\ \frac{\partial f_n}{\partial x_1}(\boldsymbol{x}_0) & \frac{\partial f_n}{\partial x_2}(\boldsymbol{x}_0) & \frac{\partial f_n}{\partial x_3}(\boldsymbol{x}_0) & \cdots & \frac{\partial f_n}{\partial x_n}(\boldsymbol{x}_0) \end{pmatrix}.$$

A solution to the nonlinear system is obtained when $\boldsymbol{F}(\boldsymbol{x}) = \boldsymbol{0}$. By substituting this into Eq. (A.9):

$$\boldsymbol{F}(\boldsymbol{x}_0) + \left.\frac{\partial \boldsymbol{F}}{\partial \boldsymbol{x}}\right|_{\boldsymbol{x}_0} (\boldsymbol{x}_1 - \boldsymbol{x}_0) = \boldsymbol{0}, \tag{A.10}$$

an improved solution estimate, $\boldsymbol{x}_1$, is obtained:

$$\boldsymbol{x}_1 = \boldsymbol{x}_0 - \left[\left.\frac{\partial \boldsymbol{F}}{\partial \boldsymbol{x}}\right|_{\boldsymbol{x}_0}\right]^{-1} \boldsymbol{F}(\boldsymbol{x}_0). \tag{A.11}$$

Since $\frac{\partial \boldsymbol{F}}{\partial \boldsymbol{x}}(\boldsymbol{x}_i)$ is a known matrix, it is more common to write the Newton iteration method as a two step process:

$$\begin{aligned} \left.\frac{\partial \boldsymbol{F}}{\partial \boldsymbol{x}}\right|_{\boldsymbol{x}_i} \Delta\boldsymbol{x} &= -\boldsymbol{F}(\boldsymbol{x}_i), \\ \boldsymbol{x}_{i+1} &= \boldsymbol{x}_i + \Delta\boldsymbol{x}. \end{aligned} \tag{A.12}$$

Eq. (A.12) is a linear equation that can be solved using LU decomposition.

A.5 Arnoldi Iteration Method

The power iteration [83] method is a widely used technique for obtaining the largest eigenvalue of:

$$\boldsymbol{C}\boldsymbol{x} = \lambda \boldsymbol{x}. \tag{A.13}$$

It is a very simple algorithm that consists of repeated multiplication of the matrix $\boldsymbol{C}$ with an arbitrary non-zero starting vector $\boldsymbol{b}^{(0)}$:

$$\boldsymbol{b}^{(n+1)} = \boldsymbol{C}\boldsymbol{b}^{(n)}. \tag{A.14}$$

After each step, $\boldsymbol{b}^{(n+1)}$ is normalized so that $\left\|\boldsymbol{b}^{(n+1)}\right\|_2 = 1$. The solution is converged when:

$$\left\|\boldsymbol{b}^{(n+1)} - \boldsymbol{b}^{(n)}\right\| < \epsilon,$$

where ϵ is some tolerance and $\boldsymbol{x}_{\max} = \boldsymbol{b}^{(n+1)}$ is the eigenvector solution with the largest eigenvalue. The associated largest eigenvalue can then be found from Eq. (A.13):

$$\lambda_{\max} = \frac{\boldsymbol{x}_{\max}^H \boldsymbol{C} \boldsymbol{x}_{\max}}{\boldsymbol{x}_{\max}^H \boldsymbol{x}_{\max}},$$

where superscript H indicates the complex-conjugate transpose.

To demonstrate how the power iteration method works, the initial starting vector can be expanded into a sum of the eigenvectors of $\boldsymbol{C}$:

$$\boldsymbol{b}^{(0)} = \sum_i^N c_i \boldsymbol{x}_i,$$

$$c_i \neq 0,$$

and N is the order of the matrix $\boldsymbol{C}$. Plugging the expression for $\boldsymbol{b}^{(0)}$ into Eq. (A.14) and using Eq. (A.13) shows why the power iteration method works:

$$\boldsymbol{b}^{(1)} = \boldsymbol{C}\boldsymbol{b}^{(0)} = \boldsymbol{C} \sum_i^N c_i \boldsymbol{x}_i = \sum_i^N c_i \lambda_i \boldsymbol{x}_i.$$

Extending the above equation in terms of the number of iterations n yields:

$$\boldsymbol{b}^{(n+1)} = \boldsymbol{C}\boldsymbol{b}^{(n)} = \sum_i^N c_i \lambda_i^{n+1} \boldsymbol{x}_i.$$

For a moderately large number of iterations, say $n = 10$, $\boldsymbol{b}^{(n+1)}$ is dominated by the contributions of the eigenvector with largest λ_i. Practical implementations normalize $\boldsymbol{b}^{(n+1)}$ after each iteration so that $\left\|\boldsymbol{b}^{(n+1)}\right\|_2 = 1$ and start with a randomized vector to ensure $c_i \neq 0$.

The Arnoldi iteration method [65] is very similar to the power iteration method.

Where the power iteration method only finds the eigensolution with largest eigenvalue, the Arnoldi iteration method finds the n largest eigenvalues. This is done by using information from each iteration to form a Krylov subspace [69]:

$$\mathcal{K}_n\left(\boldsymbol{C},\, \boldsymbol{b}_0\right) = \operatorname{span}\left\{\boldsymbol{b}_0,\, \boldsymbol{C}\boldsymbol{b}_0,\, \boldsymbol{C}^2\boldsymbol{b}_0,\, \ldots,\, \boldsymbol{C}^{n-1}\boldsymbol{b}_0\right\} = \operatorname{span}\left\{\boldsymbol{b}_0,\, \boldsymbol{b}_1,\, \boldsymbol{b}_2,\, \ldots,\, \boldsymbol{b}_{n-1}\right\}.$$

From this subspace an orthonormal basis is extracted into the matrix $\boldsymbol{V}_n$ using Gram–Schmidt orthonormalization. The problem is then projected onto the upper Hessenberg matrix $\boldsymbol{H}_n$:

$$\boldsymbol{V}_n^H \boldsymbol{C} \boldsymbol{V}_n = \boldsymbol{H}_n.$$

For sufficiently large n, the eigenvalues of $\boldsymbol{H}_n$ are approximately equal to the largest eigenvalues of $\boldsymbol{C}$. Since $\boldsymbol{H}_n$ is an $n \times n$ matrix, dense eigenvalue methods can be used to quickly obtain these approximate eigenvalues and eigenvectors. If $\boldsymbol{y}^{(j)}$ denotes the j^{th} eigenvector of the matrix $\boldsymbol{H}_n$, the corresponding eigenvector to the original problem is found as:

$$\boldsymbol{x}^{(j)} = \boldsymbol{V}_n \boldsymbol{y}^{(j)}.$$

The Arnoldi iteration method is summarized in Algorithm 1 where EIG is a function that uses QR decomposition to return all eigenvalues and eigenvectors. $\boldsymbol{\Lambda}_n$ is a diagonal matrix containing the n largest eigenvalues and $\boldsymbol{X}_n$ is a matrix whose columns are the corresponding eigenvectors.

Generalized eigenvalue problems can be accommodated by changing the matrix-vector multiplication of $\boldsymbol{C}$ with $\left(\boldsymbol{A} - \sigma\boldsymbol{B}\right)^{-1}\boldsymbol{B}$ where σ is a guess of the eigenvalue and $\boldsymbol{A}$ and $\boldsymbol{B}$ correspond to the generalized eigenvalue problem in Eq. (A.15):

$$\boldsymbol{A}\boldsymbol{x} = \lambda \boldsymbol{B}\boldsymbol{x}. \tag{A.15}$$

Algorithm 1 Arnoldi iteration algorithm.

procedure ARNOLDI($\boldsymbol{C}$)
  for k from 2 to $n-1$ **do**
    $\boldsymbol{q}_k = \boldsymbol{C}\boldsymbol{q}_{k-1}$
    for j from 1 to $k-1$ **do**
      $h_{j,k-1} = \boldsymbol{q}_j^H \boldsymbol{q}_k$
      $\boldsymbol{q}_k = \boldsymbol{q}_k - h_{j,k-1}\boldsymbol{q}_j$
    end for
    $h_{k,k-1} = \|\boldsymbol{q}_k\|_2$
    $\boldsymbol{q}_k = \frac{\boldsymbol{q}_k}{h_{k,k-1}}$
  end for
  $$\boldsymbol{H}_n = \begin{bmatrix} h_{1,1} & h_{1,2} & h_{1,3} & \cdots & h_{1,n} \\ h_{2,1} & h_{2,2} & h_{2,3} & \cdots & h_{2,n} \\ 0 & h_{3,2} & h_{3,3} & \cdots & h_{3,n} \\ \vdots & \ddots & \ddots & \ddots & \vdots \\ 0 & \cdots & 0 & h_{n,n-1} & h_{n,n} \end{bmatrix}$$
  $\boldsymbol{V}_n = \begin{bmatrix} \boldsymbol{q}_1 & \boldsymbol{q}_2 & \cdots & \boldsymbol{q}_n \end{bmatrix}$
  $\begin{bmatrix} \boldsymbol{\Lambda}_n & \boldsymbol{Y}_n \end{bmatrix} = \mathrm{EIG}(\boldsymbol{H}_n)$
  $\boldsymbol{X}_n = \boldsymbol{V}_n \boldsymbol{Y}_n$
  return $\boldsymbol{\Lambda}_n$, $\boldsymbol{X}_n$
end procedure

Eigenvalues of the generalized problem are recovered from the shift-inverted problem by:

$$\lambda^{(i)} = \frac{1}{\gamma^{(i)}} + \sigma,$$

where $\gamma^{(i)}$ is the i^{th} eigenvalue of the shift-inverted problem.

APPENDIX B

NUMERICAL TOOLS

Several numerical tools have been developed in the course of this research. The main functions of these codes are: multimode decomposition, solving the PNS equations, computing BiGlobal secondary instabilities, and adjoint optimization. All of these codes are written in C++ using the KeyCpp and Trilinos software libraries and are incorporated into the single library named the Transient Growth Library. Due to the continual evolution of software, this appendix will not give implementation details of the codes but rather give a high-level overview. Otherwise, this appendix would very quickly become out-dated.

Multimode Decomposition computes the continuous spectrum amplitude curves, $C_k^{A,B}$, for a given velocity profile. The multimode decomposition code is largely based upon Tumin [42], Denissen & White [20], and Denissen [38]. This library consists of 3 main classes. The base class is the BES class. The BES class describes the Biorthogonal Eigenfunction System (BES) for time-invariant, incompressible Blasius flow. The main job of the BES class is to compute direct and adjoint solutions of the BES. These direct and adjoint solutions are then used by the classes CompleteData and PartialData to perform multimode decomposition.

Parabolized Navier–Stokes Solver computes downstream solutions to the PNS equations given an initial state. The PNS code has been developed similarly to the methods of Paredes & Theofilis [84] and uses finite-differences and Newton iterations to solve the nonlinear problem.

BiGlobal Secondary Instability Solver computes the inviscid/viscous, temporal/spatial, and incompressible/compressible stability of basic states that are inhomogeneous in two directions. Finite-differences are used to discretize the LSE resulting in a generalized eigenvalue problem. The eigenvalue problem is solved using a shift-invert transformation, LU decomposition, and Arnoldi iterations.

Optimization Solver uses adjoint optimization to compute the initial disturbances that maximize or minimize objective functions based on BiGlobal secondary instabilities. This solver also accommodates the traditional definition of an optimal disturbance which maximizes the growth of the disturbance kinetic energy.

APPENDIX C

MATRIX OPERATORS

C.1 Linear Stability Equation (LSE) Operators for 1D Boundary Layers

$$\boldsymbol{A} = \begin{pmatrix} 0 & 1 & 0 & 0 & 0 & 0 \\ i\left(\alpha U - \omega\right)\mathrm{Re}_\delta + \alpha^2 + \beta^2 & 0 & \mathrm{Re}_\delta \frac{\partial U}{\partial y} & i\alpha \mathrm{Re}_\delta & 0 & 0 \\ -i\alpha & 0 & 0 & 0 & -i\beta & 0 \\ 0 & -\frac{i\alpha}{\mathrm{Re}_\delta} & -\frac{\alpha^2+\beta^2}{\mathrm{Re}_\delta} - i\left(\alpha U - \omega\right) & 0 & 0 & -\frac{i\beta}{\mathrm{Re}_\delta} \\ 0 & 0 & 0 & 0 & 0 & 1 \\ 0 & 0 & 0 & i\beta \mathrm{Re}_\delta & i\left(\alpha U - \omega\right)\mathrm{Re}_\delta + \alpha^2 + \beta^2 & 0 \end{pmatrix} \tag{C.1}$$

$$\tilde{\boldsymbol{A}}_1 = \begin{pmatrix} 0 & 1 & 0 & 0 & 0 & 0 & 0 & 0 & 0 \\ -i\omega \mathrm{Re}_\delta + \beta^2 & 0 & \mathrm{Re}_\delta \frac{\partial U}{\partial y} & 0 & 0 & 0 & 0 & 0 & 0 \\ 0 & 0 & 0 & 0 & -i\beta & 0 & 0 & 0 & 0 \\ 0 & 0 & -\frac{\beta^2}{\mathrm{Re}_\delta} + i\omega & 0 & 0 & -\frac{i\beta}{\mathrm{Re}_\delta} & 0 & 0 & 0 \\ 0 & 0 & 0 & 0 & 0 & 1 & 0 & 0 & 0 \\ 0 & 0 & 0 & i\beta \mathrm{Re}_\delta & -i\omega \mathrm{Re}_\delta + \beta^2 & 0 & 0 & 0 & 0 \\ 0 & 0 & 0 & 0 & 0 & 0 & 1 & 0 & 0 \\ 0 & 0 & 0 & 0 & 0 & 0 & 0 & 1 & 0 \\ 0 & 0 & 0 & 0 & 0 & 0 & 0 & 0 & 1 \end{pmatrix} \tag{C.2}$$

$$\tilde{\boldsymbol{A}}_2 = \begin{pmatrix} 0 & 0 & 0 & 0 & 0 & 0 & 0 & 0 & 0 \\ U\mathrm{Re}_\delta & 0 & 0 & \mathrm{Re}_\delta & 0 & 0 & -1 & 0 & 0 \\ -1 & 0 & 0 & 0 & 0 & 0 & 0 & 0 & 0 \\ 0 & -\frac{1}{\mathrm{Re}_\delta} & -U & 0 & 0 & 0 & 0 & \frac{1}{\mathrm{Re}_\delta} & 0 \\ 0 & 0 & 0 & 0 & 0 & 0 & 0 & 0 & 0 \\ 0 & 0 & 0 & 0 & U\mathrm{Re}_\delta & 0 & 0 & 0 & -1 \\ -1 & 0 & 0 & 0 & 0 & 0 & 0 & 0 & 0 \\ 0 & 0 & -1 & 0 & 0 & 0 & 0 & 0 & 0 \\ 0 & 0 & 0 & 0 & -1 & 0 & 0 & 0 & 0 \end{pmatrix} \tag{C.3}$$

$$\tilde{\boldsymbol{A}} = \tilde{\boldsymbol{A}}_1 + i\alpha \tilde{\boldsymbol{A}}_2 \tag{C.4}$$